

December 2014

Optical Spring Stabilization

James Lough
Syracuse University

Follow this and additional works at: <https://surface.syr.edu/etd>



Part of the [Physical Sciences and Mathematics Commons](#)

Recommended Citation

Lough, James, "Optical Spring Stabilization" (2014). *Dissertations - ALL*. 172.
<https://surface.syr.edu/etd/172>

This Dissertation is brought to you for free and open access by the SURFACE at SURFACE. It has been accepted for inclusion in Dissertations - ALL by an authorized administrator of SURFACE. For more information, please contact surface@syr.edu.

ABSTRACT

The Advanced LIGO detectors will soon be online with enough sensitivity to begin detecting gravitational waves, based on conservative estimates of the rate of neutron star inspirals. These first detections are sure to be significant, however, we will always strive to do better. More questions will be asked about the nature of neutron star material, rates of black hole inspirals, electromagnetic counterparts, etc. To begin to answer all of the questions aLIGO will bring us we will need even better sensitivity in future gravitational wave detectors.

This thesis addresses one aspect that will limit us in the future: angular stability of the test masses. Angular stability in advanced LIGO uses an active feedback system. We are proposing to replace the active feedback system with a passive one, eliminating sensing noise contributions. This technique uses the radiation pressure of light inside a cavity as a stable optical spring, fundamentally the same as technique developed by Corbitt, et al. [1] with an additional degree of freedom.

I will review the theory of the one dimensional technique and discuss the multidimensional control theory and angular trap setup. I will then present results from the one-dimensional trap which we have built and tested. And propose improvements for the angular trap experiment.

Along the way we have discovered an interesting coupling with thermal expansion due to round trip absorption in the high reflective coatings. The front surface HR coating limits our spring stability in this experiment due to the high circulating power and small beam spot size.

OPTICAL SPRING STABILIZATION

By

James D. Lough

B.S. Virginia Tech, 2001

DISSERTATION

SUBMITTED IN PARTIAL FULFILLMENT OF THE REQUIREMENTS

FOR THE DEGREE OF

DOCTOR OF PHILOSOPHY IN PHYSICS

Syracuse University

December 2014

Copyright © 2014 James D. Lough
All rights reserved.

Preface

The thesis presented here would not have been possible without collaboration with my colleagues. First, and foremost, the main subject of this thesis is the optical trap experiment taking place at Syracuse University. Much of the work in setting up the experiment was done together and will be difficult to differentiate exact contributions from members.

This experiment was very much a combined effort of primarily four people: our PI Stefan Ballmer, David Kelley, Antonio Perreca, and myself. We were fortunate to have some major infrastructure in place when we started: two large vacuum bell jars, two optics benches with floating legs. The rest of the experiment was pretty much built from the ground up.

Another graduate student, Fabian Magana-Sandoval recently joined our team and has contributed to the building of quadrant photodiode (QPD)s and the commissioning of the optical lever.

There has also been contributions from other graduate students as part of requirements for the course Graduate Laboratory:

- Prayush Kumar designed the intensity stabilization servo (ISS).
- Alex Nitz worked on the pre-mode cleaner (PMC).
- Chris Biwer is adding a feedforward modification to the PMC.

Also, my work on building and commissioning the ISS was for fulfillment of the grad lab course.

My major contributions to the experiment have been:

- setting up the vacuum system infrastructure and electrical feedthroughs,

- designing and building the reference cavity and suspension for the frequency stabilization servo (FSS),
- designing the trap output mirror "payload" suspension,
- assembling the digital control system,
- and assembling and commissioning the suspension control loops.

The theory presented in chapter 2 is primarily copied from our group's recent paper, Multidimensional optical trapping of a mirror, Perreca et al. [2]

Acknowledgments

There are so many people I would like to thank. It would not be possible to list every individual that has impacted my life over the past five years.

First, I would like to thank my advisor, Stefan Ballmer. Your breadth of knowledge and your intuition in the lab never ceases to amaze me. You set the standard that I strive to achieve.

I want to thank Duncan for welcoming me into the group 5 years ago and for making me a better scientist.

To Peter, Thank you for all of your insightful wisdom. I am honored to have had the opportunity to learn from you.

I would also like to thank all the members of my defense committee — Duncan Brown, Martin Forstner, Seth Jolly, Matt LaHaye, and Peter Saulson — for taking time out of their busy schedules to read and critique my work.

From my first days here, I want to thank Andy Lundgren for helping me get started on learning all the tools and tricks I've relied on to survive.

To the LIGO PSL team, Jan, Benno, Christina, and Patrick, for helping me understand the PSL and allowing me to invade the PSL code.

Also from my short time at the Livingston site, I must thank Keith Thorne for getting up and running on everything front-end related. Without your help and the help from Rolf and Alex I would not have been able to build the digital system which has been such an integral part of our experiment.

I must also thank Peter Couvares for his help with deep system administration questions I've needed answers on to get the front-end working.

The machine shop personnel have helped immensely through the years. To each of them, Charlie, Lou, Lester, and Phil I owe much gratitude. From helping me route the 300' foot long GPS antenna cable through your shop to providing me with emergency

air pressure to float our tables.

To Sally Prasch and Steve Penn, a huge thanks for sharing with me your expertise in glass work, a little bit of which is embedded in the heart of this experiment.

And of course to my lab-mates, Antonio, David, and Fabian: I have learned so much working with all of you.

I want to especially thank my parents for their careful guidance throughout my life. And to my sister for just being there for me throughout my life.

I want to thank my closest family. Your love and support have been invaluable. To Elizabeth and Henry for all the laughter and joy you have given us. And last, but not least to my wife Amber: you have helped me in so many ways, I really cannot imagine getting through this without you and I look forward to sharing all of the future with you.

Contents

Preface	iv
Acknowledgments	vi
List of Tables	xi
List of Figures	xiii
1 Introduction	1
1.1 Gravitational Waves	2
1.2 Angular Control	3
1.2.1 Limitations	7
2 Angular Optical Trap	9
2.1 Stability principle	9
2.1.1 Damped mechanical oscillator stability	10
2.1.2 Optical spring: a classical model	12
2.1.3 Double Carrier Spring	14
2.2 Control model of longitudinal and angular degrees of freedom	14
2.2.1 An Example	15
2.2.2 Stability range	18
2.3 Angular instability	19
2.4 Radiation Pressure Noise	20
2.5 Technical Noise	24
3 Pre-Stabilized Laser	25
3.1 Laser Head	26

3.2	Intensity Stabilization	27
3.2.1	Sensing	27
3.2.2	Actuation	30
3.3	Frequency Stabilization	30
3.3.1	Sensing	31
3.3.2	Feedback	32
3.3.3	Actuation	32
4	Linear Trap Experiment	34
4.1	Design Considerations	34
4.2	Suspension Systems	36
4.2.1	Payload Suspension	36
4.2.2	Intermediate Suspension	46
4.3	Experimental Layout	46
4.4	Locking Challenges	51
4.4.1	Optical Lever	51
4.4.2	Actuation Range and Bandwidth	52
4.5	Sub-Carrier Servo	52
5	Noise Sources	55
5.1	Seismic	55
5.2	Thermal	57
5.2.1	Derivation of Payload Suspension Thermal Noise	57
5.2.2	Other Thermal Noise Sources	61
5.3	Laser Frequency	63
5.4	Laser Intensity	65
5.5	Total Noise Budget	65
6	Results	69
6.1	Stability	69
6.1.1	Stability Range	73
6.2	Linear Trap Experiment, 1st Edition	79
6.3	Experimental Layout Revision	81
6.3.1	Faraday Isolator	86

6.4	Linear Trap Experiment, 2nd Edition	88
6.4.1	Optical Spring Cavity Residual Motion	90
6.4.2	Optic Thermal Expansion Contribution	92
7	Conclusions	98
7.1	Implications for Angular Trap Experiment	98
A	Optical Spring Derivation	102
A.1	Optical spring constant derivation	102
A.2	Torsion pendulum mechanical plant	109
A.3	Stability in two dimensions	110
B	More Derivations	112
B.1	Mode Matching	112
C	Digital System	115
C.1	System Overview	115
C.1.1	LIGO Real-Time System Theory of Operation	117
C.1.2	ADC/DAC Hardware Description	118
C.1.3	Timing	118
C.2	Front-End Code Installation	122
C.2.1	Using LLO Cloned Disk	122
C.2.2	Minimal tar deploy	123
C.2.3	From Gentoo Source	126
C.3	Front-End Operation	129
C.3.1	Using a Model	129
C.3.2	Running a Model	130
C.3.3	Changing a Filter	131
C.3.4	Changing a Model	131
C.3.5	Data Storage	131
C.3.6	Analysis Tools	132
	Bibliography	134

List of Tables

1	Trap Cavity Parameters	36
2	Epoxy Parameters	62
3	Parameters for Linear Trap Experiment, 1st Edition	79
4	Experiment 1 Spring Measurements	80
5	Optical Trap, 2nd Edition Spring Measurements	89
6	Optical Trap, 2nd Edition Optical Spring Fit Parameters	93
7	Angular Trap Parameters	101
8	Digital System Hardware Interface Matrix	117
9	Front-End Tools	130

List of Figures

1	LIGO Schematic	4
2	Hermite-Gaussian Modes	5
3	Wavefront sensing beam in reflection	5
4	Mechanical Oscillator and Feedback	13
5	Angular Trap Sketch	16
6	Multi-Dimensional Mechanical Transfer Function	17
7	Cavity Open Loop Gains	17
8	Stability Range	18
9	Radiation Pressure Noise	23
10	Intensity Stabilization Servo	28
11	ISS Closed Loop Noise	29
12	PDH Error Signal	31
13	Reference Cavity Suspension Design	33
14	Small Optic Suspension	37
15	Blade Spring Modification for Vertical Isolation	38
16	Trapping Loops	39
17	Subcarrier Servo	40
18	Background Seismic Noise	41
19	Q Measurement of Glass Suspension	45
20	Double Pendulum	47
21	Double Pendulum Feedback Representation	48
22	Small Mirror Suspension	49
23	Linear Trap Control	50
24	Subcarrier Servo Electronics	53
25	Room Layout	54

26	Seismic Noise Spectrum	56
27	Sketch of Thermal Noise Calculation	59
28	Epoxy Thermal Noise Contribution to Trap Length	62
29	Thermal Noise Sources	64
30	Frequency Noise	64
31	Intensity Noise	66
32	Noise Budget	68
33	Open Loop Gain Measurement	70
34	RMS Optical Spring Residual Motion	76
35	Parameter Space for 2nd Edition	77
36	Damped Spring Closed Loop Gain	78
37	Parameters from the 1st Edition	82
38	Data Fitting of Open Loop Gain for 1st Results	83
39	Subcarrier Detuning Gain Factor	84
40	35MHz RF Photodiode Response	85
41	New Table 1 Input Optics	86
42	New Experimental Control Scheme	87
43	Active Feedback Control for 2nd Edition	88
44	Trap Loop With Optic Thermal Expansion	94
45	Data Fitting of Open Loop Gain for 2nd Results	95
46	Data Fitting Without Absorption Coefficient	96
47	Estimate of Passively Attenuated Noise	97
48	Derivation of Optomechanical Cavity Dynamics	102
49	Front End System Overview	116
50	GPS Antenna Location	119
51	555 Timer Diagram	120
52	GPS Pulse Extender	121

to
my little scientists,
Elizabeth and Henry

Chapter 1

Introduction

The physics community has been building gravitational wave detectors for decades. The resonant bar detectors of the past have given way to the new interferometric detectors which have achieved impressive sensitivities. These detectors are soon to be dramatically surpassed by detectors with a more sophisticated optical layout, adding signal recycling to the configuration.

This new generation of gravitational wave detectors are rapidly coming online. Advanced LIGO will be at design sensitivity within a year. These new detectors will see further, by an order of magnitude over initial LIGO, this corresponds to a 1000 times greater surveilled volume. At this sensitivity, one day of Advanced LIGO observations will survey a larger space-time volume than the 2 years of observations with initial LIGO. aLIGO isn't a simple upgrade, it's literally a new detector. Every component has been ripped out and replaced. The laser source is new, pumping out a massive 180 Watts of power. The radiation pressure noise associated with this power will start to dominate the displacement noise of the new 40kg test masses. From the state of the art coatings technology to the silicate bonded monolithic fused silica fiber assemblies we have left virtually nothing untouched.

As I am writing this, the detector in Livingston is already beginning to surpass the best sensitivity we ever had in initial LIGO. The detector at Hanford will soon be sealed in it's capsule to embark on a journey into the farthest reaches of the universe¹.

Reflecting over my time at Syracuse, we have seen the Large Hadron Collider turn

¹Manufacturing errors in the test mass coatings required a new set to be installed, delaying the closure of the vacuum system.

on and confirm the existence of those things we were looking for². Of course I can't just leave the Higgs Boson as a footnote. This is what gives matter its mass and as far as we know we can't have gravitational waves without mass. Well, we wouldn't exist without mass either, but that's beside the point...

From this we begin,

$$F = ma. \tag{1.1}$$

1.1 Gravitational Waves

The foundation of Einstein's theory of general relativity is that the motion of a freely falling body is governed by the local space-time curvature. This curvature is in turn influenced by the presence of matter. This matter not only curves the space it occupies, but also curves the space around it.

As matter moves through space, the curvature of space changes. Special relativity tells us that information cannot travel faster than the speed of light. The information about how the curvature of space is changing must propagate at finite speed. From the multipole expansion of the mass distribution, the monopole (which is the first term) is a scalar quantity that is simply the total mass of the object. The second term is, called the 'dipole' is a vector which is the sum of all the bits of mass multiplied by their position vector from a fixed reference point. The dipole term is identically the center of mass location times the total mass. This term can change with time, however the first derivative mv (momentum) is conserved. The third term is known as the quadrupole term. It is this term which has a non zero second derivative that gives rise to a wave equation. And the amplitude of this gravitational wave is,

$$h = \frac{2G}{c^4 r} \ddot{I}, \tag{1.2}$$

where the unitless term h is the gravitational wave strain. This strain is the $\frac{\Delta L}{L}$ perturbation on the background space-time metric that we are looking for. Gravitational waves stretch space-time in one direction while squeezing it in the orthogonal direction.

We look for the strain perturbations by measuring the distance between two freely falling objects we call test masses. In the simple case of a two test mass detector

²the Higgs Boson

(one arm of LIGO) we are only sensitive to half of the signal (assuming optimal orientation). Since the orthogonal direction is moving in the opposite way, it would be natural to choose an instrument which measures the difference in length between two orthogonal directions. And with two orthogonal arms we are sensitive to the full amplitude of the wave. It is important to note that this factor of 2 increase in the signal, though helpful, is not the primary motivation for two arms. The big benefit comes from common noise cancellation. We can cancel out common length noise, typically dominated by frequency noise in the two arms because the gravitational wave will couple directly into the differential degree of freedom in the detector. See figure 1.

1.2 Angular Control

In order for our instrument to be sensitive to gravitational waves we want the test masses to swing freely. Also, since the gravitational wave amplitude is a strain and we are measuring changes in length, we get better sensitivity with longer arms. Longer arms, however, also make it more difficult to keep the mirrors pointed at each other. An angular control system is necessary for the sensitive alignment of the instrument.

In Advanced LIGO we use an active feedback control for angular alignment of the main mirrors[3]. Sensing for this feedback is done with a technique known as wavefront sensing (WFS). The beam entering a cavity is phase modulated to produce sidebands. The phase modulation is done at a high enough frequency so that almost all of the sideband beams are reflected.

Wavefront sensing works by beating the carrier beam reflected from the cavity against the reflected sidebands. Any misalignment results in a 1st order mode component of the reflected carrier beam relative to the reflected sidebands. This effect is shown in figure 3. If we were to then integrate over the transverse dimensions using a photodiode, the beat signal would produce no amplitude since we are beating together orthogonal transverse modes. We can defeat this by splitting the photodiode in two and measuring the difference between the two sides.

I will illustrate this effect using bra-ket notation. Keeping things to first order, the reflected carrier beam is composed of the TEM_{00} mode with a small amount of

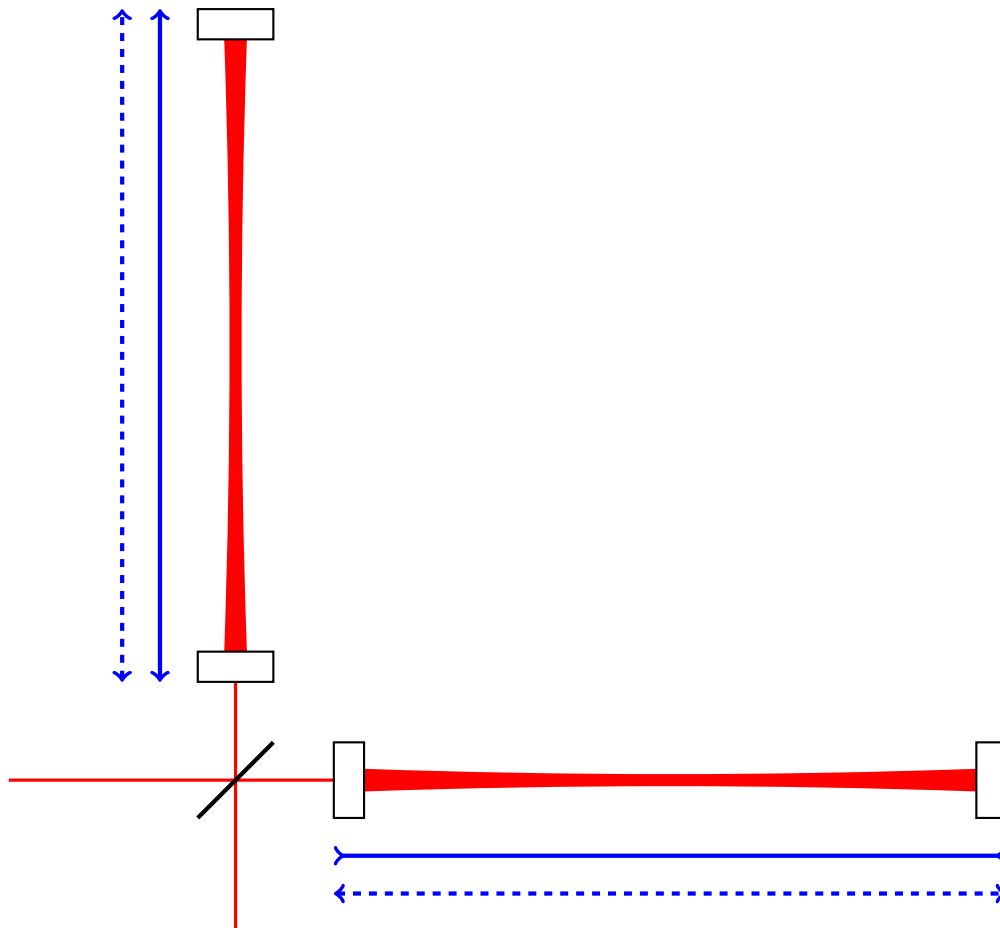


Figure 1: This schematic shows the layout of a basic interferometric gravitational wave detector. Each arm of the interferometer is a Fabry-Perot cavity which circulates the light in the arms, increasing the response of the detector. The blue lines indicate the common (dashed) and differential (solid) degrees of freedom. The Michelson naturally reads out the differential degree of freedom which is free of common noise such as the intensity and frequency noise of the laser.

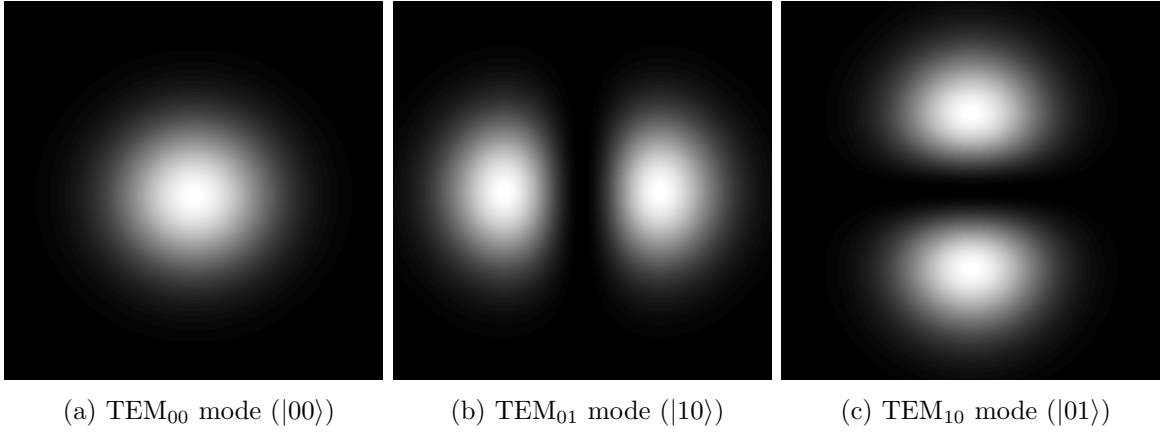


Figure 2: Hermite-Gauss modes. The first three transverse electro magnetic modes from Hermite-Gauss decomposition are depicted here. These images indicate the power density across the transverse dimensions. There is one first order mode for each transverse dimension. The first order modes are odd functions in field amplitude along the respective dimension.

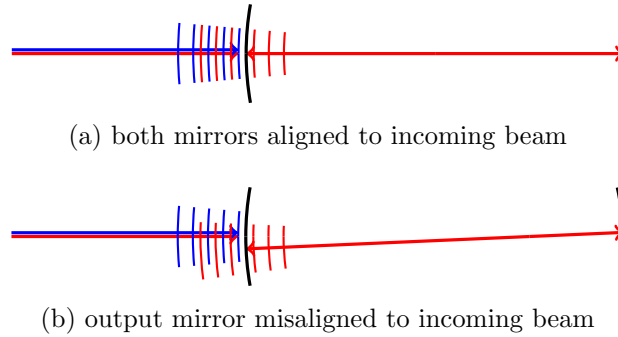


Figure 3: beam reflected from cavity for wavefront sensing. The input beam to the cavity is from the left. Blue represents the sideband beams which are promptly reflected from the input mirror. Red represents the carrier beam which resonates in the cavity. The curves represent the wavefronts of each as they are added together in reflection. Misalignment of a mirror causes a transverse offset between the reflected carrier beam and the reflected subcarrier beam. So, in the transverse mode basis of the reflected sidebands, the reflected carrier gains higher order mode content. This higher order mode content contains the alignment information which is detected with the wavefront sensor.

the TEM₁₀ mode,

$$|CC\rangle \approx |00\rangle + \eta |10\rangle \quad (1.3)$$

$$= |00\rangle + \eta |00\rangle \frac{2x}{w(z)} e^{i\Psi(z)} . \quad (1.4)$$

The TEM₀₀ mode from the sidebands looks like,

$$|SB\rangle = |00\rangle \cos \Omega t . \quad (1.5)$$

The combined beam in reflection looks like,

$$|\text{REFL}\rangle = |CC\rangle + |SB\rangle . \quad (1.6)$$

Now, we apply our sensing operator, PD. If PD is simply a single photodiode, we get,

$$\langle \text{REFL} | \text{PD} | \text{REFL} \rangle = \langle 00|00\rangle (1 + \cos \Omega t)^2 + 2\eta \langle 00|10\rangle (1 + \cos \Omega t) + \eta^2 \langle 10|10\rangle \quad (1.7)$$

The term which is first order in Ω will vanish due to orthonormality. We can defeat this by splitting our photodiode in two and subtracting one side from the other. Now, the integral $\langle 00 | \text{PD} | 10 \rangle$ is no longer zero. If the photodiode is perfectly aligned with the transverse mode basis, the integrals $\langle 00 | \text{PD} | 00 \rangle$ and $\langle 10 | \text{PD} | 10 \rangle$ become zero.

The non-zero beat signal is then demodulated to give us the error signal.

From the longitudinal dimension of the wave, we get an additional phase degree of freedom. There is a Gouy phase term which depends on the distance from the waist of the beam. The Gouy phase, $\Psi(z)$, is defined by

$$\tan \Psi(z) = z/z_R ,$$

where z_R is the Rayleigh range which is defined as the distance from the beam waist to the point where the beam radius increases by $\sqrt{2}$.

Since the input test mass and end test mass are at different Gouy phases their misalignment affects a different linear combination of quadratures of the beam.

Splitting the photodiode into four quadrants gives us sensitivity to two alignment degrees of freedom.

We use two quadrant photodiodes for sensing the four angular degrees of freedom of the two cavity mirrors. The two quadrant photodiode (QPD)s are placed in reflection at different distances from the input mirror for sensing the different Gouy phases. Then we can transform the four degrees of freedom of the sensor output to the four degrees of freedom of the mirror alignments.

1.2.1 Limitations

There are limitations to this approach which will ultimately add noise into the sensitive band of the detector. This noise comes from the alignment sensing which gets fed back to the alignment actuators and couples into the gravitational wave strain signal.

The coupling of angular motion to gravitational wave strain occurs due to misalignment of the beam on the test masses as well as unbalanced actuation on the test masses.

The ability to attenuate the sensing signal is limited by the fact that we need to control above the hard mode frequency of the Sidles-Sigg instability [4] which, for Advanced LIGO at high power, is at about 6 Hz. We need a sharp cutoff in the feedback below 10Hz in order to not introduce sensing noise in the sensitive band of LIGO. There is very little room to attenuate the sensing noise sufficiently above 10 Hz while keeping a stable feedback loop with a unity gain frequency above 6 Hz.

As power is increased, the sensing noise from WFS will contribute more to the interferometer noise budget due to the necessary feedback control requirements.

The WFS noise contribution will actually increase at a higher rate than the contribution from radiation pressure noise, assuming the control loop has a steep cutoff above the unity gain frequency. If we take the sensing noise from WFS as constant, the frequency of the hard mode of the angular instability will increase with \sqrt{P} . The control bandwidth must then also increase at the same rate. If we also increase the cutoff frequency by \sqrt{P} , the noise contribution from frequencies above the cutoff will then increase by $\sqrt{P^n}$, where n is the cutoff rate (feedback open loop goes as f^{-n}).

Without changing power ratios for the WFS, the situation is improved a little. If we allow the power incident on the WFS sensors to increase with the circulating power in the interferometer, the WFS sensing noise will decrease by \sqrt{P} . The noise contribution from WFS will then increase by $\sqrt{P^{n-1}}$ instead of $\sqrt{P^n}$.

At some point, as we push for better sensitivity in the low frequency regime, there will be a tradeoff between going to higher power in the interferometer and reducing WFS sensing noise coupling to the gravitational wave strain measurement at low frequencies. In the region where the noise contribution from WFS increases by $\sqrt{P^{n-1}}$, the radiation pressure noise increases by \sqrt{P} . If the cutoff falls steeper than f^{-2} the WFS noise will eventually overtake the radiation pressure noise as the laser power increases.

Chapter 2

Angular Optical Trap

We can eliminate the sensing noise from the angular control by replacing the active feedback with a passive stabilization technique. For stabilizing the length degree of freedom of an optical cavity, the active feedback can be reduced or even removed using a passive optical trapping technique.[1] This technique can be applied to additional degrees of freedom by coupling multiple length traps through the same mass. This chapter describes the proposal for optically trapping one angular degree of freedom using two stable optical springs.

2.1 Stability principle

An optically detuned Fabry-Perot cavity naturally leads to a linear coupling between intra-cavity power and mirror position. Depending on the sign of the detuning, this coupling creates an optical spring which is either statically stable or unstable. Due to the time delay in the optical field build-up, the optical spring restoration force is slightly delayed. This leads to a dynamically unstable spring for the statically stable case and a dynamically stable spring for the statically unstable case. Corbitt et. al. [1] demonstrated that by adding a second, frequency-shifted optical field (sub-carrier) with a different detuning and power, a statically and dynamically stable optical spring can be achieved. The dual-carrier scheme has been used to optically trap a gram-scale mirror, controlling its longitudinal degree of freedom. Moreover, the damping of the optical spring can be controlled by adjusting the detuning of both carrier and sub-carrier and their relative amplitudes. This naturally allows for efficient cooling of

the degree of freedom seen by the optical spring. In contrast to a mechanical spring, this damping does not introduce intrinsic losses, and thus does not contribute to the thermal noise.

This technique can be extended to alignment degrees of freedom. By duplicating the Corbitt et al. approach for trapping with a second, different, optical axis and a different beam spot on the controlled mirror, it is possible to control the angular degree of freedom with radiation pressure alone.

To be able to understand the stability of multi-dimensional opto-mechanical systems, we first recall the simple driven damped mechanical oscillator. From there we will stepwise increase the complexity by adding optical springs and additional degrees of freedom.

2.1.1 Damped mechanical oscillator stability

Although the damped mechanical oscillator is a well known system, we will take it as a starting point to make the reading clearer. Our goal is to describe the mechanical oscillator in the language of control theory, which allows us to understand the stability of the system from a different point of view. This approach can then be naturally extended to include the effect of additional optical springs.

The motion of a harmonic oscillator of mass m , spring constant k_m and velocity damping b , driven by the external force F_{ext} , can be expressed as [5]:

$$m\ddot{x} = -k_mx - b\dot{x} + F_{ext} \quad (2.1)$$

b is also called the viscosity coefficient. Often the damping rate $\Gamma = b/(2m)$ is used instead. Traditionally the equation of motion 2.1 is directly used to get the system's position response x when applying the external force F_{ext} . The resulting transfer function is

$$G = \frac{x}{F_{ext}} = \frac{1}{-m\Omega^2 + k_m + ib\Omega} \quad (2.2)$$

with Ω being the angular frequency of the motion.

Alternatively we can describe a damped mechanical oscillator as a feedback system, with the plant being just a free-test mass described by the transfer function

$M = x/F_{ext} = -1/m\Omega^2$, obtained directly from the equation of motion of a free test-mass. The control filter of the feedback loop is the mechanical spring, which takes the mass displacement x as input and acts on the plant with the control signal, or force, F_K , which is subtracted from the external force F_{ext} . The transfer function of the control filter is $K_M = F_K/x = k_m + ib\Omega$. In this picture we can now calculate the closed loop transfer function and obtain the same expression as in equation 2.2:

$$G = \frac{M}{1 + K_M M} = \frac{1}{-m\Omega^2 + k_m + ib\Omega} \quad (2.3)$$

where $OL_M = -K_M M = (k_m + ib\Omega)/m\Omega^2$ describes the open loop transfer function of the system.

Stability

We can now check for the stability of the system in both pictures. We recall from literature that the stability of a system described by its transfer function G can be evaluated looking at the poles of its transfer function in the s-plane ($s = i\Omega$) [6]. In particular a system is stable only if its transfer function's poles have a negative real part, and the multiplicity of poles on imaginary axis is at most 1. The transfer function in equation 2.2 has the following poles:

$$i\Omega = -\frac{b}{2m} \pm \sqrt{\frac{b^2}{4m^2} - \omega_0^2}, \quad (2.4)$$

where $\omega_0^2 = k_m/m$ is the resonant frequency of the pendulum. The value of the damping rate $\Gamma = b/2m$ compared to ω_0 determines whether the system is over-damped, under-damped or critically-damped. But since Γ (or b) is always positive, the real part of the poles is always negative. The system is thus always stable.

From the control theory point of view, the stability can also be evaluated with no loss of generality by considering the open loop transfer function $OL_M = (k_m + ib\Omega)/m\Omega^2$ and applying, for example, the Bode stability criterion [7]. The positivity of b guarantees an always positive phase margin and therefore stability. In the remainder of this work, for simplicity, we will test the stability of the control scheme using the Bode graphical method.

2.1.2 Optical spring: a classical model

Next, we look at an optical spring. We start with a Fabry-Perot cavity of length L_0 , frequency detuning δ , amplitude transmittance coefficients t_1, t_2 and amplitude reflectance coefficients r_1, r_2 of the input and output cavity mirror respectively. The light field inside the cavity builds up and exerts a radiation pressure force on both mirrors.

We define the propagator $X = r_1 r_2 e^{-2i\delta\tau}$ and phase factor $Y = e^{-i\Omega\tau}$, with $\tau = L_0/c$ the one-way travel time of the photon inside the cavity, k is the wave vector of the light field and Ω is the mechanical frequency of the pendulum. From this we can obtain an elastic force-law for small displacement values x , but potentially large detuning from resonance:

$$F_{rad} = F_0 - K_{OS} \cdot x + O(x^2), \quad (2.5)$$

where

$$K_{OS} = K_0 \left[\frac{Y^2}{(1 - Y^2 X)(1 - Y^2 \bar{X})} \right] \quad (2.6)$$

is the optical spring constant and \bar{X} is the complex conjugate of X . Here K_0 is the (mechanical) frequency-independent part of the spring constant:

$$\begin{aligned} K_0 &= F_0 \cdot 2ik \cdot (X - \bar{X}), \quad \text{with} \\ F_0 &= P_0 \cdot \frac{2r_2^2}{c} \cdot \frac{t_1^2}{(1 - X)(1 - \bar{X})} \end{aligned} \quad (2.7)$$

The expression in equations 2.6 and 2.7 is the general expression for K_{OS} up to linear order in x . While approximations for this formula have been published before [8], we are not aware of a previous publication providing the full expression. We address the complete derivation of the optical spring constant K_{OS} in the Appendix A.1. There we also show that with the approximations $2\Omega\tau \ll 1$ and $2\delta\tau \ll 1$ equation 2.6 is equivalent to the expressions already existing in literature [8, 1].

We note that K_0 is a real number. Its sign is determined by the imaginary part of X . A positive sign is associated with positive detuning ($\delta > 0$) and a restoring force (statically stable), while a negative sign is due to negative detuning ($\delta < 0$) and leads to a anti-restoring force (statically unstable). Also, for small (positive) frequencies $\Omega\tau \ll 1$, the sign of the imaginary part of equation 2.6 is opposite to

its real part, leading to positive dynamic feedback for the statically stable case and negative dynamic feedback for the statically unstable case.

Our next step is to couple the optical spring to a mechanical pendulum. We can treat this as either a damped mechanical oscillator with transfer function G , controlled by an optical spring K_{OS} , or as a free mass with transfer function M , controlled by the total feedback filter $H = K_M + K_{OS}$, see Fig.4. In both cases we obtain the

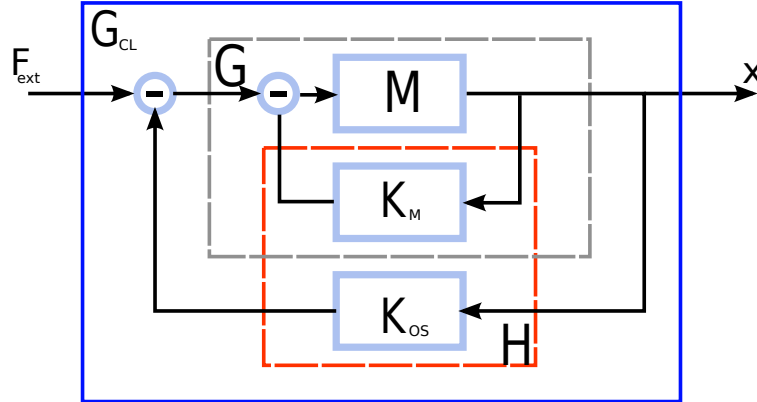


Figure 4: Mechanical oscillator and feedback systems. The mechanical oscillator can be seen as plant (G) and the optical spring K_{OS} as feedback or alternatively as free test mass (plant M) and $H = K_{OS} + K_M$ as feedback. Both the cases lead to the same closed loop transfer function G_{CL} which describes the system as a damped mechanical oscillator in presence of the optical spring, subjected to the external force F_{ext} and corresponding displacement x as output.

same closed-loop transfer function, equivalent to the one we would have obtained by rewriting the equation of motion of a damped mechanical oscillator with an optical spring:

$$\begin{aligned}
 G_{CL} &= \frac{x}{F_{ext}} = \frac{G}{1 + K_{OS}G} = \frac{M}{1 + HM} \\
 &= \frac{1}{-m\Omega^2 + K_M + K_{OS}}
 \end{aligned} \tag{2.8}$$

The stability of the total system can again be evaluated by either looking at the poles of the closed-loop transfer function G_{CL} , or looking at the gain and phase margin of the open loop transfer function $OL_{MH} = -H/m\Omega^2$. The latter is generally more convenient. Unless compensated by large mechanical dissipation in K_M , the positive

dynamic feedback for the statically stable case ($\delta > 0$) leads to a dynamically unstable system. Intuitively this can be understood as a phase delay in the radiation pressure build-up which is caused by the cavity storage time. For $\delta < 0$ the system is statically unstable.

2.1.3 Double Carrier Spring

The seemingly intrinsic instability of optical springs can be overcome by a scheme proposed by Corbitt et al. [1]. The carrier is set at a large positive detuning ($\delta > 0$, large δ/γ). This provides a static restoring force, together with a relatively small dynamic instability (anti-damping). Then a sub-carrier is added at lower power and with a small negative detuning ($\delta < 0$, small $|\delta|/\gamma$). The sub-carrier adds sufficient dissipation to stabilize the total optical spring, while leaving the sign of the static restoring force unchanged. For appropriately chosen parameters of carrier (c) and sub-carrier (sc) (power P_0^c and P_0^{sc} , detuning δ_c and δ_{sc}) the resulting total system thus becomes stable.

The spring constant of the total optical spring is simply the sum of the individual spring constants of the carrier and sub-carrier

$$K_{OS} = K_{OS}^c + K_{OS}^{sc} \quad (2.9)$$

where the individual springs K_{OS}^c and K_{OS}^{sc} are given by equation 2.8.

Conceptually we can think of the dual-carrier optical spring as a physical implementation of a feedback control filter for the mechanical system. With this tool at hand, we can start to analyze the behavior and stability of higher dimensional mechanical systems in the next section.

2.2 Control model of longitudinal and angular degrees of freedom

We will now extend our analysis to additional degrees of freedom. Experimentally, a torsion pendulum suspension is easy to build. Therefore we will focus our attention to controlling the yaw motion of a test mirror, keeping in mind that the method can be applied to any additional degree of freedom. For actively controlling two degrees of freedom (length and yaw), we need a two-dimensional control system. In other

words, we will need a second dual-carrier optical spring in a setup that for example looks like Fig.5. We will label the two dual-carrier optical fields as beams A and B . Each beam includes a carrier and a sub-carrier field, i.e.

$$\text{Beam A} = \text{carrier A} + \text{sub-carrier A} \quad (2.10)$$

$$\text{Beam B} = \text{carrier B} + \text{sub-carrier B}$$

The two beams have a different optical axis, and each has its own optical spring constant, K_{OS}^A and K_{OS}^B , given by equation 2.9.

If we define x_A and x_B as the longitudinal displacement of the mirror at the contact points of beam A and beam B on the test mirror, and F_A and F_B as the corresponding exerted forces, we can describe the mechanical system with a plant matrix M :

$$\begin{pmatrix} x_A \\ x_B \end{pmatrix} = M \begin{pmatrix} F_A \\ F_B \end{pmatrix} \quad (2.11)$$

The explicit expression for M for a torsion pendulum is given in appendix A.2.

The control is provided by the optical springs. In the x_A - x_B basis the control matrix H is diagonal and given by (also see Fig.6)

$$\begin{pmatrix} F_A \\ F_B \end{pmatrix} = H \begin{pmatrix} x_A \\ x_B \end{pmatrix} = \begin{pmatrix} K_{OS}^A & 0 \\ 0 & K_{OS}^B \end{pmatrix} \begin{pmatrix} x_A \\ x_B \end{pmatrix} \quad (2.12)$$

For a multi-dimensional feedback system to be stable, it is sufficient that each individual (one-dimensional) feedback loop is stable, assuming all remaining control loops are closed. In other words, in our two-dimensional opto-mechanical system, we close the beam B control filter for evaluating the open loop transfer functions OL_A , and vice versa. For the open loop transfer functions OL_A and OL_B we then find:

$$\begin{aligned} OL_A &= e_A^T (\mathbb{1} - HM(\mathbb{1} - e_A e_A^T))^{-1} H M e_A \\ OL_B &= e_B^T (\mathbb{1} - HM(\mathbb{1} - e_B e_B^T))^{-1} H M e_B \end{aligned} \quad (2.13)$$

with $e_A^T = (1, 0)$ and $e_B^T = (0, 1)$. The derivation of this expression is given in appendix A.3.

2.2.1 An Example

It is worth considering a specific set of possible values for our model and evaluate the control of angular and longitudinal degrees of freedom of a gram-scale test mirror

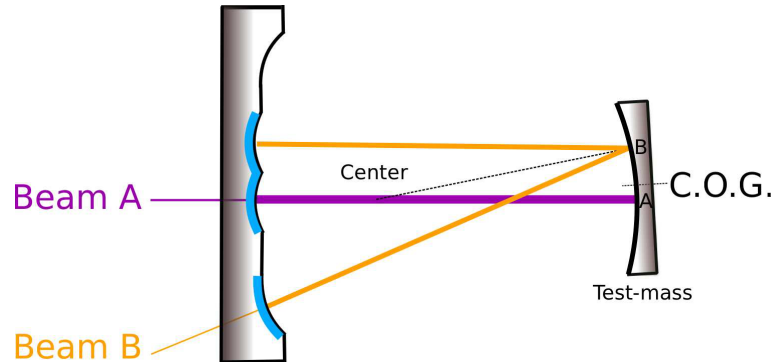


Figure 5: In this sketch the main purple (Beam A) optical axis hits the test mirror at point A, slightly displaced from the center of gravity (C.O.G.), such that it still corresponds mainly to the length degree of freedom. Thus the second orange (Beam B) optical axis, which hits the test mirror closer to the edge at point B, needs much less power to balance the total DC torque. In our test setup the large input coupler is a composite mirror. It is 600 times more massive than the small mirror. The choice of a V-shaped beam B results in a more practical spot separation on the input coupler.

using the radiation pressure of the light. All the optical fields involved in our analysis are derived from the same wavelength light source through frequency shifting. The model includes two optical cavities (Fig.5), referred to as beam A and B, both with an optical finesse of about 8000 and linewidth $\gamma/(2\pi) = 110$ kHz. The main cavity (beam A) is pumped with 1 W of carrier light, detuned by $\delta/(2\pi) = 250$ kHz (blue detuning, $\delta/\gamma = 2$), and 0.2 W of sub-carrier light, detuned by $\delta/(2\pi) = 60$ kHz (red detuning, $\delta/\gamma = -0.5$). This produces a statically and dynamically stable optical spring with a lever arm of 0.8 mm, measured from the payload center of gravity (C.O.G.). A second optical spring (beam B) is pumped with 6 times less power of carrier light, detuned by $\delta/(2\pi) = 186$ kHz (blue detuning, $\delta/\gamma = 1.5$), and 40 mW of sub-carrier light, detuned by 60 kHz (red detuning, $\delta/\gamma = -0.5$). This side cavity has a lever arm of 3.3 mm on the payload, such that the DC radiation pressure torques of beam A and B cancel. The DC radiation pressure force can be canceled by displacing the position pendulum.

The stability of the combined two-dimensional system is addressed in Fig.7. Plotted are the open loop gain functions of the two degrees of freedom (the two optical traps) under the assumption that the other loop is closed. The presence of the second loop introduces a resonance feature in each loop at the unity gain frequency of the

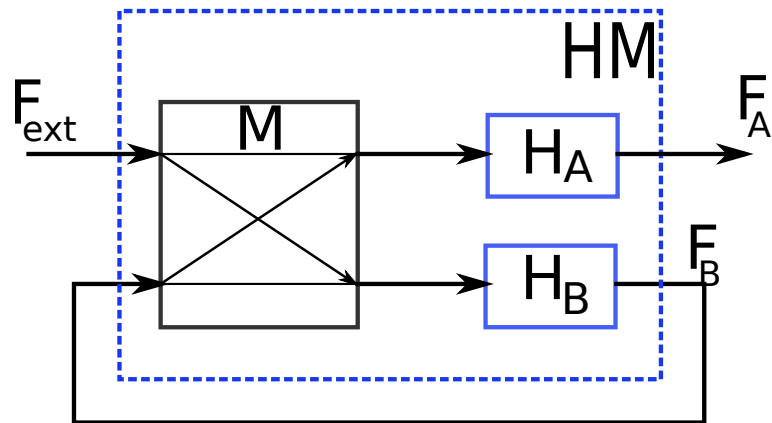


Figure 6: Block diagram of beam A and beam B. The transfer function F_A/F_{ext} is equal to OL_A from equation 2.13. Each loop affects the other resulting in cross terms present in the matrix HM . M and $H_{A,B}$ are the transfer functions of the mechanical system and the optical springs of beam A and B, respectively.

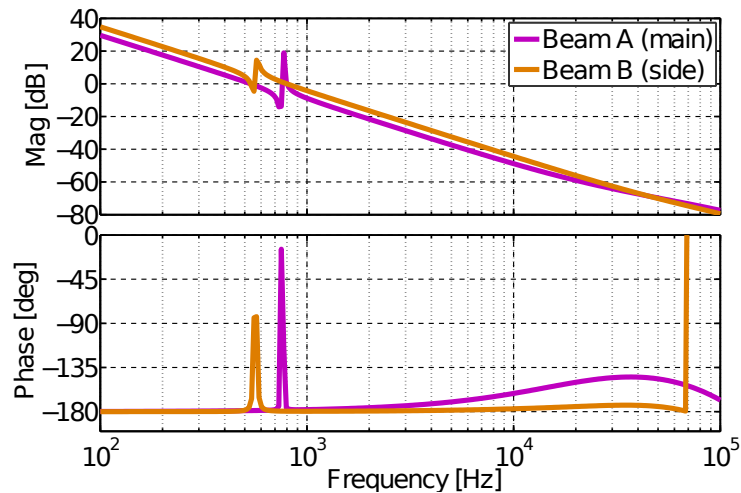


Figure 7: Open loop gain (OLG) for the main and side cavity. The respective other loop is closed, and shows up as a resonance in the OLG. Note that, despite multiple unity gain crossings, both loops are stable because the resonances effectively implement a lead filter and the OLG avoids the critical point -1. Thus the dynamic interplay between multiple trapping beams on one payload does not introduce an instability.

other loop. However the open loop gain avoids the critical point -1 (phase at zero), leading to a stable system. The model parameters were intentionally tuned for low damping / high quality factor in order to demonstrate that the system remains stable. Lower quality factors, and therefore stronger cooling is easily achievable.

2.2.2 Stability range

We can now estimate the robustness of our feedback control system by changing the microscopic length δx_A and δx_B of the two cavities. This changes the detuning of the optical springs for both beams. Therefore the propagators X_A and X_B for both beams change according to $X_{A,B} = r_1 r_2 e^{-i\delta_{A,B} \tau_{A,B}} \cdot e^{ik\delta x_{A,B}}$. For each position both the static and dynamical stability of the total optical spring system given by equation 2.13 is reevaluated.

In Fig. 8 the radiation pressure force due to the intra-cavity power of both beams versus the cavity offset is shown. The green shaded area represents the position range in which the two loops remain stable. The range is ~ 20 pm. The DC force fluctuations that the system can tolerate are given by the y-axis interval that the blue curve spends in the green shaded area.

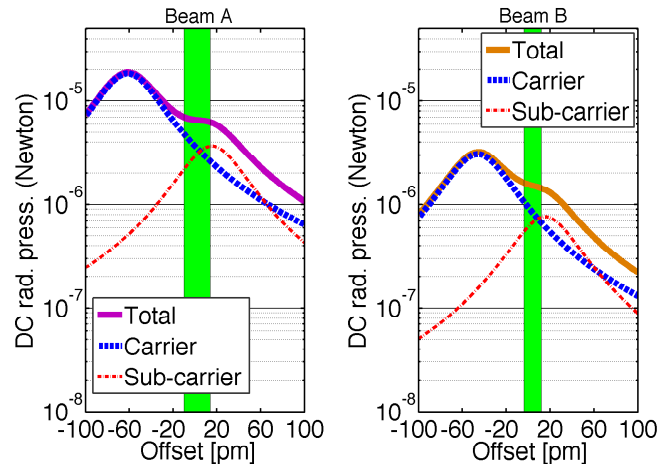


Figure 8: Static carrier and sub-carrier build-up (calibrated in radiation pressure force) as a function of the respective cavity position. Also shown in blue is the total radiation pressure force. Using the stability testing method from section 2.2.2 we find that the trap is both statically and dynamically stable in the green shaded area. With the chosen model parameters those regions are about 20 picometers wide.

2.3 Angular instability

When operated with high intracavity laser power, suspended Fabry-Perot cavities like the arm cavities of LIGO have a well known angular instability. It arises from coupling the misalignment of the two cavity mirrors to radiation pressure torques. This is known as the Sidles-Sigg instability [4]. In this section we show that the intrinsic strength of an optical trap for alignment degrees of freedom is generally bigger, i.e. has a bigger spring constant than any associated Sidles-Sigg instability.

We start with a cavity of length L , with x_1, x_2 being the position of the beam spots on mirrors 1 and 2. θ_1, θ_2 are the yaw angles of the two mirrors, and R_1, R_2 are their radii of curvature. The corresponding g-factors are $g_{1,2} = 1 - L/R_{1,2}$. If one or both of the mirrors are slightly misaligned ($\theta_{1,2} \neq 0$), then the radiation pressure force exerts torques T_1 and T_2 on the two mirrors, given by the following relation (see for instance [4] or [9]):

$$\begin{pmatrix} T_1 \\ T_2 \end{pmatrix} = \frac{F_0 L}{1 - g_1 g_2} \begin{pmatrix} g_2 & -1 \\ -1 & g_1 \end{pmatrix} \begin{pmatrix} \theta_1 \\ \theta_2 \end{pmatrix} \quad (2.14)$$

with $F_0 = P_0 \frac{t_1^2}{(1-X)(1-\bar{X})} \frac{2r_2^2}{c}$ being the intra-cavity radiation pressure force. Sidles and Sigg first pointed out that, since the determinant of the matrix in this equation is negative, the two eigenvalues have opposite sign. This always leads to one stable and one unstable coupled alignment degree of freedom.

First we note that for a situation in which one mass is sufficiently heavy that we can neglect any radiation pressure effects on it (i.e. $\theta_1 = 0$), it is sufficient to choose a negative branch cavity (i.e. $g_1 < 0$ and $g_2 < 0$) to stabilize the setup. This is for instance the case for the example setup described in Fig. 5.

Next we want to compare the order of magnitude of this effect to the strength of an angular optical spring. If we call h the typical distance of the beam spot from the center of gravity of the mirror, and x the cavity length change at that spot, the order of magnitude of the optical spring torque is:

$$T \approx \frac{F_0 L}{1 - g_1 g_2} \cdot \frac{x}{h} \quad (2.15)$$

We can express this as the strength of an optical spring located at position h . The corresponding spring constant $K_{SS} \approx T/(hx)$. Thus we can see that

$$K_{SS} \approx \frac{F_0}{1 - g_1 g_2} \cdot \frac{L}{h^2}. \quad (2.16)$$

We now consider the adiabatic optical spring ($\Omega = 0$) in equation 2.7. Expressed in terms of F_0 , K_{OS} becomes

$$K_{OS} = iF_0 \frac{X - \bar{X}}{(1 - X)(1 - \bar{X})} 2k \quad (2.17)$$

Since we operate near the maximum of the optical spring, the order of magnitude of the resonance term can be estimated as

$$\frac{X - \bar{X}}{(1 - X)(1 - \bar{X})} \approx \frac{-i}{1 - |X|} \quad (2.18)$$

Thus we can estimate the magnitude of K_{OS} as

$$K_{OS} \approx F_0 \frac{4\pi}{\lambda} \frac{1}{1 - |X|} \approx F_0 \frac{4}{\lambda} \mathcal{F} \quad (2.19)$$

where \mathcal{F} is the cavity finesse. From equations 2.16 and 2.19 we see that the optical spring K_{OS} is much larger than the Sidles-Sigg instability spring K_{SS} if

$$h^2 \gg \frac{\lambda L}{\pi} \frac{1}{1 - g_1 g_2} \frac{\pi}{4\mathcal{F}} \quad (2.20)$$

Now recall that the beam spot size in a Fabry-Perot cavity is given by [10]

$$w_1^2 = \frac{\lambda L}{\pi} \sqrt{\frac{g_2}{g_1(1 - g_1 g_2)}} \quad (2.21)$$

Assuming a symmetric cavity ($g_1 = g_2$) for simplicity, we thus find that K_{OS} dominates over K_{SS} if

$$h^2 \gg w_{1,2}^2 \frac{1}{\sqrt{1 - g_1 g_2}} \frac{\pi}{4\mathcal{F}} \quad (2.22)$$

This condition is naturally fulfilled since we need to operate the angular optical spring with separate beams ($h > w_{1,2}$) and a large finesse ($\mathcal{F} \gg 1$). Therefore the angular optical spring is indeed strong enough to stabilize the Sidles-Sigg instability.

2.4 Radiation Pressure Noise

Another advantage of radiation pressure control, compared to a classical approach based on photo detection and feedback, is its fundamental noise limit. Unlike in the classical approach, the shot noise and other sensing noises never enter a radiation-pressure-based feedback loop. Even though technical laser noise is typically bigger

in the simple cavity setup discussed in this paper, the only fundamental noise source of the scheme is quantum radiation pressure noise. In this section we give the full expression for radiation pressure noise in the case of a dual-carrier stable optical spring.

First, we note that as long as we are interested in frequencies much smaller than the any of the features in the detuned cavity transfer function, the radiation pressure noise is relatively simple. If we also assume that the end mirror has a reflectivity of 1, the one-sided ($f \geq 0$) radiation-force amplitude spectral noise density is given by

$$S_F(f) = \frac{2}{c} G \sqrt{2\hbar\omega P_{\text{in}}} \quad (2.23)$$

where G is the power gain of the cavity in the detuned configuration, and P_{in} is the power of the shot noise limited beam entering the cavity. Equation 2.23 is valid for carrier and subcarrier separately. Note that this equation does not hold if the end mirror has a finite transmissivity, as quantum fluctuations entering from that port will also contribute to the intra-cavity shot noise. In the case of a critically coupled cavity, this will result in an increase of the intra-cavity radiation-force amplitude spectral noise density by exactly a factor of 2.

To calculate the exact expression for the radiation pressure noise induced cavity fluctuations, we first realize that we can calculate the radiation-force amplitude spectral noise for a static cavity, and then compute the response of the dual-carrier optical spring system to that driving force. This yields the correct answer up to first order in the size of the quantum fluctuations. For the calculation we track the quantum vacuum fluctuations entering at both ports of the cavity. It is useful to introduce a function F :

$$F(f) = F\left(\frac{\Omega + \delta + \omega_{res}}{2\pi}\right) = \frac{1}{1 - XY^2} \quad (2.24)$$

$$= \frac{1}{1 - r_1 r_2 e^{-2i\delta\tau} e^{-2i\Omega\tau}} \quad (2.25)$$

The amplitude build-up factors for fluctuations at frequency f entering through the input coupler (1) and the end mirror (2) thus are

$$t_1 F(f) \text{ and } r_1 t_2 F(f), \quad (2.26)$$

where we already dropped the one-way propagation factor because it drops out in the radiation force noise calculation below. We can now introduce the notation $F_0 =$

$F(f_0)$, $F_+ = F(f_0 + f)$ and $F_- = F(f_0 - f)$. We then get the following expression for the one-sided radiation-force power spectral density for either carrier or sub-carrier.

$$S_F(f) = \frac{2}{c} S_P(f) \quad \text{and} \quad (2.27)$$

$$|S_P(f)|^2 = \hbar\omega P_0 t_1^2 |F_0|^2 (t_1^2 + r_1^2 t_2^2) (|F_+|^2 + |F_-|^2) \quad (2.28)$$

Here P_0 is the entering carrier power, and f_0 is its frequency. We can see that we recover equation 2.23 in the limit $t_2 \rightarrow 0$ and $G/t_1^2 = |F_0|^2 = |F_+|^2 = |F_-|^2$. The resulting force noise from carrier and sub-carrier for the cavity A in the example above is plotted in Fig.9 (*top*).

Next we calculate the response of the coupled opto-mechanical system to this driving force, using the following closed loop transfer function obtained from equations 2.11 and 2.12:

$$x = M(1 - HM)^{-1}F \quad (2.29)$$

Above the optical spring resonances this leads to a $1/f^2$ fall-off of the displacement noise, as expected for radiation pressure noise. Meanwhile below the resonance, due to the closed loop suppression, we will have a flat displacement noise. Fig.9 bottom illustrates this in the case of the two-dimensional angular trap discussed above.

Finally we compare the resulting displacement noise to a classical photo-detection feedback control scheme with similar control bandwidth and control loop shape. If such a system is able to detect all available power and has no other dominating sensing noise sources, it can at best achieve a shot noise sensitivity of

$$S_x \sim \frac{l}{P_0} \sqrt{2\hbar\omega P_0} \quad (2.30)$$

where l is the cavity line width in meters. To have the same control bandwidth and loop shape the system needs a controller transfer function equal to the optical spring, $H = K_{OS} \sim \frac{2GP_0}{cl}$, and hence it will have a noise performance similar to equation 2.23, $HS_x = S_F$. Thus we find that the traditional control scheme can only achieve similar noise if all the power from the cavity is detected, and there are no other relevant sensing noise sources.

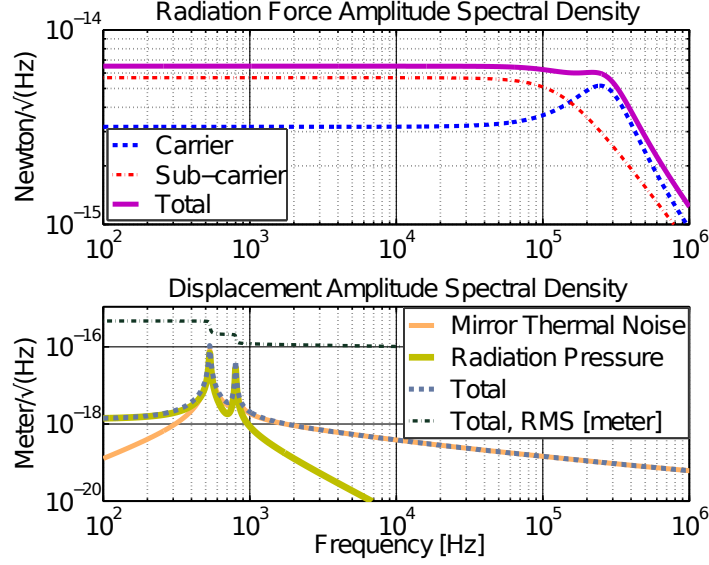


Figure 9: (*Top*) Radiation force amplitude spectral density for the dual-carrier optical spring used in beam A of the above example. The sub-carrier dominates the noise at low frequency, but the higher-power carrier contributes more at high frequencies. Also note that if we choose the same free spectral range for the two carriers, there would be an additional beat note at the difference frequency of 310 kHz. (*Bottom*) Radiation pressure and thermal noise displacement amplitude spectral density. The radiation pressure noise is calculated using the opto-mechanical response given in equation 2.29. The thermal noise is based on a theoretical calculation described in [5], [9]. Since seismic and suspension thermal noise depend on the experimental implementation, they are not shown, but they would also be suppressed by the optical spring closed loop response. The residual RMS motion due to the shown noise sources is less than 10^{-3} picometer. With the total RMS motion smaller than the 20 picometer stability band shown in Fig.8, the two cavities will remain locked purely due to the radiation pressure trapping force.

2.5 Technical Noise

In addition to the fundamental noises we have discussed, the experimental demonstration of this angular optical trap concept will be affected by several technical noise sources. These noises will impact our ability to acquire lock of the cavity, and will ultimately be the limiting factor for keeping the optical spring stable after removing active feedback.

Since the experiment relies on the force provided by a detuned cavity, the technical noises which will limit the experiment will ultimately show up as either mirror position noise or laser frequency noise. The two will be coupled through the optical spring, but we can think of the sources independently for now.

The laser source will have frequency noise of its own. Additionally, there will be relative frequency noise between the two beams.

Mirror position noise will come from seismic and other vibrational noise from the environment. Additionally, any amplitude noise in the laser will result in a radiation force noise on the mirror.

Performance of the experiment relies on reducing these technical noise sources. We will address and attempt to mitigate the laser frequency and intensity noises by implementing systems similar to a LIGO pre-stabilized laser (PSL). Seismic and mechanical vibration noises will be mitigated through a suspension system, and acoustic noise through the use of a vacuum system.

Chapter 3

Pre-Stabilized Laser

Technical noises from the laser itself can limit our experiment. [1] In order to reduce this noise we need active feedback systems to attenuate laser phase and intensity noise in the frequency band of our experiment.

Our experiment will be operating from a few hundred Hz to a few kHz. For this we have chosen to implement a system similar to the LIGO pre-stabilized laser (PSL). This is composed of three systems: frequency stabilization servo (FSS), pre-mode cleaner (PMC), and intensity stabilization servo (ISS).

The PMC cleans the beam spatially for the ISS photo-diode (PD)s. We have this system so that we stabilize the intensity of the spatial mode which couples to the experimental cavity. Without the PMC we would add noise to the TEM_{00} mode from any intensity noise fluctuations of the higher order modes that are uncorrelated with noise in the TEM_{00} mode.

The ultimate goal is to eliminate noise from active feedback. In order to accomplish this, the other noises (ch.5) entering the system must be much lower than the stability region described in section 2.2.2. In the absence of an optical spring, the rms noise coupling to cavity detuning comes from the low frequency seismic motion. An optical spring of several hundred Hz suppresses the seismic motion significantly and the dominant noise source is the resonantly enhanced noise around the spring frequency. We will need to reduce this noise in order to ultimately turn off the active feedback.

Our PSL is based on the LIGO PSL, the three main components of which are the ISS, FSS, and PMC. Each system has been commissioned in part and as a

whole. However, the integration of these systems with the experiment required some modifications that were not complete at the time of this writing.

As we will see in chapter 6, we are limited by laser intensity and frequency noise, so having these systems integrated will improve future optical trap experiments.

3.1 Laser Head

We start with a Mephisto 2 Watt laser head with an integrated intensity noise reduction system.

This laser has good noise characteristics on its own. It is a neodymium-doped yttrium aluminum garnet (Nd:YAG) non-planar ring oscillator (NPRO) laser. The monolithic cavity allows for an extremely small spectral linewidth of less than 1kHz full width at half max (FWHM). The NPRO is characterized as having a frequency noise amplitude spectral density which is proportional to $1/f$, where f is the frequency of the noise fluctuations of the laser frequency. At 1kHz the frequency noise is $10\text{Hz}/\sqrt{\text{Hz}}$.

The noise eater option gives a relative intensity noise (RIN) of less than -150dB/Hz per the specification sheet. RIN is the noise level of the laser power relative to the average laser power. The average laser power is sometimes referred to as the DC power or carrier power. It is fairly standard to specify RIN with the slightly confusing units of dB/Hz. This is actually dB relative to carrier power or dBc. The confusing part is that 20dB, which is normally a factor of 10 in amplitude is actually a factor of ten in laser power. It *is* however a factor of 10 in the amplitude of the voltage read from a PD. This is important when trying to compute the radiation pressure noise in $N/\sqrt{\text{Hz}}$, for example.

The RIN specification is actually for frequencies above 100kHz. We're actually interested in the intensity noise at frequencies much lower than this so we measure the the noise in the lab. With the noise eater on, the RIN we measure is $\frac{\text{RIN}}{\sqrt{\text{Hz}}} \leq \approx 10^{-6}$ above 100Hz (see figure 31).

The NPRO's lasing medium is one solid piece of Nd:YAG with four internally reflecting surfaces that form a ring shaped cavity. Three points define a plane, the addition of the fourth mirror outside of this plane enables a rotation of the polarization of the laser for each round trip around the ring. With the addition of a permanent

magnet, there will be a Faraday rotation as well which is dependant on the direction of the laser around the ring. For one direction the polarization rotation from the two effects are cancelled. In the other direction, the polarization rotations are not cancelled and light leaks out of the cavity at a rate higher than the gain of the medium due to a slight polarization dependent reflection of the input mirror. The output beam ends up with a very narrow linewidth but a slight elliptical shape.

3.2 Intensity Stabilization

The ISS uses a PD for sensing the laser power from a pick-off beam after the PMC. This gives us sensing of the amount of power in the TEM₀₀ mode of the laser we are using for our experiment. The signal is fed back through an electronic servo to an actuator that modulates the intensity of the beam before the PMC. The actuator is an accousto-optic modulator (AOM).

3.2.1 Sensing

The PD works by the photoelectric effect. There is a quantum efficiency associated with each PD which is the amount of light quanta (photons) which are converted into electrical current.

$$q.e. = \frac{N_{el}}{N_{ph}} \tag{3.1}$$

$$= \frac{I/e}{P/(\hbar\omega)} \tag{3.2}$$

$$= \frac{2\pi\hbar c}{e\lambda} \frac{I}{P}, \tag{3.3}$$

where e is the elementary charge.

This relates the power of the incident light to the current in the output of the PD. Photodiode quantum efficiency is usually specified in Amps per Watt. This must naturally be dependent on the wavelength of the light, so they must also specify a wavelength.

We are limited by noise due to counting statistics (shot noise). We want a high signal to noise. In this case, the signal that we are concerned about is the relative fluctuation in power, and so it is proportional to the DC incident power on the PD. The

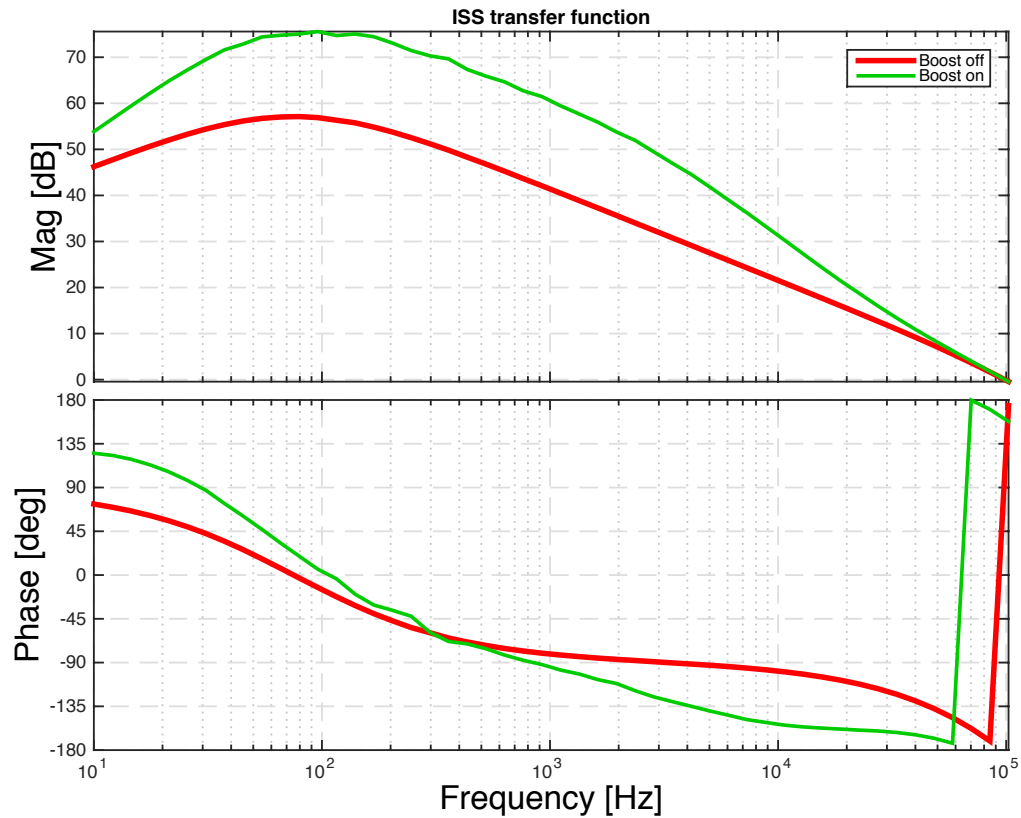


Figure 10: intensity stabilization servo transfer function. This is the open loop transfer function for the ISS. The feedback is AC coupled to prevent large DC offsets in the actuator. There is a switch to turn on a boost stage which gives another factor of 10 in gain at frequencies between 40Hz and 4kHz. This is where our optical spring frequency will be and where we will be most affected by the noise.

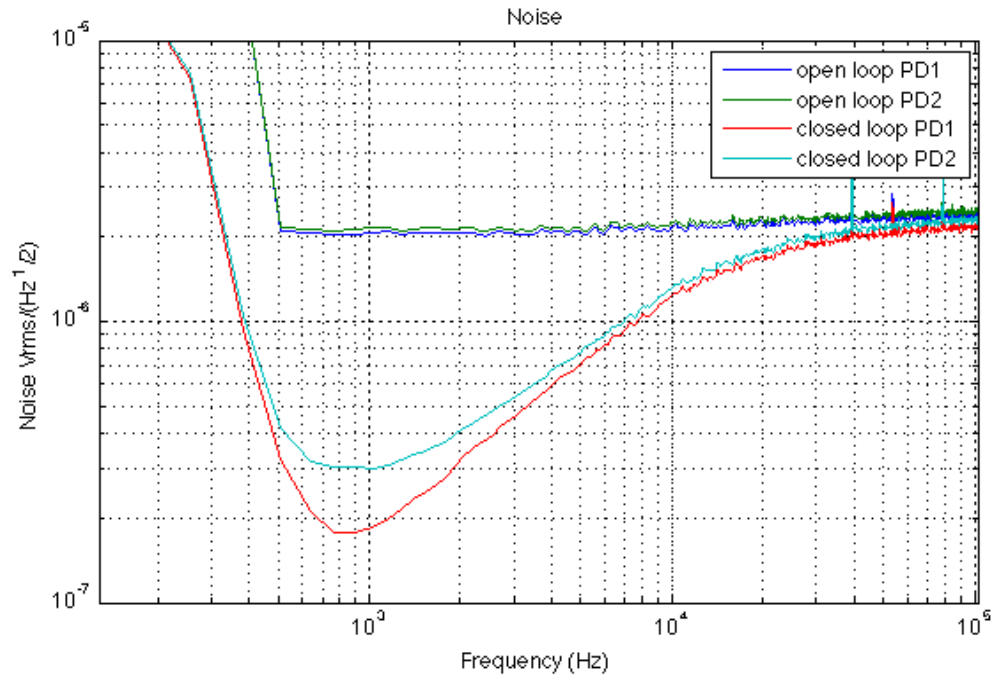


Figure 11: intensity noise with loops closed. This plot shows the amount of noise suppression we were able to achieve without the PMC in place. PD1 is the photodiode used for sensing in the active feedback loop. PD2 samples the same light but is not in the loop. This allows us to measure the actual residual intensity noise, since the servo will imprint any sensing noise from PD1 onto the laser intensity.

noise, as a Poissonian process, is proportional to the square root of the DC power (or the number of photons per second).

The RIN becomes the photon counting error divided by the total number of photons.

$$\text{RIN} = \frac{\sqrt{N_{el}}}{N_{el}} \quad (3.4)$$

$$= \frac{1}{\sqrt{N_{el}}} \quad (3.5)$$

$$= \frac{1}{\sqrt{q.e. \times N_{ph}}} \quad (3.6)$$

$$= \sqrt{\frac{\hbar\omega}{q.e. \times P\tau}}, \quad (3.7)$$

where τ is the integration time. This allows us to write the amplitude spectral density of the shot noise in $\text{RIN}/\sqrt{\text{Hz}}$ as,

$$\sqrt{\frac{2\hbar\omega}{q.e. \times P}}, \quad (3.8)$$

where the 2 is due to the choice of one-sided spectra.

3.2.2 Actuation

Actuation, as mentioned above, is accomplished using an AOM. The AOM is a device which can modulate a laser beam in both frequency and intensity. It works by using bragg reflections in a crystal with travelling waves. The interaction between the travelling waves and crystal lattice divert the beam to different orders of refraction. The power in each order is dependant on primarily the amplitude of the travelling waves. The diffraction angle is dependant on the wavelength of the travelling waves. We take the zero order refraction and modulate on the intensity of the waves which, in turn, modulated the amount of power diverted into higher order Bragg refractions.

3.3 Frequency Stabilization

The FSS is an active feedback system which stabilizes the already quite narrow frequency from the laser. The system is composed of a rigid laser cavity which is used as a reference which we can lock the laser frequency to. The laser frequency follows the length of the reference cavity up to several kHz.

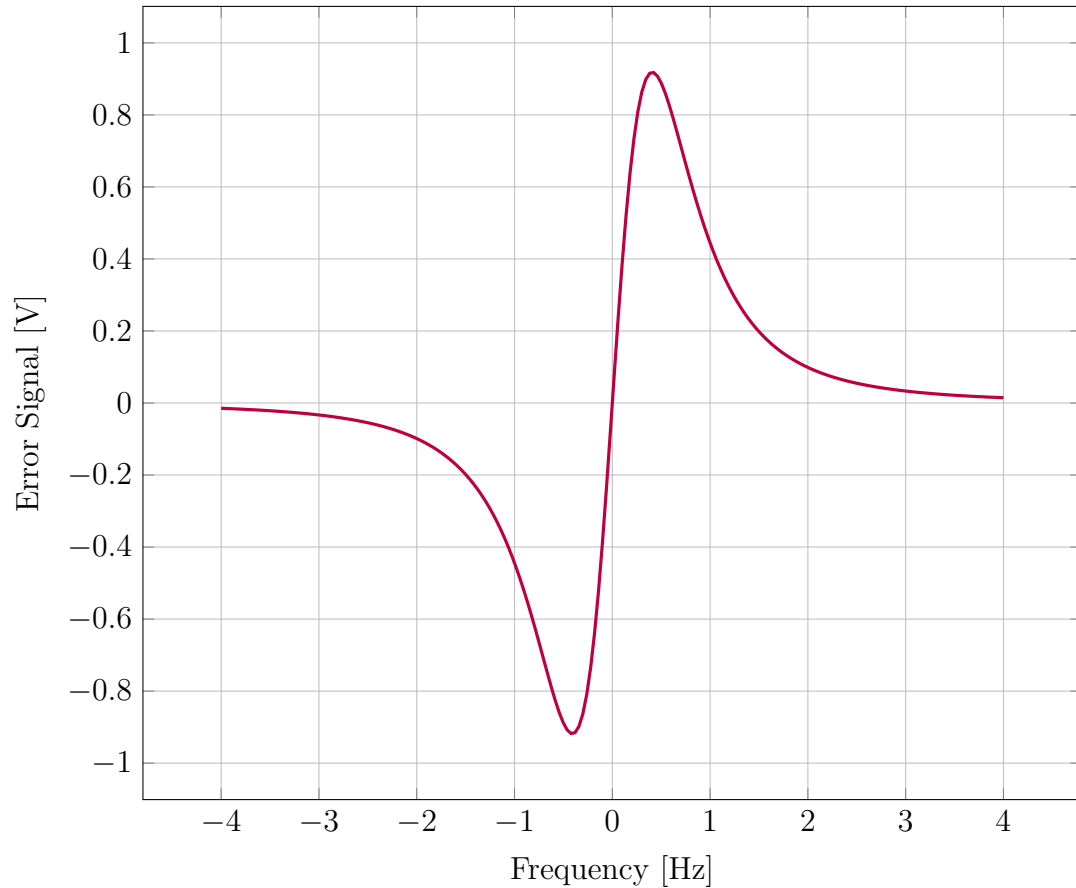


Figure 12: This shows the PDH error signal of a simple cavity. Our lock point must be between the positive and negative cavity poles (maximum and minimum on the y-axis).

3.3.1 Sensing

Sensing for the FSS is accomplished using the method of Pound Drever Hall (PDH) [11]. The signal is essentially the derivative of the reflected power with respect to frequency of the laser (assuming length is fixed). This is accomplished by modulating the frequency of the input beam with an electro-optic modulator (EOM) driven by a 25MHz local oscillator and demodulating the reflected beam with the same local oscillator. The result is a signal on resonance that is zero and has maximum slope (see fig.12). Exactly the signal we want for a feedback system which keeps the laser on resonance with the cavity.

Cavity Assembly

The reference cavity is a Fabry Perot made from an 8 inch monolithic fused silica spacer with high reflectivity mirrors glued onto the ends. The reflectivity of the mirrors yield a finesse of about 7600. Finesse is defined as the ratio of the free spectral range (FSR) to the cavity linewidth (FWHM).

Cavity Suspension

The reference cavity is suspended with wires and coil springs from an aluminum frame. The design of the frame can be seen in figure 13. Eddy current dampers were added to damp the resonances. This was done by attaching vertical aluminum plates to the bottom of the cavity. One was oriented longitudinally and one laterally. U-shaped steel channels were attached to the aluminum frame to close the magnetic field lines of the damping magnets.

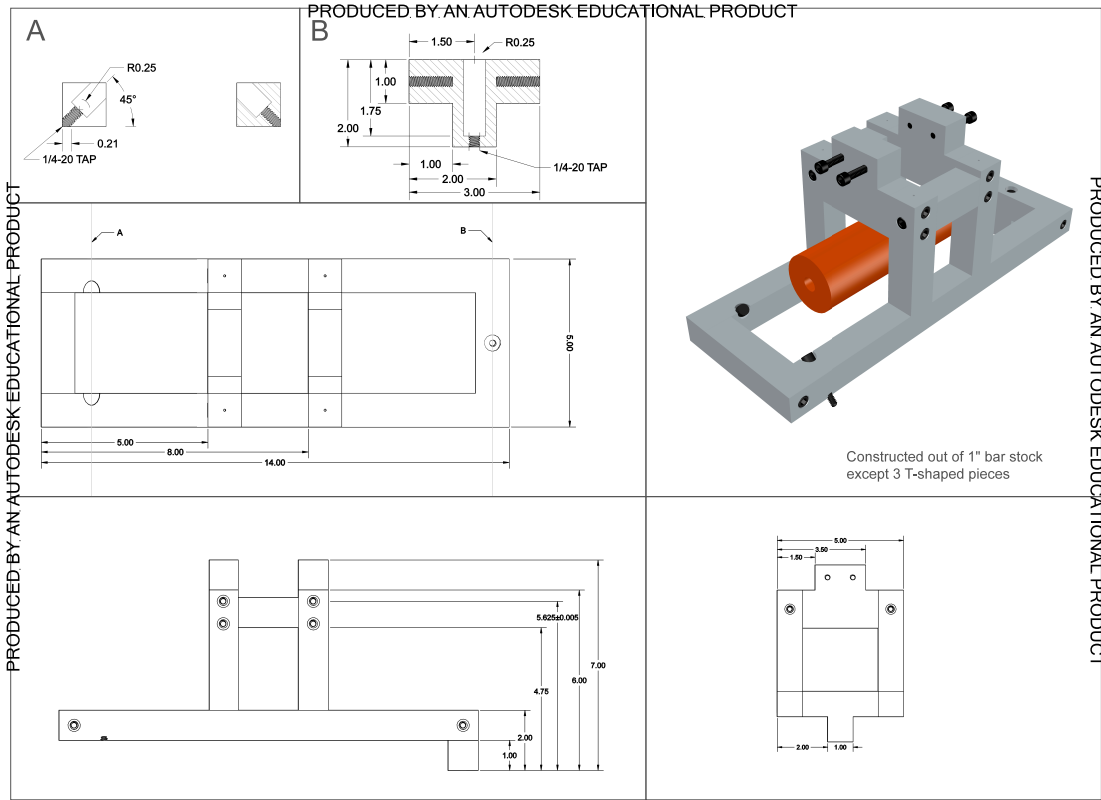
3.3.2 Feedback

The feedback electronics used for the FSS are from initial LIGO. The board provides feedback signal for 2 different actuation paths with a crossover frequency of 10kHz. The low frequency path actuates on the laser frequency by changing the laser cavity length. The other path is to an EOM to actuate on the phase of the laser beam.

The low frequency path is split again into two different actuation paths with a crossover frequency of about 10Hz. Below the crossover the laser cavity length is changed by thermal expansion. Above the crossover the actuation is by piezo electric transducer (PZT).

3.3.3 Actuation

There are three actuators. Low frequency actuation is by a thermal controller in the laser head which actuates on the the cavity length through thermal expansion. The mid frequency actuation is by PZT which applies a force to change the cavity length. The high frequency actuation is by phase modulation of the light after it exits the laser head using an EOM.



Constructed out of 1" bar stock except 3 T-shaped pieces

PRODUCED BY AN AUTODESK EDUCATIONAL PRODUCT

Figure 13: design of the reference cavity suspension. Eddy current dampers were added to this suspension design by attaching two U-shaped pieces of steel to the frame and two aluminum paddles to the reference cavity. Permanent magnets were attached to the steel to create a magnetic field which the aluminum paddles are suspended in. Motion of the reference cavity in relation to the suspension frame creates eddy currents in the aluminum which damp the motion.

Chapter 4

Linear Trap Experiment

In designing the experiment we knew that frequency noise would be a primary limiting factor. For the goal of reaching the quantum noise limit, we can also be limited by thermal noise of the suspensions and coatings. Seismic noise can be attenuated quite well by choosing a higher frequency.

With these limitations in mind we designed the trap cavity and the supporting optics and electronics.

4.1 Design Considerations

We want our optical spring frequency to be high enough so the experiment is not limited by seismic noise. Without the resources for elaborate seismic isolation we are limited to single pendulum isolation stages with a natural frequency of order 1Hz. At 1kHz we have seismic motion below $10^{-12}\text{m}/\sqrt{\text{Hz}}$. With a pendulum isolation we can attenuate at 1kHz by a factor of 10^{-6} . Assuming we have a cavity length of order 30cm we can assume a corresponding frequency noise of about $1\text{mHz}/\sqrt{\text{Hz}}$. This is well below the free running laser noise of the NPRO laser of about $10\text{Hz}/\sqrt{\text{Hz}}$ at 1kHz (see section 5.3).

To achieve this resonant frequency we will need to have a small mass. Just how small is determined by the dP/dL dependance that gives us the optical spring constant. For a high finesse, it can be shown, by taking the derivative of the intracavity

power, that the maximum spring constant for a given power is approximately

$$k = \frac{3^{5/2} F^2}{\pi \lambda c} P. \quad (4.1)$$

This gives us a minimum mass of

$$m = 3^{5/2} \frac{F^2}{\pi \lambda c \omega_0^2} P. \quad (4.2)$$

Additionally, we need a high Q suspension for the small optic in order for the spring stability to be dominated by the optical field. The optical spring will have fairly low phase since we will be operating a frequency much lower than the cavity pole.

We use a smaller cavity in order to reduce the effect of frequency noise. The frequency noise couples in by the ratio of the cavity length and laser frequency.

As described in section 2.1 if we choose a sufficiently heavy mass for the input mirror, the angular stability of the small mass is governed by the following effective angular spring constant,

$$T = \frac{F_0 L}{1 - g_1 g_2} g_1 \theta \quad (4.3)$$

By choosing negative g-factors we get the stable angular mode for the small mirror since the large mirror is essentially fixed.

Ultimately, we wanted to lower the frequency impact of frequency noise, so we chose a short cavity. Since the linewidth of the resonance is fixed in terms of cavity length ($\text{FWHM}(m) = \lambda/\mathcal{F}$) it is natural to convert the frequency noise to cavity length. The cavity length noise is related to the frequency noise by,

$$\delta L = \delta f \frac{L}{f}. \quad (4.4)$$

By using a shorter cavity, we reduce the effect of frequency noise by geometry alone.

The cavity length is related to the radius of curvature by the fact that we want negative g-factors, which constrains the length to 1 to 2 times the radius of curvature (for the case $g_1 = g_2$). With the off the shelf substrates available at the time, we chose to use a 5cm radius of curvature for both input and output mirror.

Incedentally, the sizes of the mirrors available with a 5cm radius of curvature are quite small. We chose the smallest one for the output mirror, which gave us a

Parameters of Trap Cavity		
Parameter	Value	
Cavity Length	7cm	L_0
Coating Reflectivities	0.99979	r_1, r_2
Radius of Curvature	5cm	$\mathcal{R}_1, \mathcal{R}_2$
Test Mass Mirror	0.414g	m
Input Mirror Mass	300g	M

Table 1: Trap Cavity Parameters for the experiment.

payload mass of about 0.41 grams, well within our criteria for optical spring resonance frequency.

In order to avoid higher order modes near the resonance we examined the resonance condition for the first ten orders. We determined that with a radius of curvature of 5cm, we could avoid these modes well with a cavity length of 7cm.

These criteria lead us to the experimental parameters listed in table 1.

4.2 Suspension Systems

For seismic isolation we have 30cm pendulums attached to the lab optics table. The table is suspended on pneumatic legs which provide additional isolation above about 1Hz. For the input mirror, the mirror is fixed to the pendulum mass. For the output mirror (payload), the mirror is suspended from the pendulum mass using thin fibers (see figure 22).

4.2.1 Payload Suspension

We want the suspension to have a high Q and low resonant frequency. The high Q reduces thermal noise in the area of interest (above the resonant frequency). And the low resonant frequency gives us better seismic isolation at high frequencies

With a lower resonant frequency, the response of the mirror due to a force from radiation pressure is unchanged as long as the resonant frequency is sufficiently lower than the operating frequency. This can be shown by the transfer function of force

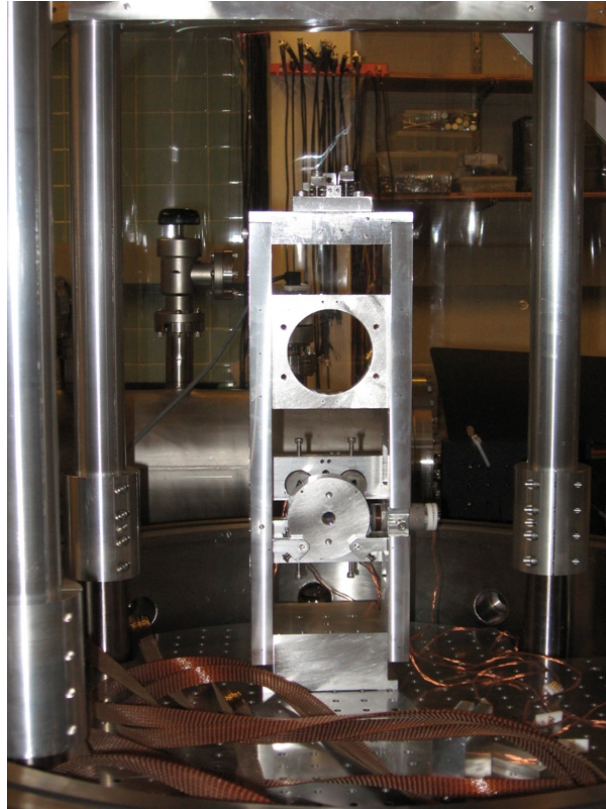


Figure 14: This shows the full small optic suspension tower. This is based on the LIGO SOS design. We modified the tower base in order to get the mirrors closer together. You can see in this picture the base is flush with the front of the vertical side plates. This suspension was modified after first cavity lock to further improve seismic isolation using blade springs depicted in figure 15. The extra length of cabling is for suspending the OSEM connection block in case the entire platform is suspended as an extra level of seismic isolation. In this case, suspending the connection block may be desirable to reduce seismic coupling to the platform through the stiff vacuum cabling.

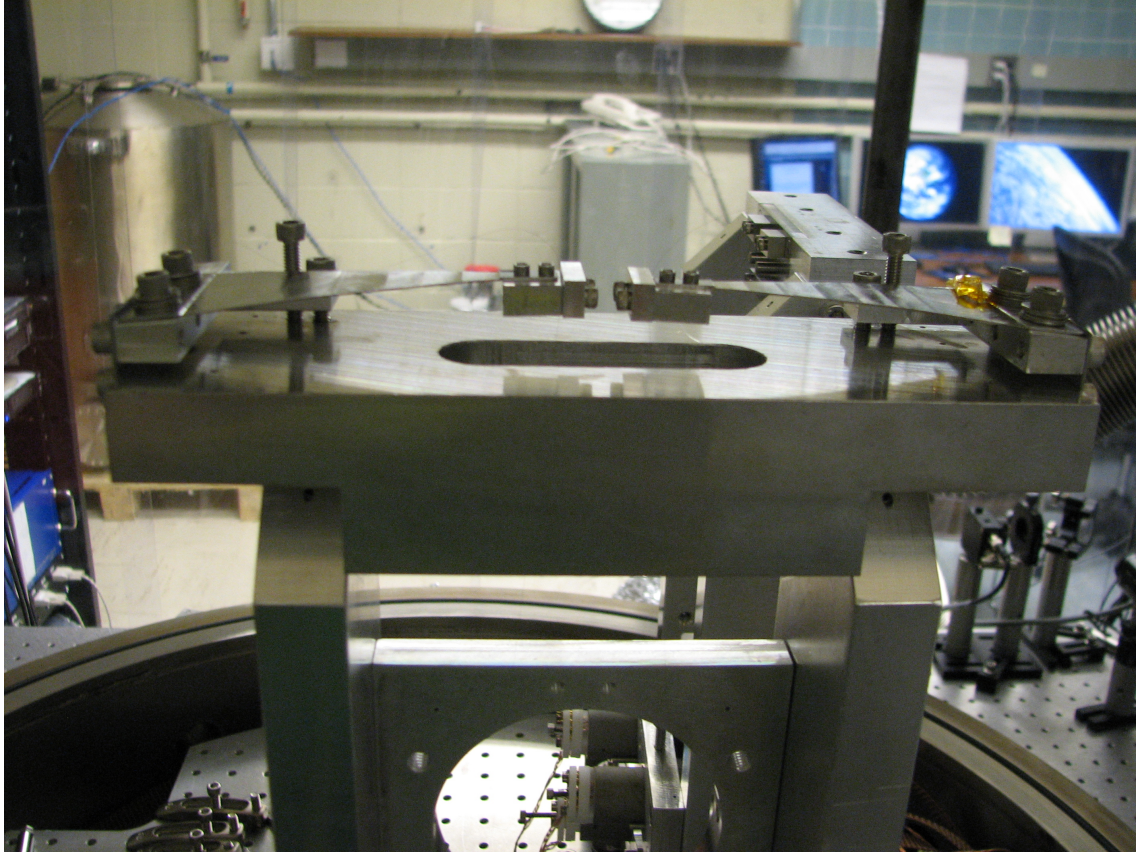


Figure 15: This is a picture of the blade springs as installed on one of the suspension towers. This was necessary for additional bounce mode suppression of seismic noise. The bounce mode of the suspension wires were at about 22Hz. This unfortunately, was very close to a peak in our seismic spectrum resulting in too much vertical motion in our suspended mirrors. With the addition of the blade springs, we ended up with a bounce mode of about 7Hz providing more suppression of the seismic by moving away from a seismic peak as well as the additional suppression from a lower frequency mode. See section 5.1.

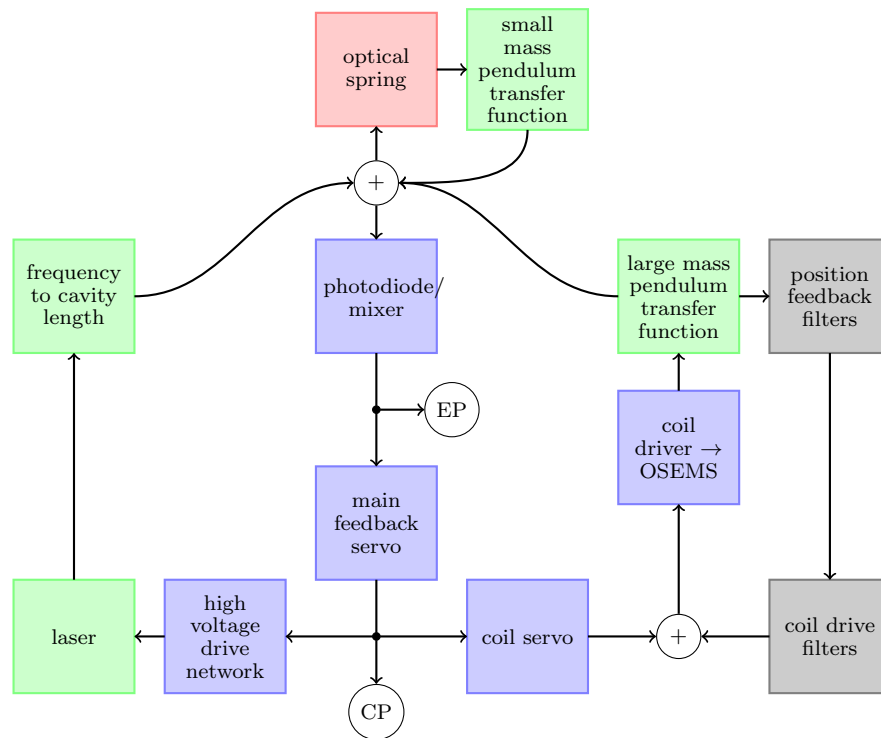


Figure 16: This chart depicts the feedback scheme used for locking the trapping cavity and observing the spring behavior.

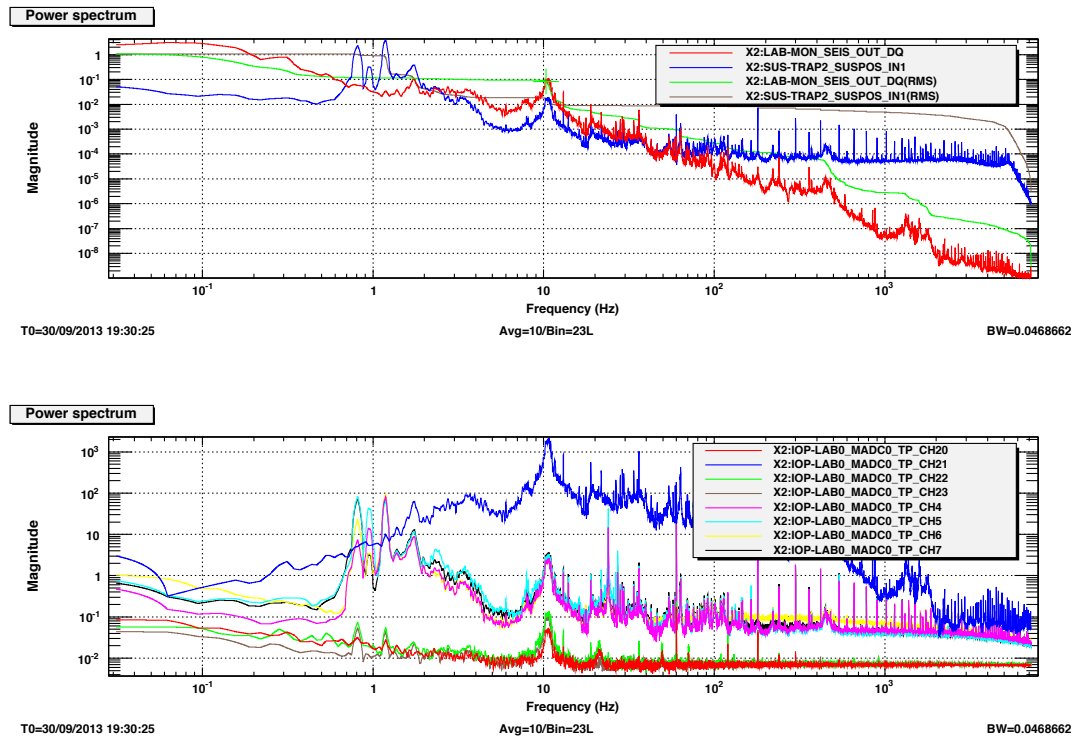


Figure 18: background seismic noise. The units in the top plot are $\mu\text{m}/\sqrt{\text{Hz}}$. The bottom plot is in counts from the analog to digital converter. The red trace in the upper plot is from the seismometer. The rms motion due to the noise around 500Hz is about $10^{-4}\mu\text{m}/\sqrt{\text{Hz}}$. This is about a factor of 10 too much for our experiment just from the point of view of the stability criteria. The bottom plot of the signals in counts shows the relative strength of the signals into the digital system. Channels 20, 22, and 23 show the noise floor digital inputs. The 10Hz peak shows up in the empty channels due to a small amount of crosstalk between channels. This plot shows that even though the seismometer input is quite high, the amount of crosstalk is low enough to not be a concern for us.

applied a mass on a spring. From force to position, this is,

$$H = \frac{1}{k - m\omega^2} \quad (4.5)$$

$$\approx \frac{1}{-m\omega^2} \quad (\omega \gg \omega_0) \quad (4.6)$$

and is then independent of the spring constant. The mass acts as a free mass.

For the seismic isolation, however, there is a dependance on the spring constant. In this case the transfer function from a position displacement at the attachment point of the spring to the position of the mass looks like,

$$H = \frac{k}{m\omega^2 - k} \quad (4.7)$$

$$\approx \frac{k}{m\omega^2} \quad (\omega \gg \omega_0) \quad (4.8)$$

In designing the suspension for the small mirror we went through the thermal noise analysis to determine the best approach. We wanted to suspend the small mirror using thin glass fibers with a low tension for isolating the mass from vibrations in the next mass up in the chain. Thin fused silica fibers are desirable for seismic isolation suspension due to the very high quality factor achievable. [12]

The initial thermal noise analysis was for the glue used to mount the glass fibers to the small mirror. This analysis is described in detail in the noise chapter. We designed the glue joints of the suspension to minimize thermal noise based on the analysis. The result of the analysis was to have a small mass at the glue end of the fiber with a center of gravity close to the glue surface.

Glass Fibers

We needed glass fibers in the final suspension for the high quality factor. These were produced by heating up a thin section of fused silica and pulling abruptly while removing the heat. The resulting fiber has an incredibly high tensile strength and quality factor.

The ratio of tensile strength to weight makes fused silica an ideal material for seismic isolation. Seismic isolation is limited by standing waves in the suspension fiber. This effect is analogous to that from surging in coil springs. The mass is not as well isolated above the violin modes as the $1/m\omega^2$ of the free mass. See, for example, Winterflood[13].

In our lab we use a small hydrogen and oxygen torch. The procedure used for the suspension fibers in gravitational wave detectors is similar except that CO₂ lasers are used instead of a flame and the process is automated.

Prior to the actual fiber pulling some preparation work with the torch must be done to get the right shape for the preform. We prepare the preforms by making a small point on each where the fiber will connect the two pieces. The preform work is done with a torch as well. In our case the preform work was done with a larger torch. The rod preform is created by heating a rod with a torch and pulling it apart to form a cone shape at the end of the rod. The tip of one cone is then used to weld a nub of glass onto the side of the mirror. Then, using a small torch we weld the tip of the preforms together and pull abruptly while removing the torch.

The length and diameter of the fibers can be controlled somewhat and becomes a bit of an art in practice. In general, though, one can vary these parameters through the choice of torch tip size, pressure of gases, and the starting size and shape of the glass rod. In the end, generating the right fibers requires the sort of finesse that has nothing to do with optical cavities.

Welding Fibers to the Mirror

The procedure of directly welding to the mirror was a challenge. The first few attempts produces clearly visible damage. We needed to protect the coating from the hot gases of the torch by employing a holder made of graphite.

After upgrading the fiber welding process with the graphite holders we could weld fibers to the mirror without producing any obvious damage. The mirror produced from this was used in a cavity with another mirror of the same coating run.

The finesse of a cavity using mirrors from the same coating run was about 8000 but the finesse of this cavity was only about 800. The exact nature of this degradation is currently unknown, but since the finesse is high (800 is still pretty high), the damage to the optic resulted in only about 0.31% more in additional losses either in absorption or scattering.

The order of magnitude lower in finesse was far too much for the experiment. So, we came up with a method of glueing the fibers to the mass.

Glued Fiber Attachements

It may be that the coating of the welded mirror was damaged directly from the heat in the substrate, though the melting point of the Ta₂O₅ is higher than the temperature of the substrate during welding. It is also quite possible that some of the graphite was deposited onto the coating and remained despite attempts to clean the coating or that the coating was damaged during handling.

It would be interesting to find out the exact cause of the damage and possibly refine the welding procedure. Though not immediately useful since we decided to go for glueing the fibers to the small mirror instead.

The final suspension design for this experiment used small cone-shaped glass nubs at the glue end of the fibers. This could be constructed monolithically by cold welding¹ the tip of a glass rod to a small mirror blank² to create a small nub from which the fiber is pulled.

After creating the glass rod preforms, this procedure is done in one continuous motion. The torch is applied to the edge of the mirror blank to gently heat the point of attachment, then the rod with a sharp point is placed into the flame to melt the tip and cold weld to the edge of the mirror. The flame is then directed at the tip of the rod slightly back from the weld to soften the fiber pull spot. When the spot is sufficiently heated, the fiber is pulled away sharply while dropping the flame away from the fiber. What remains is a rod attached to a small conical shaped nub monolithically through a very thin, high Q fiber.

The cold weld allows us to separate this monolithic fiber assembly because the bond strength is much less than the yield strength of the fiber.

We then glue this monolithic fiber assembly using the epoxy to the side of the mirror with undamaged coatings. This technique allows us to preserve a very high Q ($\approx 5 \times 10^5$) while avoiding damage to the coating. The results of a Q ringdown measurement can be seen in figure 19.

¹a process where the substrate is not heated to the point where the materials flow together

²or a mirror with a previously damaged coating...

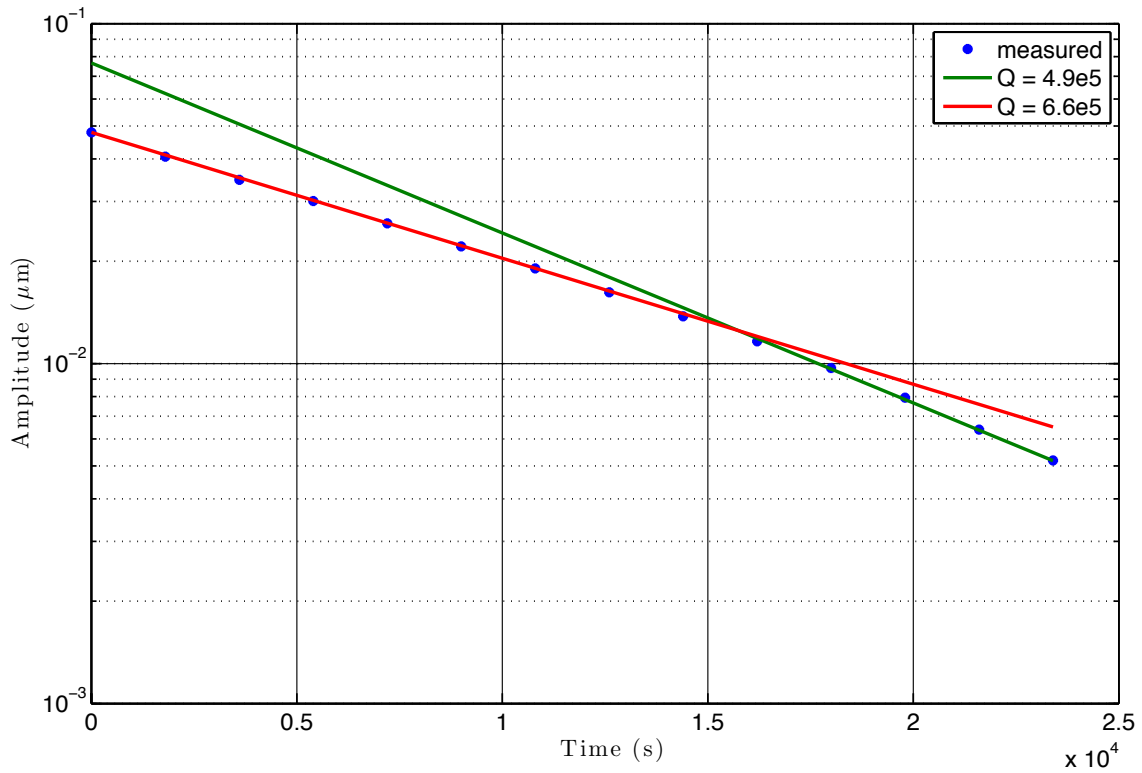


Figure 19: This ringdown measurement was done by exciting the $\approx 18\text{Hz}$ position resonance and measuring the rms motion across the resonant frequency from an ASD measurement of the OSEM position resonance. The OSEM position signal is of the metal ring intermediate mass of the output mirror suspension as described in section 4.2.2.

4.2.2 Intermediate Suspension

We have engineered the assembly for the small mirror to have about the same mass and dimensions as the input mirror assembly. Both of which fit nicely in a LIGO designed small optic suspension.

The original design of this suspension had no vertical isolation aside from stretching of the metal suspension wire itself. This mode was about 22Hz and there was no active damping. We modified the design to incorporate blade springs for better vertical isolation with a mode of about 7Hz. These suspension towers can be seen in figures 14 and 15.

The vertical isolation mode is still not damped directly, although we can damp indirectly since the suspension has some vertical to horizontal coupling. We needed to move the resonance frequency away from some large peaks in the background seismic. Moving the resonance down in frequency also helps reduce the amount of vertical seismic motion that couples into the cavity length.

Double Pendulum

The output mirror is suspended by glass fibers inside a ring of steel which is three inches in diameter. The steel ring is the SOS controlled mass. Since the mass of the ring is considerably greater than the mass of the small mirror, the transfer function for force to position on the small mirror can be approximated by simply the small mirror mass and resonant frequency. For the complete solution, the equations of motion that need to be solved for one dimension (per mass) are,

$$F_{1\text{ext}} = m_2 a_2 - k_2 x_2 + k_1 (x_1 - x_2) \quad (4.9)$$

$$F_{2\text{ext}} = m_1 a_1 - k_1 (x_1 - x_2) . \quad (4.10)$$

This system can be modelled by a double pendulum as seen in figure 20. One can also present the equations of motion diagrammatically as in figure 21.

4.3 Experimental Layout

As a reminder, we need two beams at different frequencies to couple into the cavity. We employ an optics path with active control on the frequency offset between the two beams which we call the "subcarrier servo".

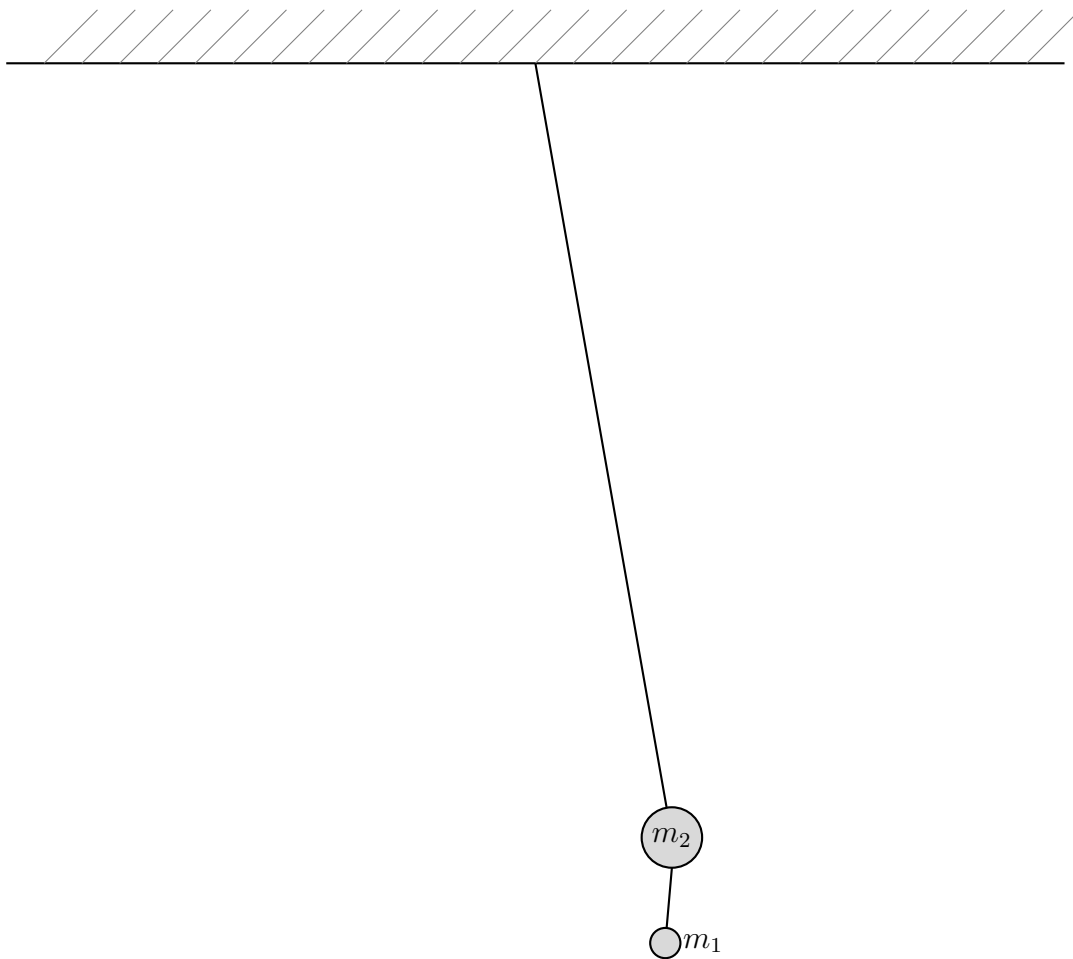


Figure 20: The double pendulum system representing the small mirror suspension. For small oscillations the pendulum and spring give equivalent equations of motion by $k = \sqrt{gm/l}$. m_1 represents the small mirror and m_2 represents the steel ring. If the system depicted here was a scale model of the actual small mirror suspension, the relative size of the masses and lengths of the pendulums would be more extreme.

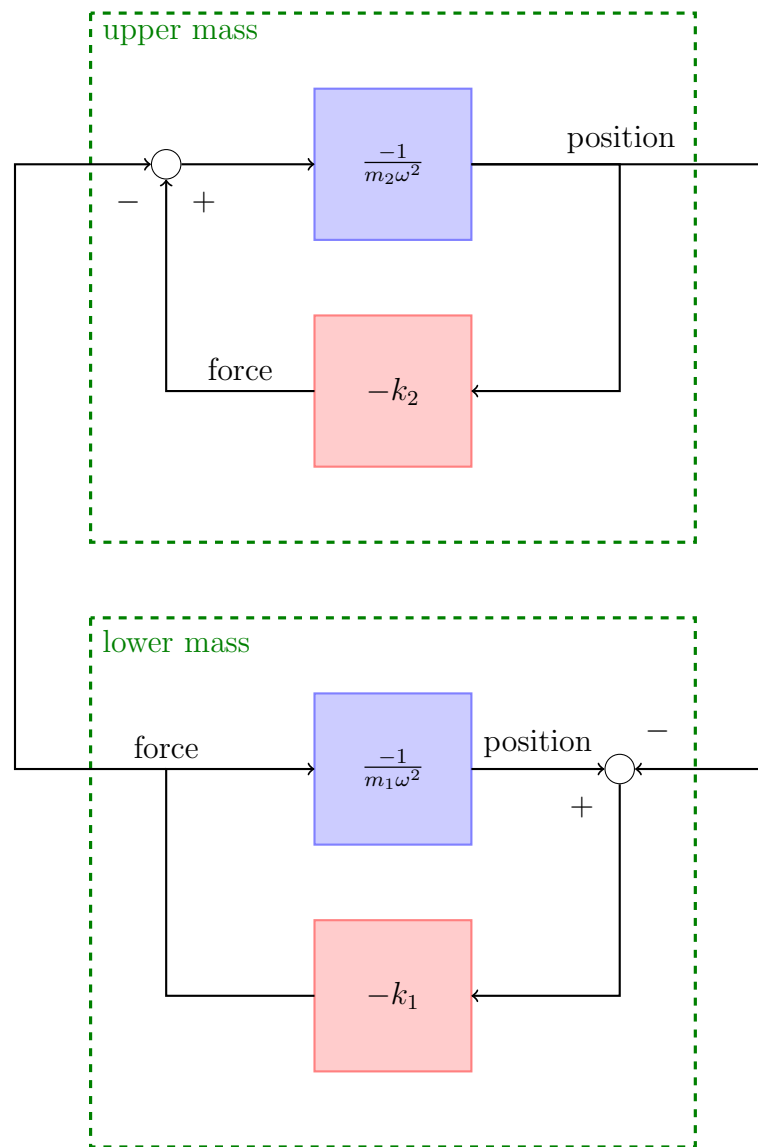


Figure 21: feedback representation of double pendulum. This diagram represents the double pendulum feedback loops from which one can calculate the response of the system. The upper and lower masses form a feedback loop with the upper mass position and the lower spring (pendulum) force.

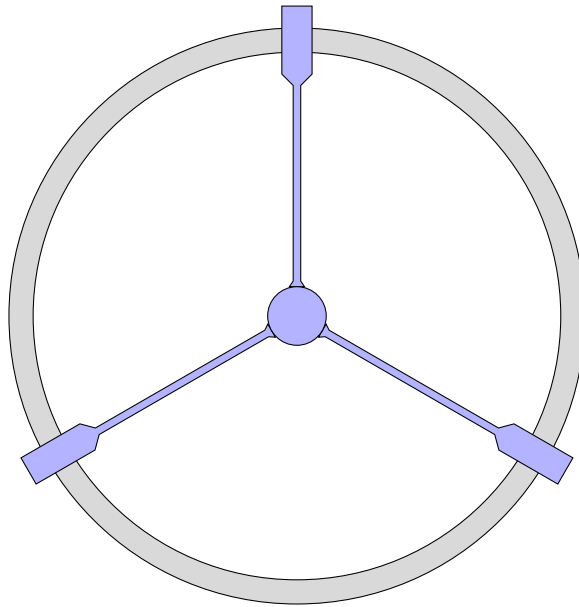


Figure 22: The small mirror suspension intermediate mass (gray) is a 3 inch diameter steel ring about 1/4" thick and 1" deep. The small mirror itself is a 7.75mm diameter fused silica substrate with a 5cm radius of curvature. The suspension fibers are monolithic to a small conical nub which is glued to the outside edge of the mirror.

frequency of about 2.14GHz. This produces a technical problem in attempting to set the subcarrier on the next resonance, one FSR away. AOMs are limited in the range of frequencies they can operate in. The minimum is higher than the linewidth for our cavity. The maximum is less than FSR.

The solution for us was to set the subcarrier on the same resonance fringe using two AOMs, each one shifting the frequency by about 80MHz in opposite directions. One is driven by a crystal oscillator. The other is driven by a tunable oscillator, a voltage controlled oscillator (VCO), which gives us the knob to detune the subcarrier.

We produce a beat signal between the two oscillators and we lock the beat signal to a function generator operating in the range of frequencies we are need to detune the subcarrier with. So, now we can set directly, the carrier to subcarrier offset frequency using the knob on the function generator. This setup essentially eliminates frequency noise due to the crystal oscillator, which is quite low to begin with, since we are subtracting the same, coherent, frequency noise with the second AOM. And the frequency noise due to the function generator is lower due to the fact that we are using a lower frequency tunable oscillator. Tunable oscillators generally have a frequency noise that is relative to the set frequency. The subcarrier servo is discussed in more detail in section 4.5.

4.4 Locking Challenges

4.4.1 Optical Lever

We found the small mirror resonances to be strong enough to prevent locking the trapping cavity. Our solution to this was to employ an optical lever, where a laser is reflected off the back of the small mirror and onto a quadrant photodiode (QPD). The photodiode outputs a signal corresponding to the pitch and yaw of the small mirror.

Using the signal from the QPD as the error signal we feed back to the OSEM actuators using digital filtering. We employed resonant gain filters in the optical lever loops to damp resonance modes as necessary to acheive stable locking.

4.4.2 Actuation Range and Bandwidth

Due to seismic noise we needed a fairly wide actuation range at low frequencies. The maximum range of the laser PZT is plus or minus 160MHz. This corresponds to about 42nm. As can be seen in figure 18 there is more rms motion than this at low frequencies.

We needed another actuation path to cover the full range of rms motion at low frequencies. For this we use the magnetic force from the OSEM coils. From the OSEM coils, we calibrated a force per voltage (voltage input to current driver board) value of 2×10^{-5} N/V per coil. With four coils we get a force range of about $\pm 8 \times 10^{-4}$ N for the suspension. Most of the rms motion will come from the 18Hz resonance of the payload suspension which is undamped. At this frequency we are well above the pendulum frequency of the input mirror suspension so we can treat the input mirror as a free mass. The actuation range at this frequency is then 2×10^{-7} m.

While attempting to acquire lock, the cavity mirror motion is much larger than the linewidth of the cavity. As a result, the PDH error signal (fig. 12) sweeps through rapidly. Looking at the signal in the time domain (as with an oscilloscope), the width of the PDH error signal is about 50μ s. One can imagine that we would want a bandwidth of at least $\approx 1/50\mu$ s = 20kHz. In fact a unity gain frequency of about 20kHz turned out to work well for acquiring lock.

To get this bandwidth a modification to the laser PZT actuation path was required. The high voltage amplifier for the laser PZT was limiting our bandwidth due to it having a complex double pole at 50kHz. This gave a rather strong rolloff in phase starting around 10kHz. By passively adding the HV output to the HV input we could extend the bandwidth of the PZT path. The passive path which doesn't have the phase rolloff dominates at high frequencies, extending the unity gain frequency we can get with this loop.

4.5 Sub-Carrier Servo

As mentioned above, we needed a way of shifting the frequency of the subcarrier beam in relation to the carrier by \mathcal{O} 100 kHz. We do this using AOMs by first shifting in one direction by 80 MHz, then shifting the opposite direction by 80 MHz + offset. The 80 MHz frequency source is a crystal oscillator. The variable frequency source is

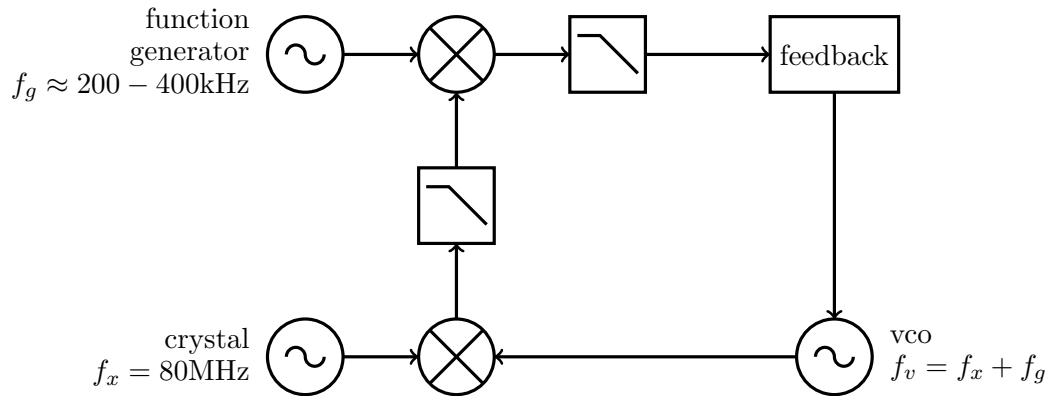


Figure 24: This diagram represents the electronic path of the subcarrier servo. This circuit locks the frequency of the vco to the frequency of the crystal oscillator plus an offset which is set by the function generator. This works by mixing the vco output and the crystal oscillator output together in a mixer (\times in the diagram). We take the output of the first mixer and filter it with a low pass filter to remove the high frequency output of the mixer so that we are left with a sine wave at a frequency which is $f_v - f_x$. This low frequency signal is then mixed with the signal from the function generator. This mixer output is then filtered with another low pass filter. The resulting error signal becomes the phase difference between the function generator signal and the vco, crystal difference signal, $f_v - f_x$. The feedback servo completes this modified phase locked loop.

a VCO which uses the output of a feedback servo to modulate the frequency. The sensor for this feedback is the demodulated beat signal of the output of the two AOM frequency sources. The demodulation is done by mixing the beat signal with the output of a function generator which is set to the desired offset frequency. See figure 24 for the layout of the electronics.

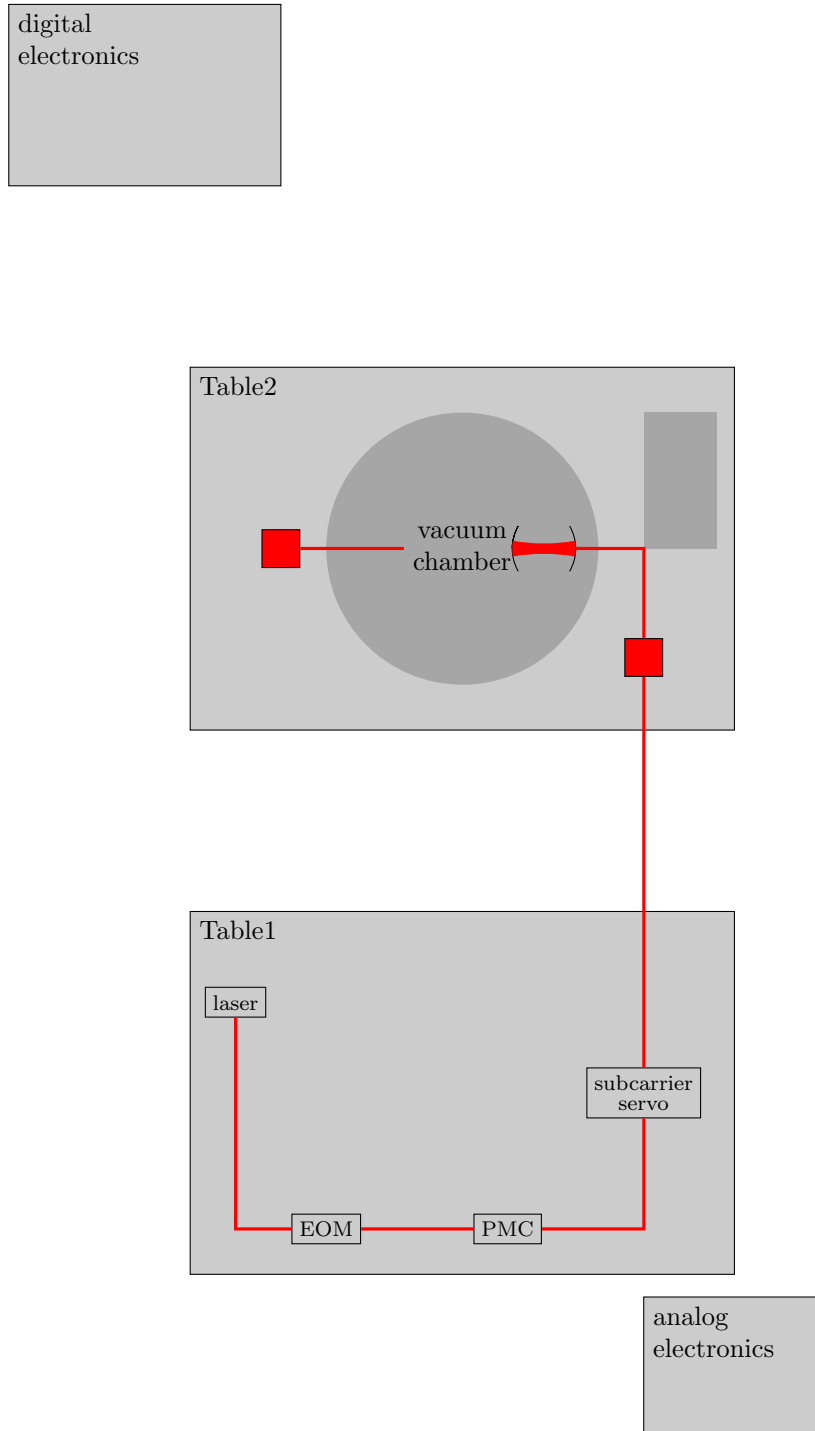


Figure 25: This depicts the basic layout of how the experiment is situated in the lab. The red boxes on table 2 are periscopes necessary for getting the laser to the height of the trap cavity, and on the output side for getting back to the table height for the output optics.

Chapter 5

Noise Sources

The goal of this thesis is to develop the control for the optical spring experiment, observe the signature of the optical spring in the transfer function, and determine the noise level and steps for noise mitigation in order to remove active feedback at the spring resonance.

In this chapter I will define the sources of noise which we have identified and describe their impact to the experiment.

We have identified sources of noise and projected their contribution to noise in the length of the cavity. We could also choose frequency of the light as a reference, but we choose the cavity length as this is the natural dimension when talking about a spring, $F = -kx$. This "noise budget" is necessary for building the full picture for explaining our observations.

The Pound Drever Hall (PDH) error signal for the trap cavity is our observation of the length of the cavity. With the cavity locked we use the PDH signal to infer residual motion of the cavity. We calibrate the error signal by measuring the open loop gain and dividing out the feedback servo and actuation function.

5.1 Seismic

Seismic noise in our lab was a bit problematic due to the fact there is a giant inflatable roof sports dome right next door. The fans required to keep the roof up create a great deal of seismic noise at specific frequencies.

This causes peaks in our seismic spectrum at frequencies that are integer multiples

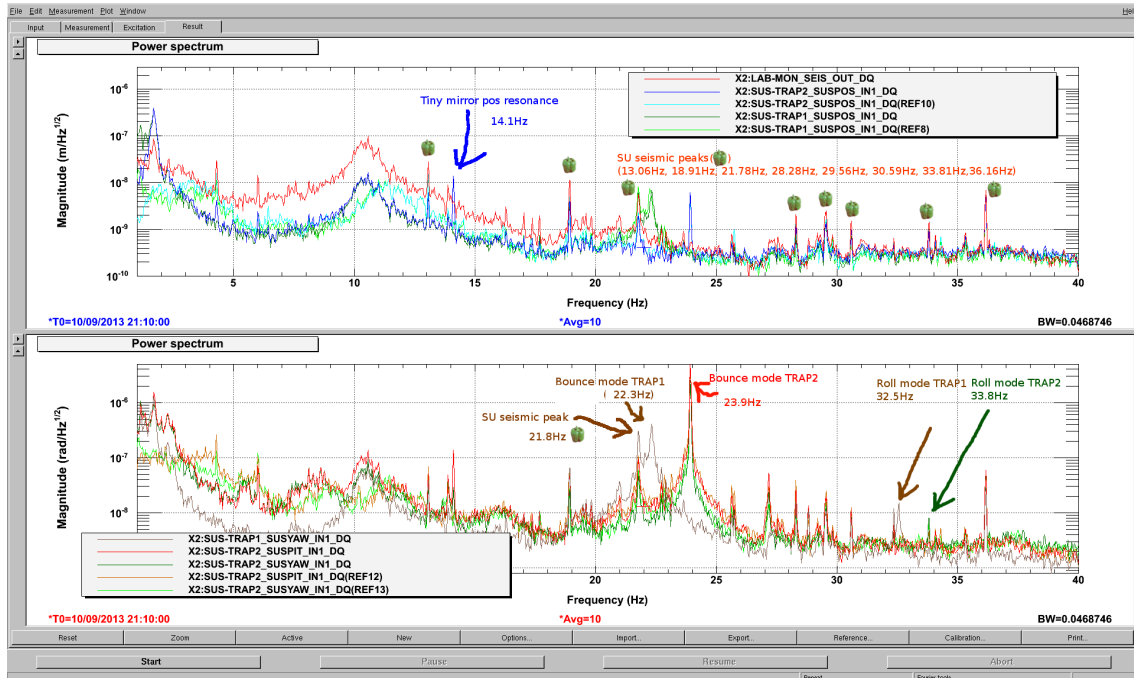


Figure 26: This shows the spectrum of the seismic noise in our lab taken with a seismometer located on table 2. The peppers represent peaks in the seismic background. This spectrum was taken with the first payload assembly suspended from our small optic suspension before installing blade springs for vertical isolation. We needed to move the bounce mode frequency down in order to not excite it with the background seismic peaks. The suspension upgrade took place concurrently with the payload upgrade discussed in section 4.2.1.

of each fans rotational frequency Ω_f . The frequency at $n_b\Omega_f$, where n_b is the number of blades in the fan, will likely be the highest since a section of air near the fan will feel an increase in force as each blade passes by. The seismic noise is plotting along with noise measured from the two suspensions in figure 26.

Aside from the seismic peaks, the background seismic spectrum was basically as expected. The falloff was $1/f^2$ with $\approx 10^{-10}\text{m}/\sqrt{\text{Hz}}$ at 100Hz. The total rms motion was less than $1\mu\text{m}$ at 100mHz. With a voltage range of $\pm 10\text{V}$ at the coil drivers for our suspensions we can get a position range of about $\pm 68\mu\text{m}$ for the suspended mass at DC. This gives us plenty of range to cover the background seismic motion.

5.2 Thermal

Thermal noise is the random aggregate fluctuations of an object due to the random motion of the constituent particles. The spectral density of this motion is dependant on the temperature and the dissipation of the material. The random motion in a dimension of interest also depends on the geometry of the system.

These motions are tiny and only really affect us in a cavity where we rely on the constructive interference of the micron wavelength light. So, we look closely at the materials in direct contact with the mirrors.

Specifically, we identify the payload suspension attachment to the small mirror, the aluminum disk within which the large mirror is imbedded, and the layers of the high reflective coatings.

Thermal noise will also affect us indirectly if we use another cavity for reference. The frequency stabilization servo (FSS) will not be able to suppress the frequency noise below the thermal noise from the mirrors of the reference cavity. This thermal noise is part of the sensing noise for the servo and thus gets imprinted on the laser frequency which will account for detuning noise of the cavity.

If we were to implement the FSS we would need to account for the reference cavity's thermal noise as well. We estimate these noise effects as well in order to quantify the possible improvements gained by the implementation of this system.

Thermal noise from the reference cavity consists of the same coating thermal for the trap cavity and thermal noise from the glue used to attach the mirrors on the ends of the fused silica spacer.

5.2.1 Derivation of Payload Suspension Thermal Noise

We derive the thermal noise of a system using the fluctuation-dissipation theorem which describes the relationship between the fluctuation of a system and its dissipation. The starting point for our thermal noise calculations is the Callen form of the theorem [14, 15].

This calculation requires us to know the dynamics of the system.

The power spectral density (PSD) of the thermal noise is defined,

$$S_{xx}(\omega) = \frac{4k_B T}{\omega^2} \Re(Y(\omega)) \quad (5.1)$$

$$= \frac{4k_B T}{\omega^2} \Re(Y(\omega)) \quad (5.2)$$

For a system with velocity damping(b), $F_{\text{ext}} = m\ddot{x} + b\dot{x} + kx$, we can rewrite the PSD as,

$$S_{xx}(\omega) = \frac{4k_B T}{\omega^2} \Re(Y(\omega)) \quad (5.3)$$

$$= \frac{4k_B T b / \omega^2}{b^2 + (m\omega - k/\omega)^2} \quad (5.4)$$

Notice that as the damping coefficient goes to zero, this function becomes a delta function at the resonant frequency, $\omega_0 = \sqrt{k/m}$.

That works for something like gas damping. However, we are more interested in the thermal noise due to internal damping where the damping is essentially absorbed into the spring coefficient making it complex. This changes the dependence of the PSD on ω . Taking this new form of damping, $F_{\text{ext}} = m\ddot{x} + k(1 + i\phi)x$, where ϕ is called the loss angle (for small values of ϕ) we can write the PSD as,

$$S_{xx}(\omega) = \frac{4k_B T k \phi / \omega}{(k\phi)^2 + (m\omega^2 - k)^2} \quad (5.5)$$

In this case we still have the peak at the resonant frequency, however the form of the noise is different above and below the resonant frequency.

Now we will derive the thermal noise for our small mirror assembly. We are concerned with thermal noise due to the epoxy used to glue the fibers to the mass. We start with the Lagrangian to get the dynamics of the system and compute the

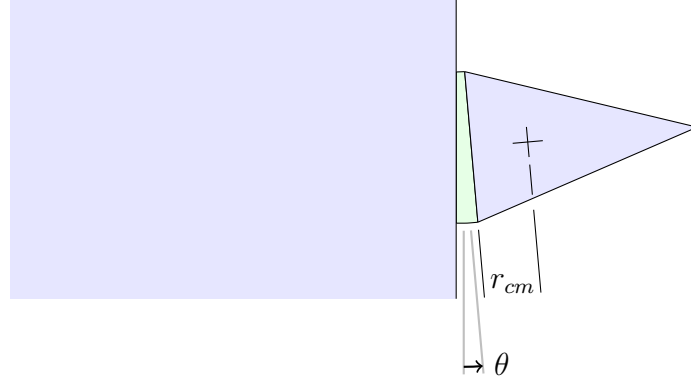


Figure 27: This shows the setup for the thermal noise derivations starting with equations 5.6. The fiber is not included in the calculation for this.

admittance.

$$\begin{aligned}
T &= \frac{1}{2}M\dot{x}^2 + \frac{1}{2}I_M (\dot{\eta}_1^2 + \dot{\eta}_2^2) \\
&\quad + \frac{1}{2}m \left(\dot{x} + r_M\dot{\eta}_1 + r_{cm}\dot{\theta}_1 \right)^2 \\
&\quad + \frac{1}{4}m \left(2\dot{x} - r_M \left(\dot{\eta}_1 + \sqrt{3}\dot{\eta}_2 \right) + 2r_{cm}\dot{\theta}_2 \right)^2 \\
&\quad + \frac{1}{4}m \left(2\dot{x} - r_M \left(\dot{\eta}_1 - \sqrt{3}\dot{\eta}_2 \right) + 2r_{cm}\dot{\theta}_3 \right)^2 \\
&\quad + \frac{1}{2}I_m \left[\left(\dot{\theta}_1 + \dot{\eta}_1 \right)^2 + \frac{1}{2} \left(2\dot{\theta}_2 - \dot{\eta}_1 - \sqrt{3}\dot{\eta}_2 \right)^2 + \frac{1}{2} \left(2\dot{\theta}_3 - \dot{\eta}_1 + \sqrt{3}\dot{\eta}_2 \right)^2 \right]
\end{aligned} \tag{5.6}$$

$$V = \frac{El_y l_x^3}{8t} (\theta_1^2 + \theta_2^2 + \theta_3^2) \tag{5.7}$$

Where x is the position of the mirror, η_1 and η_2 are the pitch and yaw of the mirror, and θ_i are the angles of each fiber attachment nub with respect to the mirror.

The equations of motion become quite complex, so we simplify the system by only looking at the contribution from the longitudinal mode. The effects of the pitch and yaw modes should not contribute at first order for a perfectly aligned system, so we can simplify (5.6) and (5.7) by setting $\dot{\eta}_1 = \dot{\eta}_2 = \dot{\eta}_3 = 0$ and $\theta_1 = \theta_2 = \theta_3 = \theta$. The equations then become

$$T = \frac{1}{2}M\dot{x}^2 + \frac{3}{2}m \left(\dot{x} + r_{cm}\dot{\theta} \right)^2 + \frac{3}{2}I\dot{\theta}^2 \tag{5.8}$$

$$V = \frac{El_y l_x^3}{8t} \theta^2 \tag{5.9}$$

making some substitutions,

$$m_t = M + 3m, \quad (5.10)$$

$$I_t = 3(mr_{\text{cm}}^2 + I), \quad (5.11)$$

$$K = \frac{El_y l_x^3}{4t}, \quad (5.12)$$

the Lagrangian becomes,

$$\frac{1}{2} \left(m_t \dot{x}^2 + 6mr_{\text{cm}} \dot{x} \dot{\theta} + I_t \dot{\theta}^2 - K\theta^2 \right). \quad (5.13)$$

We can then find the equations of motion with an external force in the x direction,

$$F_{\text{ext}} = \frac{d}{dt} \frac{\partial L}{\partial \dot{x}} - \frac{\partial L}{\partial x}. \quad (5.14)$$

The two equations of motion become,

$$F_{\text{ext}} = m_t \ddot{x} + 3mr_{\text{cm}} \ddot{\theta} \quad (5.15)$$

$$0 = 3mr_{\text{cm}} \ddot{x} + I_t \ddot{\theta} + K\theta. \quad (5.16)$$

We can then solve for the impedance in the frequency domain,

$$Z = \frac{F_{\text{ext}}}{i\omega x} = m_t i\omega + 3mr_{\text{cm}} i\omega \frac{\theta}{x}, \quad (5.17)$$

where, from the second equation,

$$\frac{\theta}{x} = \frac{3mr_{\text{cm}} \omega^2}{K - I_t \omega^2}. \quad (5.18)$$

We need the real part of the admittance, $Y = 1/Z$.

$$Y = \frac{iI_t \omega^2 - iK}{\omega m_t (K - I_t \omega^2) + (3mr_{\text{cm}})^2 \omega^3} \quad (5.19)$$

The real part of Y is then,

$$\frac{K_0 \phi \omega (3mr_{\text{cm}})^2}{(m_t K_0 + \omega^2 ((3mr_{\text{cm}})^2 - m_t I_t))^2 + (m_t K_0 \phi)^2} \quad (5.20)$$

And the thermal noise in the x direction is (we have taken ϕ to be small),

$$S_{xx}(\omega) = \frac{4k_B T}{\omega} \left[\frac{K_0 \phi (3mr_{\text{cm}})^2}{(m_t K_0 + \omega^2 ((3mr_{\text{cm}})^2 - m_t I_t))^2} \right] \quad (5.21)$$

When ω is below the resonant frequency,

$$S_{xx}(\omega) = \frac{4k_B T \phi (3mr_{\text{cm}})^2}{m_t^2 \omega K_0} \quad (5.22)$$

$$S_{xx}(\omega) = \frac{16k_B T \phi t (3mr_{\text{cm}})^2}{m_t^2 \omega E l_y l_x^3} \quad (5.23)$$

It is desirable to make the nubs much smaller than the mirror. So, we can simplify the equation to,

$$S_{xx}(\omega) = \frac{36k_B T \phi t l_y l_z^4 \rho^2}{M^2 \omega E l_x}. \quad (5.24)$$

Now, it is obvious that we want to make the nubs so that the center of mass is close to the mirror, the thickness of the glue is small, and the glue area is large in the dimension along the axis of the mirror.

For our situation we have actually arrived at a cone shaped nub which provides for a large base and a short r_{cm} . Going back to eq. (5.22) we make the approximations to get

$$S_{xx}(\omega) = \frac{4k_B T \phi (3mr_{\text{cm}})^2}{M^2 \omega K_0} \quad (5.25)$$

The mass of a cone is $\frac{1}{3}\pi R^2 l_z \rho$, r_{cm} is $\frac{1}{4}l_z$, and $K_0 = \frac{3\pi E R^4}{4t}$.

$$S_{xx}(\omega) = \frac{k_B T \phi \pi t l_z^4 \rho^2}{3M^2 \omega E} \quad (5.26)$$

The noise is independent of the radius of the base of the cone, but depends heavily on the length of the cone. The expressions for K_0 assume that t is large compared to $\frac{R^2}{2R_m}$. Figure 28 depicts the amplitude spectral density (ASD) of this epoxy thermal noise contribution to the cavity length noise.

5.2.2 Other Thermal Noise Sources

As mentioned above, we have several sources of thermal noise to consider. The sources fall into two basic categories: elastic deformation of an object and bending at a glue joint.

I have presented the derivation of thermal noise from the glue joints attached to the payload mirror. The glue joints for the reference cavity mirrors are done in a similar way, however the geometry is much simpler. The equations of motion used

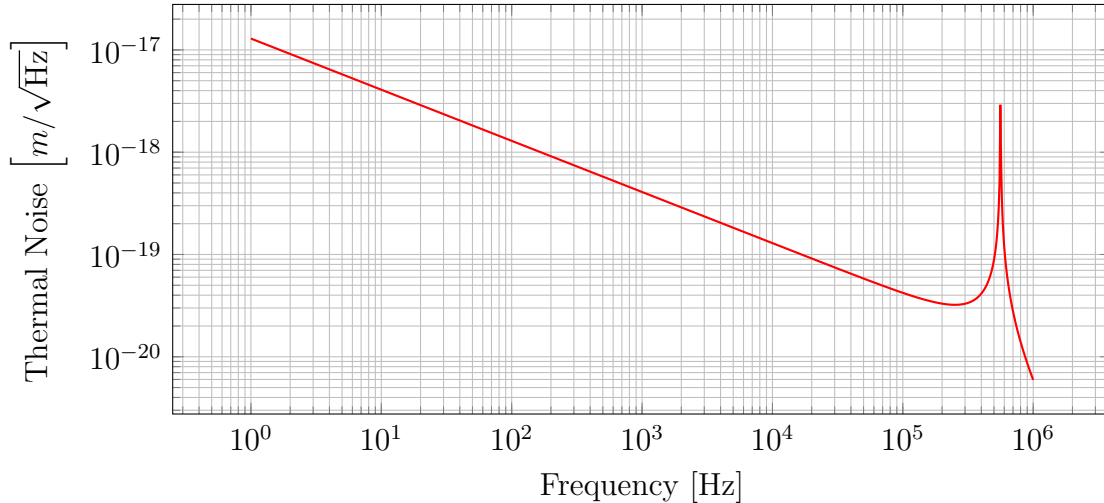


Figure 28: This is a plot of the thermal noise from the epoxy used to glue the small conical nubs for the fiber suspension. This includes the resonance which comes from the full expression in (5.21).

Parameter	Symbol	Value
Young's Modulus	E_0	3.378 GPa
Density	ρ	1118 kg/m ³
Loss Angle	ϕ	0.03

Table 2: parameters of the OptoCast 3553 epoxy resin. All parameters were taken from the data sheet except for the loss angle. The loss angle ϕ has not been measured for this material, so a fairly conservative value was assumed.

were simply from the longitudinal compression of the glue which attaches the mirror to the spacer.

The reference cavity was glued using 4 spots of the Optocast 3553 per mirror. The mirrors are one inch in diameter with a radius of curvature of $0.5m$ mounted to a spacer which has a 0.5 inch hole drilled through the middle. Centering the mirror over the 0.5 inch hole, there is at most a distance of $120\mu\text{m}$ from the curved surface of the mirror to the flat end of the spacer. I have used a value of $50\mu\text{m}$ for the thickness of the glue spots.

Parameters for glue used in thermal noise modelling are provided in table 2.

The other category of thermal noise source that I mentioned comes from the elastic deformation of an object. The method chosen for this calculation comes from Levin [16]. This method is derived from the same form of the fluctuation dissipation theorem as above, except that now, we compute the non-homogeneous deformation of an object where the deformation has a gaussian profile of the same diameter as the beam spot.

In the case of the coating thermal noise we use a direct application of the method presented by Levin.

There is one additional source which I place in the same non-homogeneous deformation category. That is the deformation of the aluminum disk which the large mirror is attached to. The mirror was attached by thermally expanding the aluminum and allowing it to cool around the large mirror. This gives a pretty solid attachment and we expect that the dominant thermal noise from this mount will come from the non-homogeneous deformation of the aluminum itself. For this calculation we simply apply the same calculation as we do for the coating to the aluminum disk with a "beam spot" diameter equal to the diameter of the large mirror. This will be correct up to some small geometric correction.

These additional noise sources are presented in figure 29. The total thermal noise contribution is quite low. With the fiber suspension design, the dominant thermal noise source is actually from the coatings.

5.3 Laser Frequency

Laser frequency noise couples into the measurement significantly due to the interferometric nature of the experiment. The coupling goes as the length of the cavity as discussed in section 4.1.

We can measure the frequency noise of the laser by referencing the beam to another cavity. The FSS described in section 3.3 can be used for this measurement because at low frequencies (below unity gain) the control signal is the noise entering the control loop. If the control loop is designed well, the dominant noise source will be the frequency noise which is inherent to the laser without the presence of the control loop. Figure 30 shows this laser frequency noise measurement converted from the Volts measured in the PZT path to Hz laser frequency.

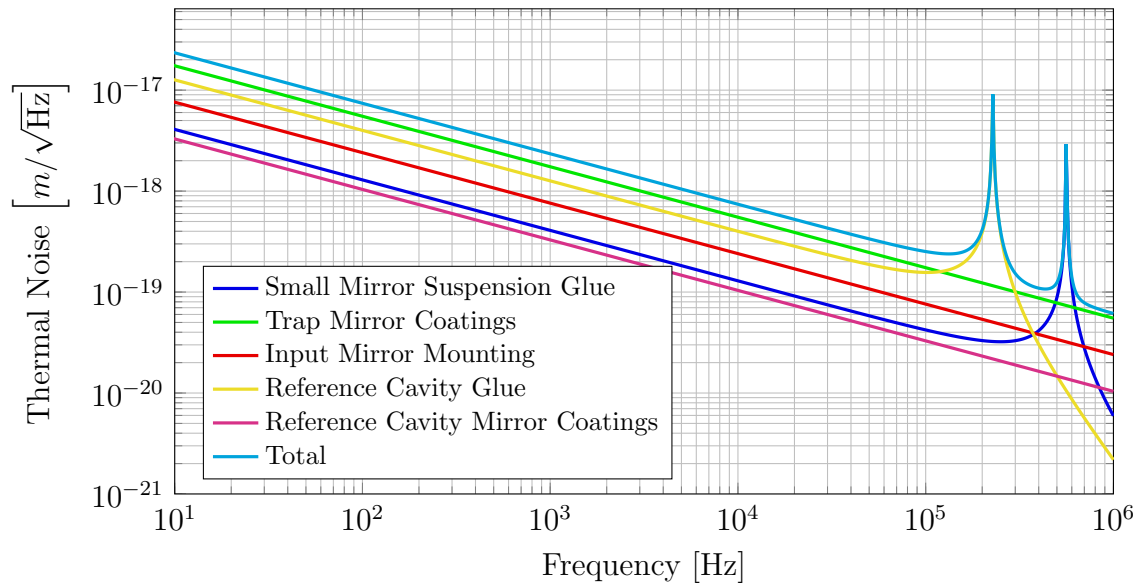


Figure 29: thermal noise contributions to experiment. The limiting thermal noise factors are from the coatings which are difficult to improve on. However, the total thermal noise is quite low.

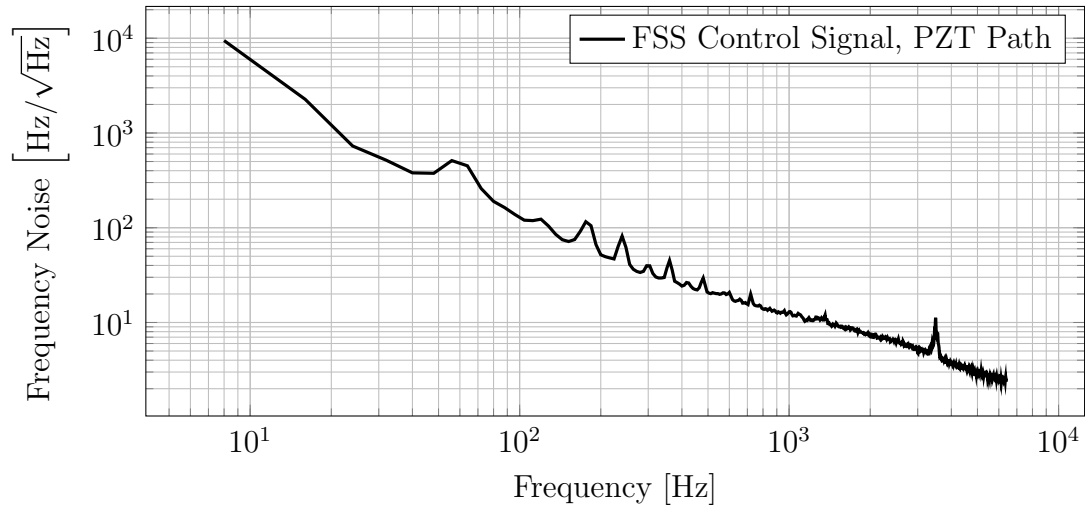


Figure 30: measured laser frequency noise from the PZT path of the FSS. This measurement was taken with the FSS locked with a unity gain frequency above 100kHz. We measured the control signal which gives us the free running laser frequency noise. The $1/f$ shape and $10\text{Hz}/\sqrt{\text{Hz}}$ at 1kHz are characteristics of the NPRO laser.

The laser frequency noise is the dominant noise source above a few hundred Hz. The level of noise is low enough to be able to control the cavity. With frequency stabilization we would theoretically get at least a factor of 100 improvement of the frequency noise at 1kHz. This is based on a unity gain frequency of 10kHz for the FSS loop, which should be able to be improved even more. We can only estimate the improvement in frequency noise because without another cavity which would give us an out of loop frequency measurement, we only have an in loop measurement of the frequency noise. The actual laser frequency noise will be composed of the in loop measured noise plus any additional sensing noise. The sensing noise can be electronic noise, shot noise, or noise in the effective length of the cavity.

5.4 Laser Intensity

As mentioned in chapter 3 the laser has an intensity noise specification of relative intensity noise (RIN) -150 dB/Hz. This is equivalent to a noise spectrum of $10^{-7.5} \text{W}/\sqrt{\text{Hz}}$ for a 1W beam. The specification is really only for frequencies above 100kHz or so which we aren't interested in. So, we have measured the intensity noise in the lab. The measured intensity noise compared to the shot noise limit is shown in figure 31.

We were not able to improve the intensity noise down to the shot noise limit. There was some residual sensing noise we couldn't correct, but we are able to get at least a factor of 3 improvement in the intensity noise below about 200Hz where the intensity noise dominates the noise budget.

5.5 Total Noise Budget

In figure 32 I show the total thermal noise with the laser noises and the quantum noise limit. From here it is clear there is a lot of room for improving the laser noise. In the range of our experiment of several hundred Hz, we can improve by more than an order of magnitude before improvements to seismic isolation are needed. Laser noise is more than 3 orders of magnitude above the thermal and quantum noises.

We have the actuation range that we need. Details of the actuation ranges were covered in section 4.4.2. The PZT range is about $\pm 160 \text{MHz}$. Converting this to

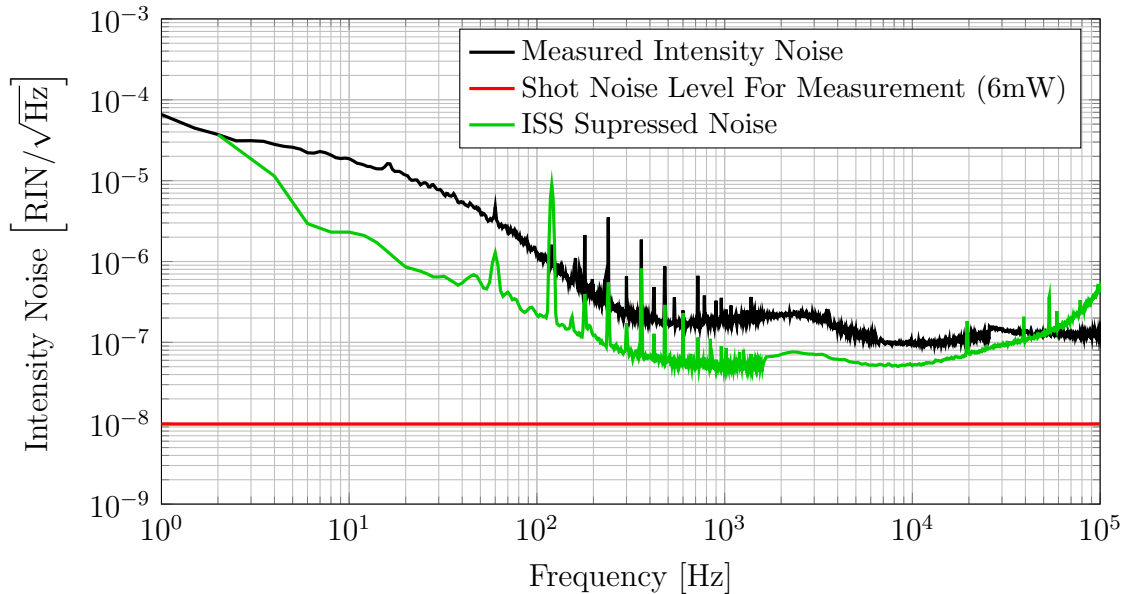


Figure 31: This is a comparison of intensity noise levels. The noise was measured in the lab using a PD which we built for use in our ISS. I have included for reference, the shot noise level for the amount of incident power in this measurement.

cavity length, the range is about 4×10^{-8} m This easily covers the range needed for the noise above 100Hz depicted in figure 32.

The OSEM range with our current driver electronics is about $\pm 2 \times 10^{-7}$ m/ $\sqrt{\text{Hz}}$ at 18Hz (at the suspension resonance frequency). The actuation range is flat in force up to a few hundred Hz where the coil inductance starts to matter so in terms of position the range has a slope of f^{-2} above the 1Hz pendulum frequency of the input mirror. The OSEM actuation range is also well above what is plotted in figure 32 however, because the Q of the payload suspension is so high, the actual height of the 18Hz isn't resolved. We needed to actively damp the 18Hz peak for locking the cavity. This was done with optical levers and using a resonant gain filter to damp with pitch and yaw actuation on the intermediate mass. With this motion damped we have plenty of range as seen in the measured trap length noise.

The amount of additional noise reduction needed to turn off the loops depends on the amount of optical spring damping we can achieve. The optical spring resonance will amplify the noise nearby as well so the proximity of peaks in the background can affect the total rms noise as well. We will explore this more in the next chapter, but

staying clear of strong resonances and with the amount of damping we will be able to achieve, we will be just at the limit of the stability range. With the implementation of the full pre-stabilized laser (PSL) with the performance that it currently has we should have low enough noise to turn off active feedback above 10Hz.

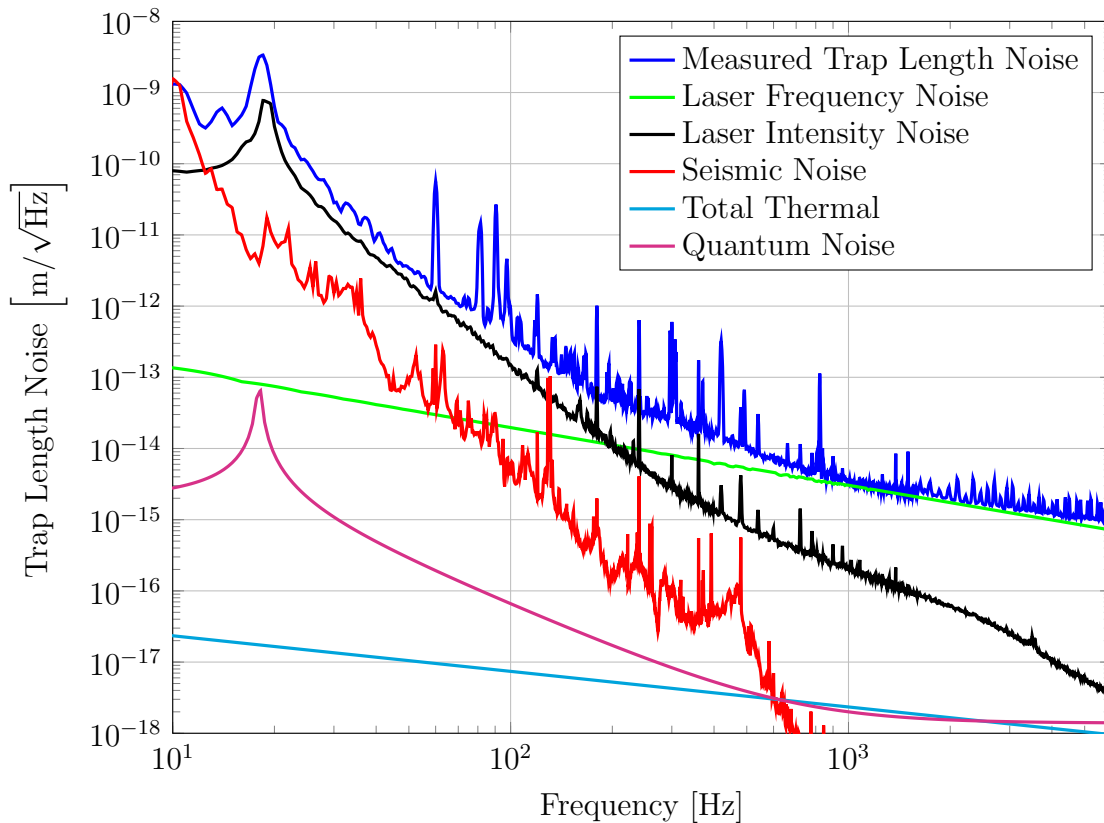


Figure 32: total noise budget including measured noise. The measured trap length noise is the measurement presented in the results section. The quantum noise limit shown was computed using the parameters of the optical spring during trap length noise measurement. The experiment will take place with an optical spring frequency between a few hundred Hz to about 1kHz. The noise above a few hundred Hz is within a stability range of $\mathcal{O}10\text{pm}$. However, the optical spring resonance will amplify the motion by an amount dependant on the optical spring damping. Here, in order to remove active feedback we will need either a very well damped optical spring or we will need to reduce the noise amplified by the resonance. The dominant noise which we have identified by far is from the laser frequency noise and laser intensity noise. The intensity noise can be improved by at least a factor of 3 with the implementation of the ISS. The frequency noise should be able to be improved down to a level of about $4 \times 10^{-7}\text{Hz}/\sqrt{\text{Hz}}$ with the FSS.

Chapter 6

Results

In order to observe the optical spring effect we have set up the experiment as described in chapter 4. The measurement that we take is the open loop transfer function of the servo. This is accomplished at the electronic servo board itself as shown in figure 33.

6.1 Stability

The definition of a stable system is one which has a bounded output for a bounded input. In our case we are interested in the closed-loop system consisting of an optical spring attached to the small mass.

This system is linear and time-invariant (LTI). As such it will multiply a sinusoidal input of a specific frequency with a complex number which is only dependant on this frequency and will not change over time. These values are called transfer function and fully describe the system.

The criterion for stability above translates into the requirement that all poles of the transfer function lie in the upper half of the complex plane, that is none of its eigenmodes are exponentially growing.

To convert this statement into a experimentally measurable criterion I first look at the energy budget of the system. As a reminder, a single optical spring has a delayed response in the cavity which causes it to be unstable.

One way to visualize this is that we have a system that, without the delay, the force is maximum when the length is minimum. In this case as the cavity shortens, a force is applied in the opposite direction. As the cavity lengthens, a force is applied

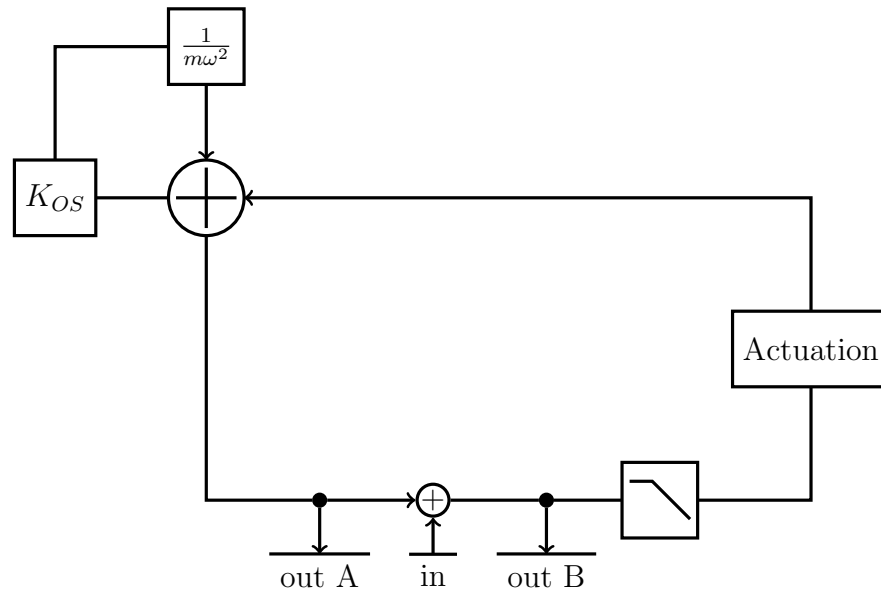


Figure 33: This is a simplified schematic showing how we measure the optical spring. While the loop is closed, we can inject a sine wave of a specific frequency at "in", then measure the amplitude and phase shift of this sine wave at the points, outA and outB, giving us the complex numbers A and B . The open loop gain at each point is then given by A/B . The transfer function is then constructed out of many of these measurements at different frequencies. A Bode plot can then be made which is a plot of gain versus frequency. The plot is actually two plots: one for the magnitude of the gain and one for the phase of the gain. The transfer function we are measuring here is the open loop gain of the sensing, feedback, and actuation gain H (the lower right loop) times the closed loop gain of the optical spring, $G = \frac{H}{1 - K_{OS}/m\omega^2}$.

in the same direction as the motion. And the total work done over each cycle is zero, $\oint F dx = 0$. With a positive delay, the force applied while the cavity is lengthening is greater than when it is shortening which makes the total work per cycle greater than zero. We're adding energy to the system, making it unstable.

We can aid the visualization with the following thought experiment. We attach a device that requires the mirror to follow a sinusoidal motion at a specific amplitude and frequency regardless of external forces and place it in a cavity to form an optical spring where the absolute value of the spring constant is $m\omega_0^2$ where m is the mass of the optic¹ and ω_0 is the angular frequency the device is following. Work would be done on the optic by the spring and taken up by the special device. Of course there's no magic here, the energy comes from the power delivered by the laser. Without the device to take up the energy the spring is delivering to the optic, the energy must go into the motion of the optic where the total energy is related to the motion by,

$$E = \frac{1}{2} k x_0^2, \quad (6.1)$$

where k is the spring constant and x_0 is the amplitude of the motion. A delay manifests itself in the transfer function as a phase lag. To further work out how the transfer function phase is related to stability we can solve the equations of motion,

$$\begin{aligned} F &= ma = -kx \\ m\ddot{x} &= -kx. \end{aligned}$$

The solution to this is harmonic motion of the form,

$$x = Ae^{i\sqrt{k/mt}} + Be^{-i\sqrt{k/mt}}.$$

I will take B to be 0. This sets the initial condition, which in the end can be free again by multiplying by a phase factor $e^{i\theta}$. Motion in the real world is real, so we always take the real part of the complex motion when we're done. The imaginary part is just a mathematical construct that helps with the calculations.

We can damp the system in way similar to what was discussed in section 2.1. I will leave out the velocity term from equation 2.1 and instead use a complex k for the damping. This is the same thing as having a viscosity coefficient b with a f^{-1}

¹The imaginary device is massless of course.

frequency dependence. Allowing k to be a complex number, $k = k_0 e^{i\phi}$, we can see readily that this corresponds to a transfer function $-k$ which shifts the wave in time.

$$\begin{aligned} F &= -kx \\ &= -k_0 A e^{i\omega t + i\phi} . \end{aligned} \quad (6.2)$$

And the energy is,

$$\begin{aligned} E &= \oint F dx \\ &= \oint F v dt \\ &= \oint \Re(-k_0 A e^{i\omega t} e^{i\phi}) \Re(i\omega A e^{i\omega t}) dt \\ &= \frac{-k_0 A^2}{2} \oint \Im(e^{i\phi}) \omega dt \\ &= \frac{-k_0 A^2}{2} \sin(\phi) . \end{aligned} \quad (6.3)$$

We can see that with a small positive ϕ we have a spring that is taking energy from the motion of the mass. A small negative ϕ puts energy into the motion of the mass making it unstable.

We will be observing the optical spring effect through a transfer function, so we need to understand how the stability affects the transfer function measurement. Starting with the closed loop gain of a spring we look at the phase behavior around the resonance,

$$\begin{aligned} \text{CLG} &= \frac{1}{1 - \frac{k_0(1+i\phi)}{m\omega^2}} \\ &= \frac{m\omega^2}{m\omega^2 - k_0(1+i\phi)} \\ &= \frac{m^2\omega^4 - k_0 m\omega^2 + ik_0\phi m\omega^2}{(m\omega^2 - k_0)^2 + k_0^2\phi^2} \end{aligned} \quad (6.4)$$

$$\begin{aligned} \angle \text{CLG} &= \arctan \frac{k_0\phi}{m\omega^2 - k_0} \\ \frac{d}{d\omega} (\angle \text{CLG}) &= \frac{-2k_0\phi m\omega}{(m\omega^2 + k_0)^2 + k_0^2\phi^2} . \end{aligned} \quad (6.5)$$

On resonance the slope of the phase becomes,

$$\frac{-2m\omega_0}{k_0\phi} . \quad (6.6)$$

Now, we can see clearly that the slope of the phase on resonance is negative for positive ϕ . Also, note that the slope gets steeper for a smaller magnitude of ϕ .

Therefore, for the case of the stable spring $\phi > 0$, we see that the phase of the transfer function must decrease as the frequency increases through the resonance. For the unstable spring $\phi < 0$ the phase will increase over the resonance. This can be seen in figure 36 and is experimentally accessible in a closed loop measurement of the spring.

Now, in our case, the measurement isn't the pure closed loop gain of the optical spring. We are actually measuring this closed loop gain times the open loop gain of the feedback loop. The result is that the characteristic shape of the falling phase over the resonance is preserved. This can be seen by writing the complex gains with exponential functions to generate the imaginary parts,

$$\begin{aligned} FG &= F_0 e^{i\theta_1} G_0 e^{i\theta_2} \\ &= F_0 G_0 e^{i(\theta_1 + \theta_2)}, \end{aligned} \tag{6.7}$$

where G is the closed loop transfer function for the optical spring and F is the transfer function for the rest of the feedback system. Knowing θ_1 we can subtract it from the measured phase. I will actually present the results as they were measured and compare with the theoretical plot of the transfer function including both the optical spring closed loop transfer function and the feedback transfer function.

The transfer function will also be affected by the suspension. At high frequencies however, where the optical spring is, the suspension has negligible effect. With the suspension frequency at 18Hz and the optical spring frequency at 360Hz the magnitude of the optical spring constant is 400 times larger than that of the suspension. This gives a factor of 400 dilution in the ϕ value from the suspension to that of the observed optical spring. With a measured ϕ of about 2×10^{-6} for the suspension, the contribution to the damping loss angle of the optical spring is about 5×10^{-9} . This is negligible compared to the optical spring damping range we can achieve of, $\phi = \pm \mathcal{O}10^{-3}$.

6.1.1 Stability Range

We know how to make a stable spring but any spring becomes nonlinear at some range of motion. For us to be able to remove the active feedback to the system, we need to

understand what this range is so we can stay within its limits. We can first define a region of stability where the phase of the spring is positive. An example parameter space is shown in figure 35. On the y-axis of this plot you see the subcarrier detuning. This is the overall detuning of the cavity in frequency, which directly corresponds to a cavity length by,

$$\frac{\Delta L}{L} = \frac{\Delta f}{f} , \quad (6.8)$$

Where L is the length of the cavity and f is the frequency of the laser. The x-axis changes the nature of the double optical field that we're sending into the cavity. It is completely independent of the cavity length change.

We want the mirror to stay within the limits of positive phase, which is within the zero phase line on the plot. If we pick a spot along the x-axis and vary the subcarrier offset (or mirror position) we see that the frequency of the spring increases quite a bit from the center of the stable range. Additionally, the phase of the spring decreases to zero. To give a margin, we will want the range of motion to really stay within about a tenth of the overall stable boundary. Looking at the blue star in this plot, we can see that the frequency and phase of the spring don't change dramatically within about 10kHz of subcarrier detuning compared to the ≈ 100 kHz stable region. By equation (6.8) we get a length displacement of,

$$\begin{aligned} \Delta L &= \frac{10\text{kHz}}{2.8 \times 10^{11}\text{kHz}} 0.07\text{m} \\ &= 2.5\text{pm} . \end{aligned} \quad (6.9)$$

Because the spring frequency actually increases toward the boundary, more force is required to get the spring into the unstable region than what one would compute from the central k value with $F = -kx$. We would actually need a force of $m\omega^2x$ to get into the region of instability, where ω is the spring angular frequency at the boundary. For example, in the case of the blue star from the plot, the lower spring frequency at the boundary is $f_{\text{limit}} = 800\text{Hz}$. The force required to exceed this boundary will be then given by,

$$\begin{aligned} F &= 4\pi^2 m f_{\text{limit}}^2 x \\ &= 4\pi^2 \times 0.0005\text{kg} \times (800\text{Hz})^2 \times 10\text{pm} \\ &= 1.26 \times 10^{-7}\text{N} . \end{aligned}$$

This is all good for the adiabatic case where the motion is less than the spring resonance. The resonantly enhanced motion at the spring resonance, however, is strongly dependant on the phase of the spring. The damped spring removes energy entering the system at a rate determined by the phase. Since we are not always at the equilibrium point, the average phase and therefore the average amount of energy dissipated is less than at the equilibrium point, effectively increasing the Q of the spring.

Since we have a high Q optical spring most of the root mean squared (rms) motion of the mass will come from the amplification at the resonance until we include very low frequency motion. As we go lower in frequency the optical spring filters out more of the motion as seen in figure 36. This decreases as f^2 until we get to the suspension resonance, which is not shown in the plot. At frequencies below this point, the optical spring response flattens out and no longer depends on the frequency. Our suspension resonance is at about 18Hz and below this point, the amount of displacement noise due to seismic starts to become the dominant noise source. At low enough frequencies, if the optical spring is not strong enough, the seismic motion will dominate the total rms motion. The closed loop suppression at frequencies below the suspension resonance can be found easily since we know the transfer function is 1 at very high frequencies and f^2 between the the suspension resonance and the optical resonance. The suppression below the suspension frequency is then,

$$(f_{\text{sus}}/f_{\text{OS}})^2 , \quad (6.10)$$

which with an optical spring frequency of 720 Hz we have seismic suppression of,

$$\begin{aligned} & \left(\frac{1}{40} \right)^2 \\ &= \frac{1}{1600} \\ &\approx 6 \times 10^{-4} . \end{aligned}$$

At very low frequencies, where the rms motion will increase again, we are in the adiabatic condition and have the advantage of the steep energy boundaries of the spring. An example of two different spring configurations can be seen in figure 34.

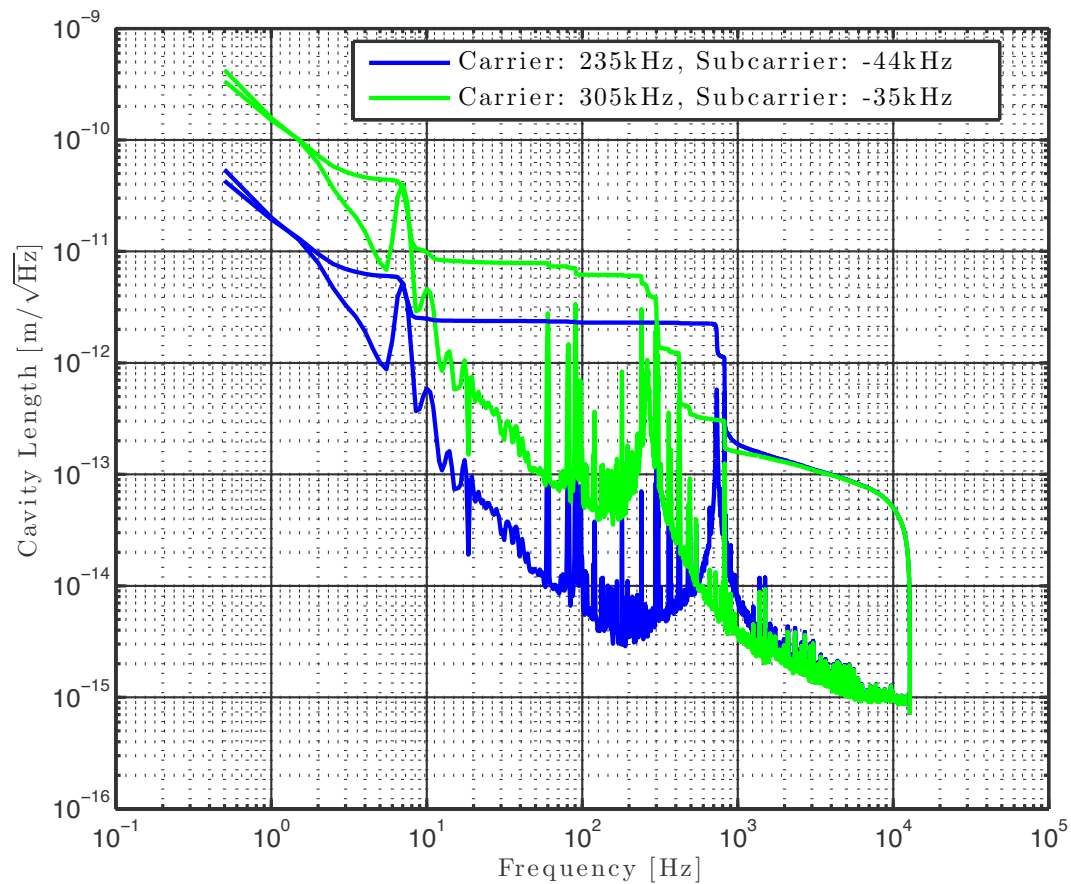


Figure 34: RMS motion after applying optical spring. The carrier and subcarrier input powers are fixed for both examples. The subcarrier detuning was chosen to maximize the damping for each carrier detuning. This plot uses the noise measurement from section includes the coefficient of thermal expansion term that is discussed in section 6.4.2.

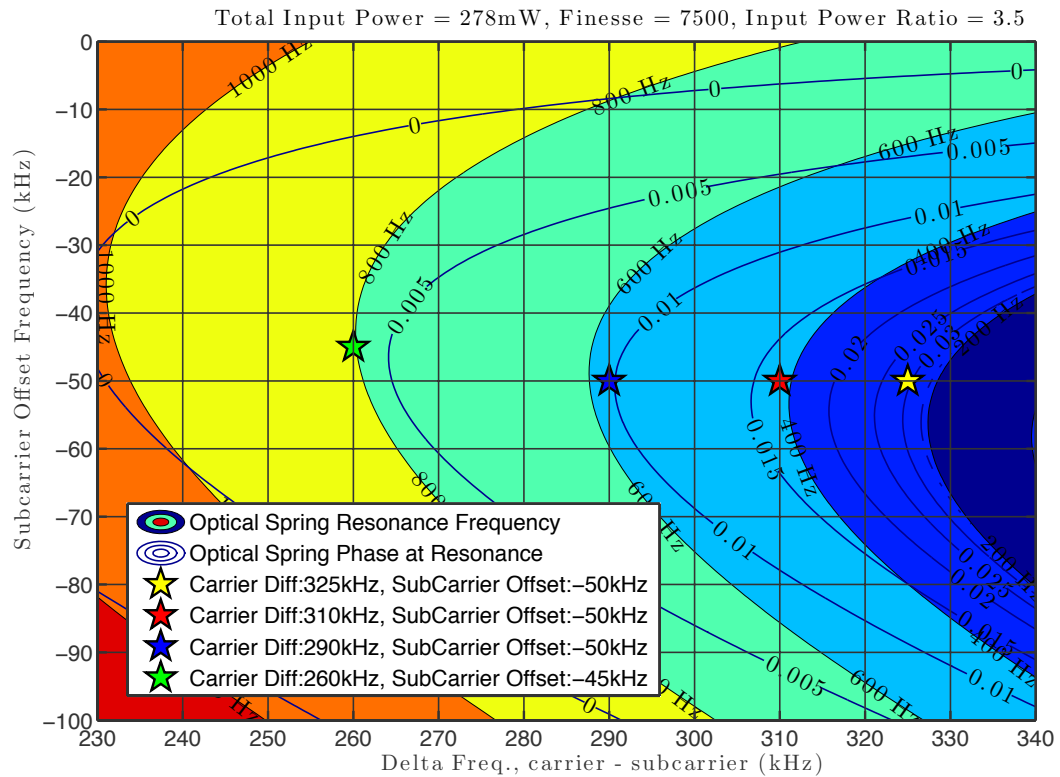


Figure 35: The parameter space of the experiment. We can see the stability values for different detunings given by the phase contours which are in units of radians. Ideally we want a high frequency and phase.

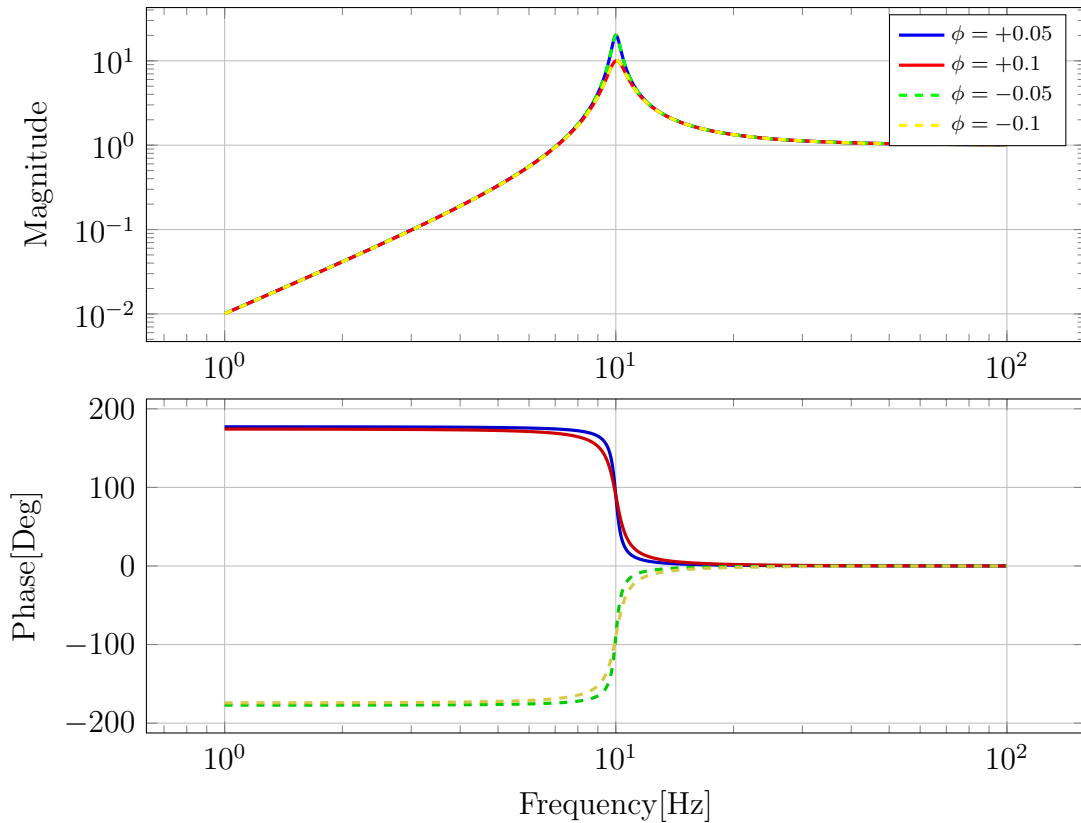


Figure 36: Damped spring closed loop gain behavior. The two solid lines are examples of stable springs ($\phi > 0$). The two dashed lines are unstable springs. The signature we look for to verify stability of the optical spring is the direction the phase goes from 180 to 0 degrees. Decreasing phase over the resonant frequency indicates a stable spring, while the unstable spring has the opposite behavior. Notice that the stability cannot be determined from the magnitude plot. Positive and negative ϕ look exactly the same. Loss angle ϕ is presented in radians.

Parameter	Value	Units
Cavity Length	7	cm
Carrier Power	440	mW
Subcarrier Power	44	mW
Subcarrier Servo Offset	355	kHz
PDH Local Oscillator	35	MHz
Specified EOM Modulation Depth	> 0.2	rad/V

Table 3: Parameters for the first edition of the linear trap experiment.

6.2 Linear Trap Experiment, 1st Edition

In the first set of measurements, the carrier to subcarrier power ratio was set to 10. I fixed the subcarrier to carrier offset frequency to 355kHz. This offset frequency was chosen because it gave a comfortable margin in stability. The trap would consistently lose lock with an offset of around 250kHz. A list of parameters is provided in table 3.

The experiment was performed by keeping the power constant for each beam, leaving the carrier frequency offset by 355kHz above the subcarrier frequency, and varying the subcarrier detuning. With this, when the subcarrier is detuned above the resonant frequency of the cavity, both beams are detuned in the same direction and the resulting combined spring must be unstable. We expect that as we detune the subcarrier from positive to negative the contribution to the spring constant from the subcarrier will decrease which in turn reduces the resonant frequency. Because of the power ratio, cavity finesse, and subcarrier servo offset frequency we expect to see stable springs at some point after detuning the subcarrier beam to the opposite side of the resonant frequency of the cavity.

During the optical spring measurements we were sensitive to variations in power. I observed that the stable optical spring frequency could drift over a few hours by as much as 100Hz without me changing any of the parameters of the setup. This is shown in table 4.

After the data was taken of the stable spring with fixed parameters and before losing lock on the feedback loop, I took several measurements in a row in a shorter period of time of about 30 minutes total. The results from these measurements are

Measurement ID	Error point offset [mV]	Resonant Frequency [Hz]	Time of Measurement [Min]
1-30	-604	742	0
1-31	-873	757	4
1-33	-1120	782	9
1-34	-1410	834	12
1-35	-827	768	17
1-36	-827	789	52
1-37	-827	870	91
1-38	-827	820	102
1-39	-522	800	107
1-40	-172	797	112
1-41	28	801	117
1-42	137	806	120
1-43	438	818	125
1-44	879	840	130

Table 4: This table contains the error point offset measured for each spring measurement during the second lock stretch of experiment 1. The frequencies indicated were measured from the data by finding the frequency corresponding to the ± 90 degree phase point of the closed loop optical spring. Measurements 35-38 were taken at the same error point offset and had a wide range in resonant frequencies compared to the rest of the data. Measurement ID 1-32 is not included in this table because the data was saved twice. The data is identical to 1-33.

provided in figures 37, and 38.

One of the reasons for this is the fact that the carrier beam was not well aligned to the subcarrier beam causing drifts in the power ratio between carrier and subcarrier as the overall alignment drifted. Another complication in the first run was due to the fact that the carrier and subcarrier beams had exactly the same polarizations which caused a strong beat signal at 355kHz. This beat signal was low enough in frequency that it would show strongly in the resonant radio frequency photodiode (RFPD) output, likely causing saturation effects in the electronics that would lead to an unpredictable subcarrier detuning. The effect of carrier and subcarrier beating will be discussed further in section 6.3

Changing the detuning of the subcarrier during the measurement also changes the overall gain of the feedback system. This is because of the fact that the Pound Drever Hall (PDH) error signal does not have a linear relationship with detuning as seen in figure 12. During each measurement, we keep the error point fixed to a small region, which keeps the system quite linear. But as we change the error point offset the slope of the signal changes. This slope corresponds to an overall gain factor in the system. We can actually see the effect in the measurements of figure 39.

Despite these issues we were clearly able to observe stable and unstable optical springs and there was a short stretch of measurements that were able to be fit to the theoretical model. However, to get the actual frequency detuning and power level under better control, a few design changes were needed which I will discuss in the next section.

6.3 Experimental Layout Revision

From our first layout design there was a rather large beat signal on the RFPD used for generating the PDH signal for our locking feedback servo. This beat signal is a result of our initial layout involving the combining of carrier and subcarrier beams before a faraday isolator (FI) which resulted in the two beams having the same polarization. This produces a beat signal of the difference in the two frequencies. The power inside the cavity has the beat between the carrier beam and the unmodulated part of the subcarrier beam. This shows up in the transmitted DC photo-diode (PD) because the bandwidth is much greater than the subcarrier servo offset frequency. The Thorlabs

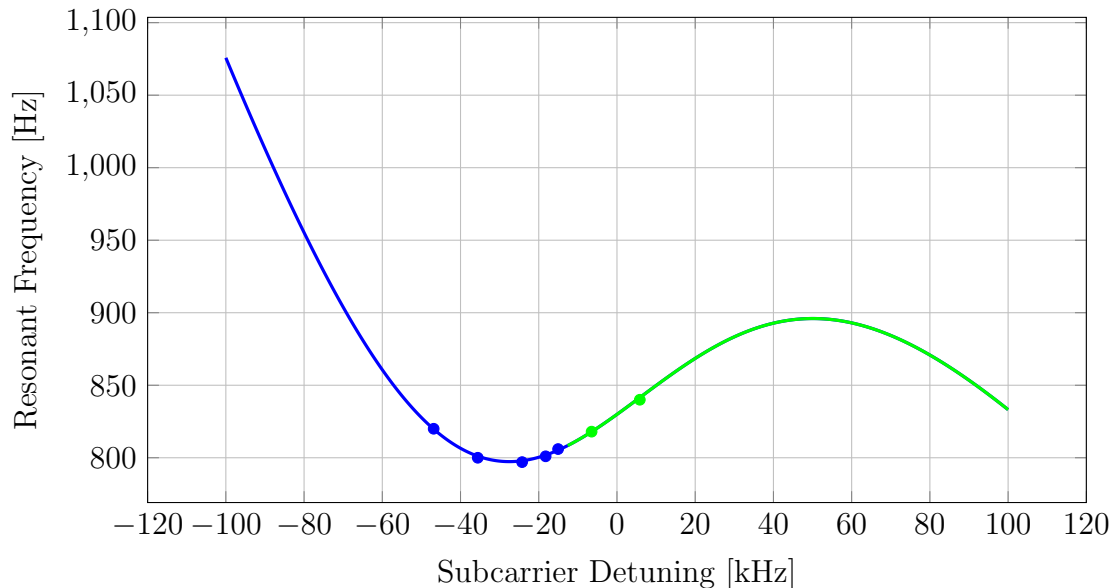


Figure 37: The solid lines show the theoretical spring frequencies for all of the measurements that took place in a span of about 30 minutes during the first edition at the end of one lock stretch. The dots correspond to the actual measurements of the optical spring at different subcarrier detunings. The entire space depicted is in the region of static stability, i.e. the optical spring provides a restoring force. The colors correspond to the dynamic stability of the optical spring. Blue is dynamically stable. Green is dynamically unstable. The carrier frequency remained at a fixed offset from the subcarrier at 355 kHz. The fitting for this plot was done by plotting the actual measured resonant frequency vs. the error point offset in mV. The theoretical curve was transformed to match the axes using the PDH transformation shown in figure 12. I could then fit the curve using four parameters: finesse, total power, error point voltage offset, and carrier to subcarrier power ratio. The parameters used in this plot are: $\mathcal{F} = 8000$, power ratio= 1.5, total power= 344.7mW, error point offset= $-670\text{mV} = -19.07\text{kHz}$. This does not include any effect due to the thermal expansion of the optics mentioned in section 6.4.2.

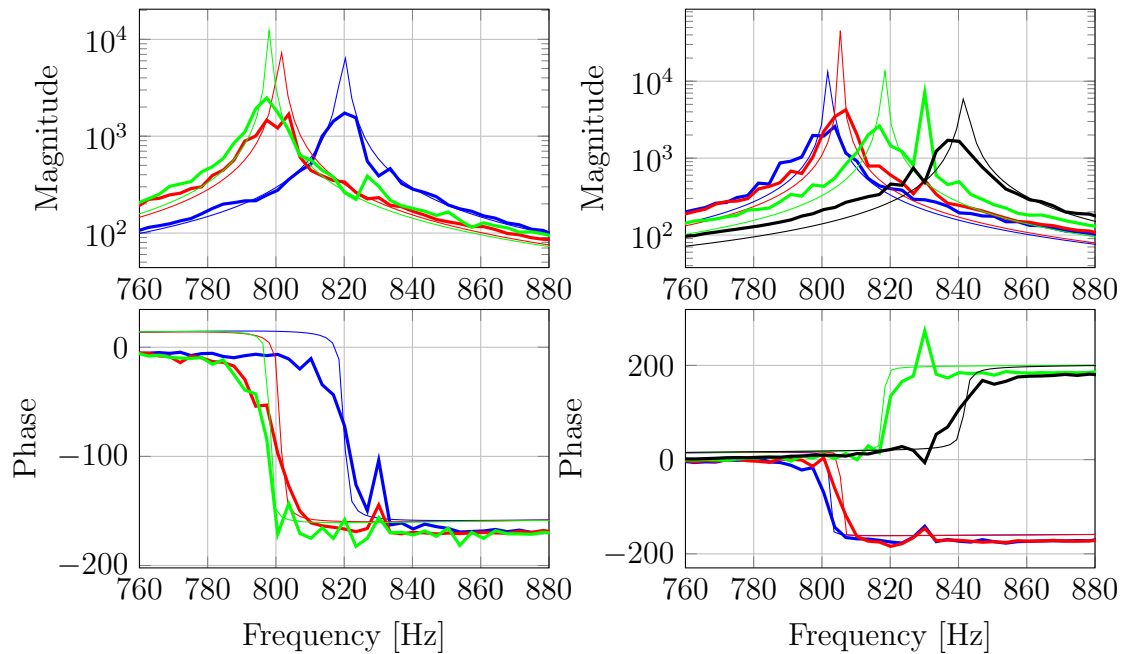


Figure 38: This is the open loop gain fit of the last 7 measurements taken during a segment of time in which the cavity was continuously locked. The three traces in the top two plots are of the stable spring with a large negative detuning. They correspond to the three blue dots from figure 37 with the most negative subcarrier detuning. The thick traces in all plots are from the measurements in the lab. The thin traces are of the modelled open loop gain. The trap cavity had been locked for a few hours at this point and seemed to have stabilized compared to earlier in the lock segment. These measurements were taken no more than 5 minutes apart from each other so the effects of any drifting were minimized.

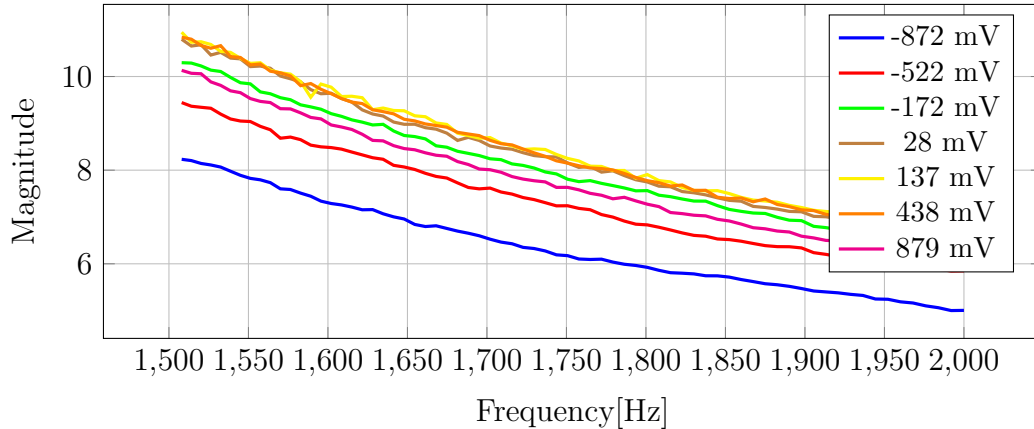


Figure 39: Relative gain above resonant frequency for different subcarrier detunings. The peak gain appears to be at an offset of about 250mV which contradicts the fit in figure 37. This provides further motivation to constrain the measurements better by monitoring key parameter needed to fit the model.

PD10CS set to 0dB gain has a bandwidth of 17MHz. In the resonant RFPD we see the beat between the carrier beam and the sideband of the subcarrier beam because the linewidth of the resonance in the PD is also greater than the subcarrier servo offset frequency. For a subcarrier offset of 355kHz, the RFPD gain is only a couple dB below the peak gain at ≈ 35.1 MHz. These values are taken from the plot in figure 40.

We observed that, with the power on the RFPD at the nominal value to give us a 20kHz unity gain frequency, the signal directly from the RFPD was nearly the $\pm 5V$ of the supply voltage to the op-amp. By varying the power onto the RFPD we could see that the signal in fact did not get much larger and seemed to be at point where the size of the beat signal did not increase at the same rate as the overall power.

Saturations in the electronics can cause unpredictable electronic offsets in the trap locking feedback servo resulting in an error on the subcarrier detuning lock point. We solved this problem by using a polarizing beam splitter (PBS) cube to combine the two beams instead of a non-polarizing beamsplitter. The carrier polarization was set to s and the subcarrier polarization to p. We made the beams incident to the PBS cube such that the carrier was reflected along the path of the transmitted subcarrier beam. The resulting combination of orthogonally polarized beams was propagated to experiment. An added benefit was that we could combine the beams with little loss

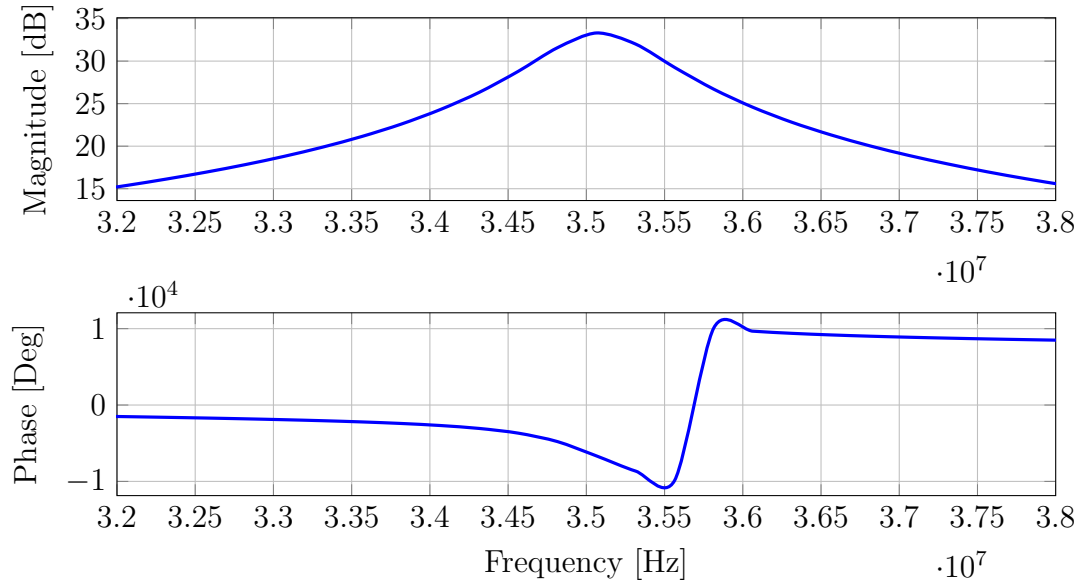


Figure 40: A Bode plot of the 35MHz RFPD response. Beating the subcarrier beam sidebands with the carrier beam creates beat frequencies that lie within the linewidth of the RFPD peak response.

of power.

A quarter wave-plate was needed in the combined path due to some ellipticity in the reflected beam. This is apparently from birefringence in the window to the vacuum chamber. The birefringence causes a phase delay in one linear polarization of light with respect to its orthogonal counterpart. If there is only one birefringent optic in the path we could use a half wave-plate and simply rotate the orthogonal beams so they align with the fast and slow axes of the birefringent material. The quarter wave-plate solves this with an added benefit of having the flexibility to rearrange the return beams. One could direct the carrier back along the subcarrier and vice-versa, for instance.

Additional improvements included several things to make the experiment easier. We added a camera to look at the reflected beam which helped with alignment.

We also added some polarization cubes to take advantage of the orthogonal polarizations and monitor the two transmitted beams independently.

Aligning the beam to the cavity using the steering mirrors on table 2 was very difficult because the cavity mirrors could get excited quite easily from touching the

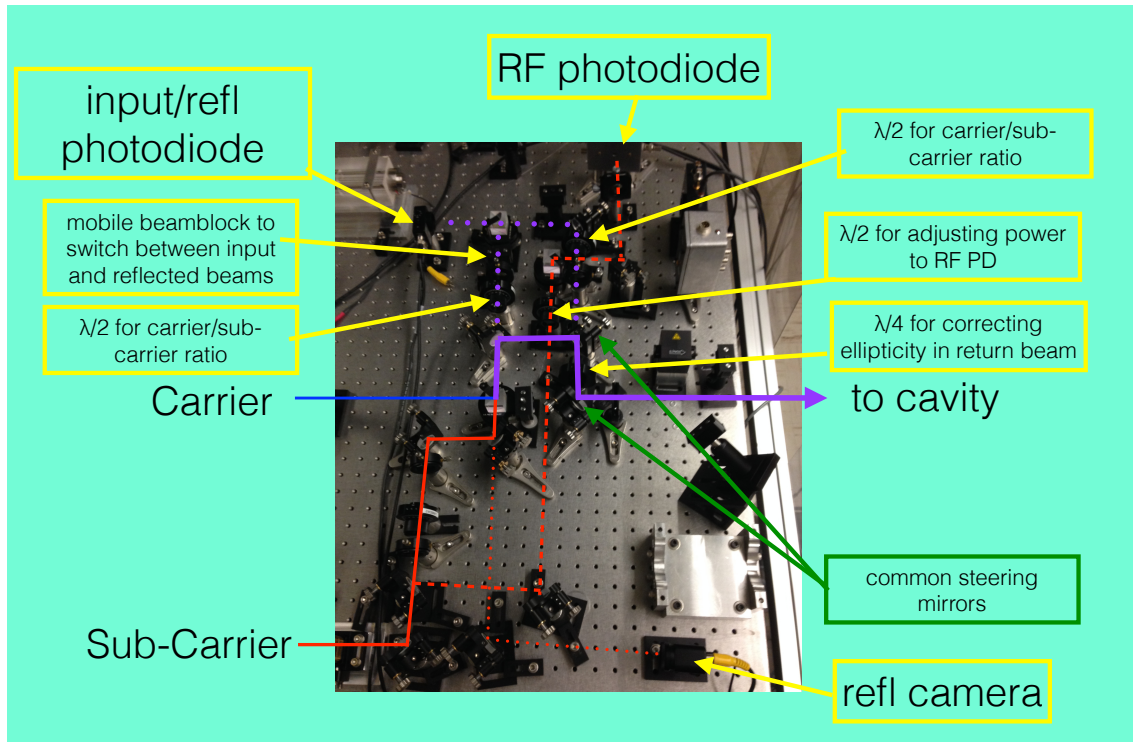


Figure 41: new input optics located on table 1. By replacing the faraday isolator with a PBS the new layout allows for orthogonal polarizations of the two beams. We needed this to reduce the beat signal of the two beams on our photodiodes.

table. So we added steering mirrors on table 1 after the carrier and subcarrier beams are combined. This allowed us to compensate for drifts in alignment between the two tables without having to touch table 2. The new layout can be seen in figure 41.

6.3.1 Faraday Isolator

The Faraday isolator is composed of a Faraday rotator and two PBS cubes. The Faraday rotator is a medium which in the presence of a magnetic field will rotate the polarization of light as it propagates through the medium. There are other, much simpler devices that can rotate the polarization. However, the advantage of the FI is that it will rotate the polarization in a fixed direction relative to the lab and not relative to the direction of propagation.

In the case of the Faraday isolator, the polarization is rotated by 45 degrees so that any reflected light comes back through the FI with a 90 degree rotation. The

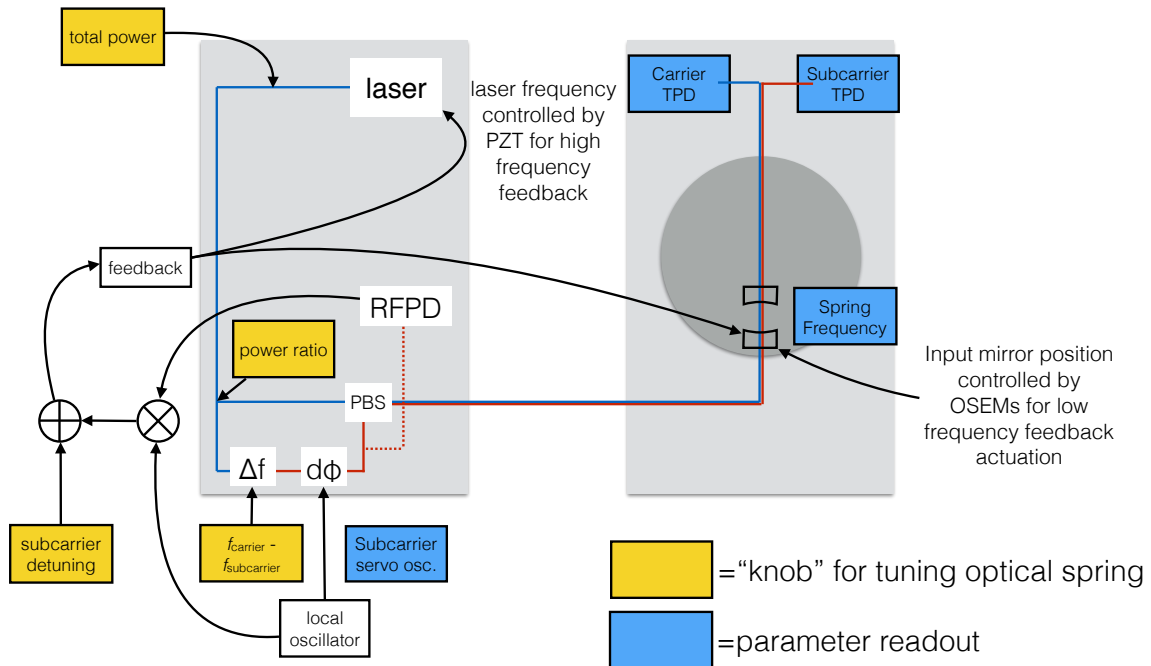


Figure 42: new experimental control scheme. We have moved the experimental control parameter readout closer to the cavity. This gives us smaller errors on the actual parameters of the optical spring. Alignment and laser intensity drifting was too large for us to be able to rely on simply measuring the power at the input to the experiment. We needed a way of monitoring the amount of power which actually couples into the cavity. Which we do by looking at the DC power in transmission for each beam. This is now much easier with the orthogonally polarized beams. It would be difficult to accurately measure the transmitted powers by decomposing the beat signal in the transmitted PD.

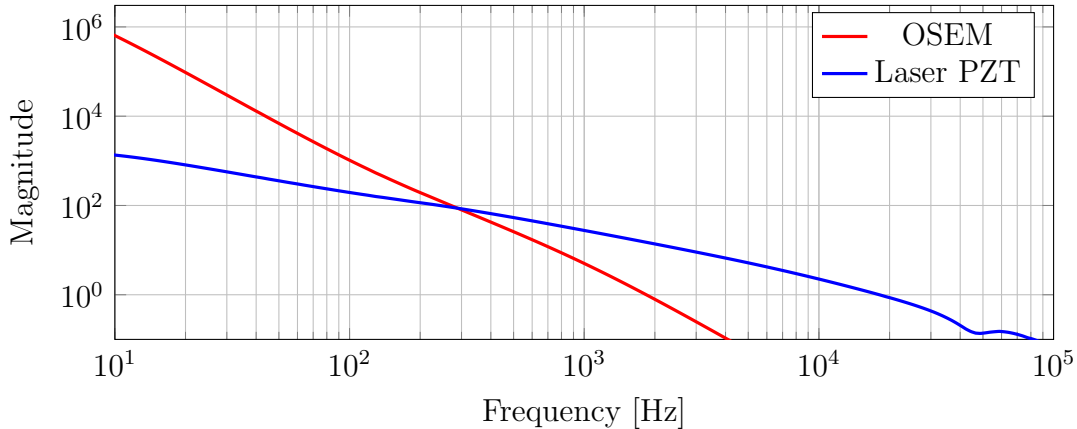


Figure 43: Active feedback used for the second edition of the experiment. This shows each of the two actuation paths used with the crossover point.

isolation is then done by adding a PBS cube at the input to the Faraday rotator. Then we also add one on the output because there will often be additional optics that will disturb the polarization of the reflected light entering the FI from the output side. Another way of putting it is that the PBS on the input side transmits only the linear polarization that will transmit through the output PBS. The output PBS transmits only the linear polarization that will be reflected by the input PBS.

6.4 Linear Trap Experiment, 2nd Edition

With the changes described above in place, we were able to observe several stable and unstable springs as before. This time the measurement procedure was to vary the frequency offset between carrier and subcarrier for each measurement, keeping the other settings fixed. We chose this procedure to simplify the data fitting afterwards. We know the subcarrier servo offset frequency with much better accuracy than we know the subcarrier detuning. Also, changing the subcarrier detuning changes the gain of the system to some extent because the PDH error signal is not linear at the scale of large detuning changes. The change in gain due to subcarrier offset can be seen in figure 39

For active feedback we used two actuation paths, one to the laser piezo electric transducer (PZT) and one to the optical sensing electro-magnet (OSEM) actuators which provide a force to the input mass. The electronic servo which is common to

Measurement ID	Subcarrier Servo Offset [kHz]	Resonant Frequency [Hz]
2-13	330	274.8
2-20	330	370.7
2-10	320	424
2-15	300	609
2-18	260	915
2-19	240	1047

Table 5: Parameters of measurements presented in figure 45.

both paths had the 100 Hz integrator engaged. This integrator has a flat response above 100 Hz and provides a boost below 100 Hz for better seismic suppression. The two paths have a crossover frequency of 200Hz as can be seen in figure 43.

With the orthogonal polarization of the beams, we were able to monitor the transmitted power for each beam. The optical spring has four parameters that can change during the measurement: carrier power, subcarrier power, carrier detuning, and subcarrier detuning. The measurements of the carrier and subcarrier transmitted powers, the observed resonant frequency, and the subcarrier servo offset form a set of parameters from which we can determine the optical spring parameters leaving us with no free parameters in the fitting.

Measurement parameters and spring frequencies can be seen in table 5. The subcarrier detuning was set by checking the carrier power; then increasing the subcarrier servo offset by 50kHz, which increases the carrier detuning by 50kHz because of the lock offset; then changing the electronic offset for the subcarrier detuning to get back to the original carrier transmitted power. This procedure allowed us to use the well defined frequency offset from the subcarrier servo to set the subcarrier detuning to -50kHz. The uncertainty with this comes from noise in the transmitted carrier PD signal relative to the slope of W/Hz (Transmitted Power/Carrier Detuning).

When fitting the data using the technique above, we were not able to get the stability to fit correctly, see figure 46. The measured springs were consistently more unstable than the model. This gave an indication that our model must be missing some physics. With the addition of an effect from the thermal expansion of the high reflective optical coatings, we were able to fit the stability properly.

Thermal expansion couples into the transfer function by absorption of the circulating power in the cavity at the surface of the mirror expanding the optic and making the cavity length shorter. This will be explained in more detail in section 6.4.2. It turns out that only about 5ppm absorption is required to account for the discrepancy in stability. This is, in part, due to the high circulating power and the small beam spot size on the cavity end mirrors. The results of this fitting can be seen in figure 45.

6.4.1 Optical Spring Cavity Residual Motion

We want to know the residual motion of the cavity if we were to remove the active feedback. In order to do this we need to measure the control signal while locked with a stable spring. The control signal is the output of the feedback servo before the actuation. Since the error point (input to feedback servo) is set to zero by the feedback servo below the unity gain frequency of the loop, the control signal tells us what actuation is required to cancel noise entering the system. This allows us to estimate how much motion there would be if we remove the active feedback loop. Knowing the actuation transfer functions, we can convert the control signal to the length noise entering the system. We have two actuation paths, to the laser and to the test mass actuator (OSEM) with a crossover frequency of 300Hz. The sensing and feedback we will call F . So the open loop gain is AF in the absence of the optical spring. With the optical spring, this becomes $\frac{AF}{1-O}$, where O is the open loop gain of the optical spring. Closing the loop, the control signal f will be,

$$\frac{Fn}{1 - (O + AF)} . \quad (6.11)$$

Since AF is much larger than everything else in the denominator below the unity gain frequency, we get,

$$f \approx -\frac{1}{A}n , \quad (6.12)$$

where n is the noise entering the system. Taking the inverse of the equation (6.11) gives us a function to convert the measured control signal to the length noise entering the system. We can then apply the closed loop gain of the optical spring loop to compute what the residual length motion of the cavity would be in the absence of the active feedback.

$$\frac{(1 - O - AF)}{F(1 - O)} f \quad (6.13)$$

Since we have made a measurement G that includes the optical spring,

$$G = \frac{AF}{1 - O}, \quad (6.14)$$

We can replace $1 - O$ in equation (6.12) with $\frac{AF}{G}$. With a bit of algebra we get,

$$n = \frac{1 - G}{F} f. \quad (6.15)$$

The result of this measurement is shown in figure 47 where the noise measurement was taken with the spring from measurement #2-13.

It can be seen from the plot that the residual rms motion is about 1.3×10^{-11} m. We want this to be less than the stability range as defined in section 6.1.1. The response is non-linear for motion on the order of the stability range.

The stability range can be seen for various detunings in figure 35. There is a trade off between phase and frequency however. The lower phase will create a higher Q spring resonance which will amplify the noise entering the system at the resonance more than the higher phase/ lower Q spring resonance. At higher frequencies, the noise entering the system is enough lower to compensate for the higher Q (see fig. 34) so that we can reduce the overall rms motion. We can also see that noise dominating the rms motion at low frequencies is from the bounce mode of our vertical isolation at about 7 Hz and pure seismic takes over below about 3 Hz.

Purely Passive Spring

With a 800Hz optical spring using the same total input power used in this experiment we see that we can get the rms motion at the resonance down to about the 2.5 pm limit. This is marginally good enough at the resonance but we would still need active feedback for the noise below 10Hz.

To improve the stability of the spring we have three main areas we can address: the residual motion at the resonance frequency, the residual motion below 10 Hz, and the stability range itself.

At the resonant frequency we can increase the laser power which we can use to increase the spring frequency further, decrease the Q , or a combination of the two. The increased laser power will result in an increase in the intensity noise however the limiting factor is still the laser frequency noise.

We can also decrease the noise entering the system at 800Hz. The limit here is laser frequency noise. We will need to implement the frequency stabilization servo (FSS) in order to improve this, however we need the full actuation range of the laser PZT for lock acquisition. Once lock is acquired we can separately acquire the FSS and change the feedback scheme to make the laser follow the reference cavity. This would drop the frequency noise down to the level of the voltage controlled oscillator (VCO) noise which is at $0.1\text{Hz}/\sqrt{\text{Hz}}$ at 800Hz, corresponding to $2.5 \times 10^{-17}\text{Hz}/\sqrt{\text{Hz}}$. Thus the noise budget would then be limited by the laser intensity noise, which is at the level of about $5 \times 10^{-16}\text{Hz}/\sqrt{\text{Hz}}$ at 800 Hz. This drops the overall noise at 800 Hz by a factor of 20, reducing the rms noise to roughly $1.3 \times 10^{-13}\text{m}/\sqrt{\text{Hz}}$.

For the low frequency motion we can simply keep the feedback engaged below 10Hz. Also, by increasing laser power to improve the rms motion at high frequency, we will also improve the rms motion at low frequency, either by having a stronger spring which will improve the low frequency suppression or by increasing the phase of the optical spring which will increase the stability range for the system. Another option for improving the motion at low frequencies would be to add an additional seismic isolation stage. This would be a common isolation platform with a resonant frequency below about 0.5 Hz. The design is already partially complete on this, but was delayed due to complexity. The main difficulty with this will be controlling it below the resonant frequency for alignment.

6.4.2 Optic Thermal Expansion Contribution

The power fluctuations which provide the force feedback for the optical spring also cause fluctuations of the absorbed power at the surface of the mirror. This leads to thermal expansion fluctuations of the mirror changing the length of the cavity. The effect was observed during initial LIGO as a noise coupling, see [17]. The relevant part that we are interested in is the effect of changing the thickness of the optic itself due to thermal expansion.

At the frequencies we're interested in, the depth of the thermal expansion oscillations is very shallow compared to the thickness of the optic due to the slow heat conduction through the optic substrate. We want to first consider this penetration

Measurement ID	Carrier Detuning [kHz]	Subcarrier Detuning [kHz]	Carrier Power [mW]	Subcarrier Power [mW]
2-13	290.8	-39.2	215.9	62.5
2-20	285.0	-45.0	213.3	53.8
2-10	285.1	-34.9	223.0	63.7
2-15	264.2	-35.8	215.2	54.6
2-18	238.2	-21.8	224.2	52.5
2-19	222.5	-17.5	228.5	51.7

Table 6: Parameters of measurements presented in figure 45.

depth d of the thermal fluctuations. This is given by,

$$d = \sqrt{\frac{\kappa}{2\pi f C \rho}} = 18.4 \mu\text{m} \sqrt{\frac{400\text{Hz}}{f}}. \quad (6.16)$$

I have written the equation in this form to illustrate that at the lower optical spring frequencies from the experiment, we have a maximum penetration depth of about $18\mu\text{m}$. This is nearly an order of magnitude smaller than the beam spot diameter, which is about $320\mu\text{m}$. The change in thickness Δz of the optic can then be approximated with

$$\Delta z = (1 + \eta) \alpha \frac{\delta P}{2\pi i f C \rho A}, \quad (6.17)$$

where δ is the absorption coefficient, A is the area of the beam, α is the linear coefficient of thermal expansion, and η is the Poisson ratio.

From equation 6.17 we can get the transfer function from force to traplength. With a factor of $c/2$ to remove the optical power to force from the optical spring K_{OS} , the transfer function depicted in figure 44 is

$$\frac{-c\delta\alpha(1+\eta)}{4\pi i f C \rho A}. \quad (6.18)$$

The majority of the change in power buildup due to cavity length is due to the carrier beam which has a positive detuning. Because of this detuning, expansion of the optics will shorten the cavity and increase the intracavity power. The intracavity power fluctuations will thus have a positive feedback and add to the instability of the optical spring.

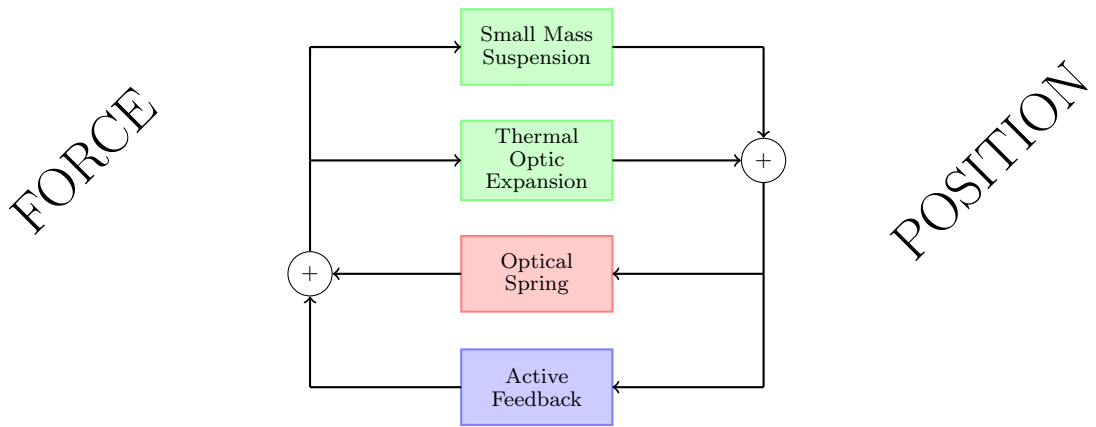


Figure 44: This shows how the thermal expansion effect couples into the experiment. Active feedback represents the two feedback paths displayed in figure 16.

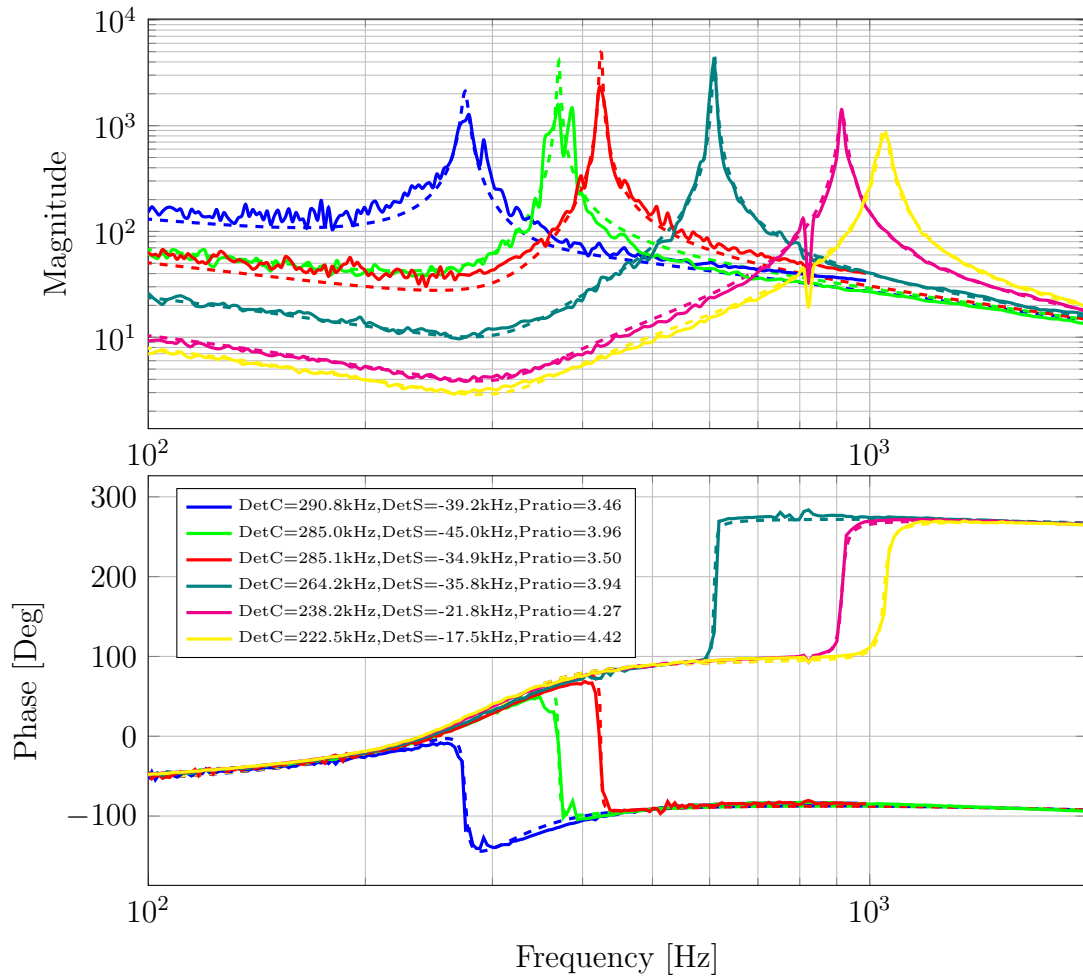


Figure 45: This is the open loop gain fit for the second edition of the experiment. The solid lines are the measured optical spring transfer functions. The dashed lines are the corresponding theoretical transfer functions. In the legend, "DetC" and "DetS" stand for carrier and subcarrier detuning respectively. Pratio is the power ratio of carrier to subcarrier input power.

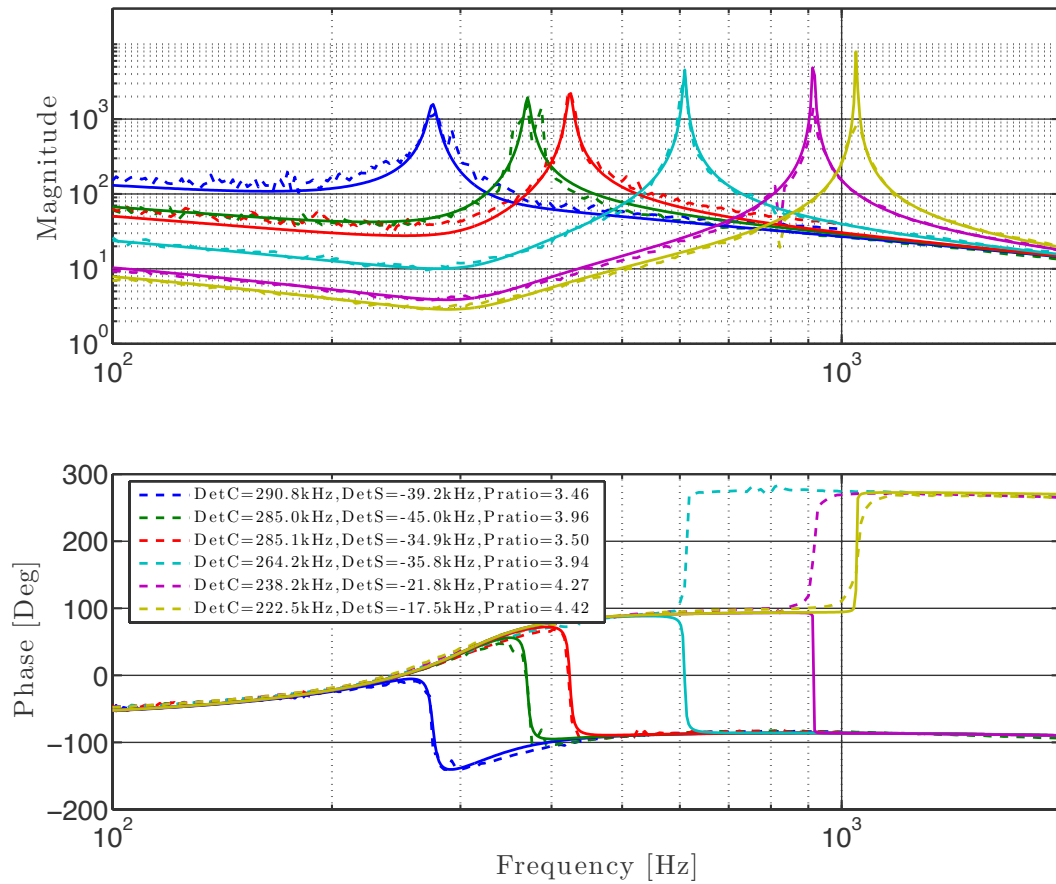


Figure 46: Open loop gain measurements of the second edition of the experiment. This plot shows the fit without the absorption term. Two of the optical springs become stable which does not match with the measurement.

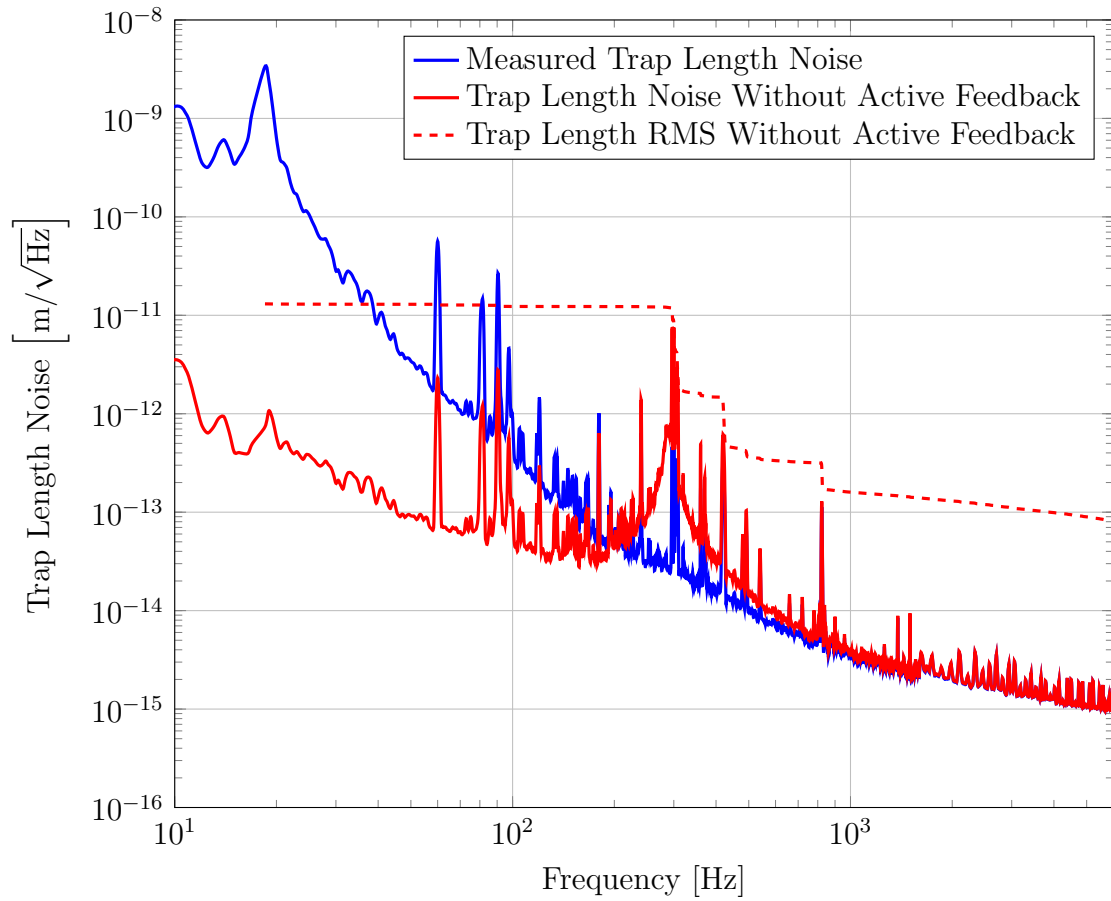


Figure 47: This is the noise budget which includes the measured cavity length noise with a stable optical spring.

Chapter 7

Conclusions

I have shown that the optical trap works for one degree of freedom and matches well with the theory if we include the effects due to thermal expansion. This thermal expansion effect adds an interesting contribution to the transfer function. Unfortunately, this effect works against us to destabilize the mirror.

This discovery indicates that we will have to balance the power density with absorption limits for the optics we're using in optical trapping applications.

7.1 Implications for Angular Trap Experiment

In the case of the angular trap we need to consider the beam size on the test mass. If we assume the configuration as presented in section 2.1 we need to consider a stable 3 mirror cavity which, topologically is a four mirror ring cavity with the test mass acting as the 2nd and fourth mirrors. If all of the radius of curvatures are the same, the stability condition is basically that of a two mirror cavity. In any case, the 2nd mirror is at an angle to the resonant beam and will impart an interference pattern on the surface of the mirror. So, the power distribution on the mirror will be of the form,

$$p = 2 \sin^2(k_t x) \times e^{-(x+y)^2/w^2}, \quad (7.1)$$

where k_t is the transverse k-vector across the interference pattern. Since the integrated power is the same, and there is an interference pattern, the maximum power density must increase by a factor of 2. Therefore the integration of $p^2 dA$ increases by a factor of 4. Thus the effect due to thermal expansion increases by a factor of 4.

To minimize the effects due to thermal expansion, we will particularly need to pay attention to the beam spot size on the test mass due to the angled beam. The stability condition for the cavity can be determined by considering the ABCD propagation matrix for the system. Each round trip will have the following matrix overall,

$$\mathbf{M} = \mathbf{M}_{R3}\mathbf{M}_L\mathbf{M}_{R2}\mathbf{M}_L\mathbf{M}_{R4}\mathbf{M}_L\mathbf{M}_{R2}\mathbf{M}_L, \quad (7.2)$$

where \mathbf{M}_R represents the ABCD matrix for each mirror

$$\mathbf{M}_R = \begin{pmatrix} 1 & 0 \\ \frac{2g-2}{L} & 1 \end{pmatrix}, \quad (7.3)$$

and \mathbf{M}_L represents the ABCD matrix for the propagation through length L . The eigenvalue equation which needs to be solved is then,

$$\lambda^2 - \text{Tr}(\mathbf{M})\lambda + \text{Det}(\mathbf{M}) = 0. \quad (7.4)$$

It turns out that the solution has the form,

$$\lambda = \alpha \pm i\sqrt{1 - \alpha^2} \quad (7.5)$$

with,

$$\alpha = 1 - 4g_3g_2 - 4g_4g_2 + 8g_3g_2^2g_4. \quad (7.6)$$

For $|\lambda|^2 = 1$,

$$\lambda = e^{i\phi} \quad (7.7)$$

where,

$$\alpha = \cos(\phi) \quad (7.8)$$

We will still want the angular stability condition for beam A of $g_1 < 0$ and $g_2 < 0$ because the experiment we have outlined only stabilizes the yaw angular degree of freedom. The pitch degree of freedom still needs to be stable on it's own.

This results in the following condition (for $g_2 < 0$ in order to preserve stability of linear trap, where $0 < g_1g_2 < 1$, and $g_1 < 0$),

$$0 \leq (1 - 2g_3g_2)(1 - 2g_2g_4) \leq 1 \quad (7.9)$$

The corresponding resonant mode of the cavity will have $R_{\text{beam}} = R_{\text{mirror}}$ at mirrors 3 and 4.

If we make R_4 infinite, i.e. flat mirror, we can have a stable resonator with $g_3 \leq \frac{2}{g_2-2}$. Since we keep g_2 bounded by $-1 < g_2 < 0$, it is sufficient to require $g_3 < -1$.

For beam A we can increase the cavity length to about 9cm while still having the stability requirement for $g_1 g_2 < 1$ and the spot size will be a bit larger. We can also go to a larger radius of curvature and even longer cavity, with the consequence of going to a more massive test mass. Parameters for a few configurations are provided in table 7.

parameter	configuration 1	configuration 2	configuration 3	configuration 4
Beam A				
L_A [cm]	7	11	11	12
R_1 [cm]	5	7.5	7.5	7.5
R_2 [cm]	5	7.5	7.5	7.5
w_0 [μ m]	88	106	106	101
w_1 [μ m]	161	205	205	225
w_2 [μ m]	161	205	205	225
$L_{\text{roundtrip}}$	14cm	22cm	22cm	24cm
\mathcal{FSR}	2.141 GHz	1.363 GHz	1.363 GHz	1.249 GHz
\mathcal{F}	8650	8650	8650	8650
γ	778 kHz	495 kHz	495 kHz	454 kHz
Beam B				
L_{B1} [cm]	7	12	14	13.5
L_{B2} [cm]	7	13	14	14.5
R_3 [cm]	5	5	7.5	7.5
R_4 [cm]	5	5	7.5	7.5
w_0 [μ m]	88	31	80	71
w_0 [μ m]	88	35	80	111
w_3 [μ m]	161	553	308	351
w_2 [μ m]	161	778	308	309
w_4 [μ m]	161	483	308	231
$L_{\text{roundtrip}}$ [cm]	28	50	56	56
\mathcal{FSR}	1.071 GHz	600 MHz	535 MHz	535 MHz
\mathcal{F}	4960	4960	4960	4960
γ	678 kHz	380 kHz	339 kHz	339 kHz
TM mass	0.415g	1.17g	1.17g	1.17g

Table 7: This table provides different possible angular trap configurations we can employ using existing optics. Beam A forms the two-mirror cavity as in the linear trap. Beam B forms the V-shaped offset cavity for providing angular stability as seen in figure 5. L_A corresponds to the length of the Beam A cavity. R_1 and R_2 are the radius of curvature for the input and output mirrors respectively for the Beam A cavity. R_3 and R_4 are for the input and end mirrors respectively for the Beam B cavity. The mirror at the vertex of the V-shaped cavity is the output mirror for Beam A. The beam sizes are denoted with w . w_0 for Beam A is the waist size. The first beam waist under Beam B is the waist of the beam in the length L_{B1} . The beam sizes w_n , with $n > 0$ are the spot sizes on the mirrors corresponding to R_n . The second beam waist is for the beam in length L_{B2} . $L_{\text{roundtrip}}$ is the roundtrip length of each cavity which is used to compute the free spectral range (\mathcal{FSR}). The \mathcal{FSR} with the finesse (\mathcal{F}) are used to compute the linewidth γ .

Appendix A

Optical Spring Derivation

A.1 Optical spring constant derivation

In this section we consider the effect of light stored in a detuned Fabry-Perot cavity using a classical approach. The intra-cavity power generates radiation pressure that exerts on the cavity mirror a force $F_{rad} = -K_{OS} \cdot x$, where x is the mirror displacement and K_{OS} is the optical spring constant. Here we show the full derivation of the optical spring constant K_{OS} .

We consider a suspended Fabry-Perot cavity of length L_0 with an incident beam of wavelength λ and power P_0 . First we calculate a general expression of the intra-cavity power and then its radiation pressure force exerted on the end mirror.

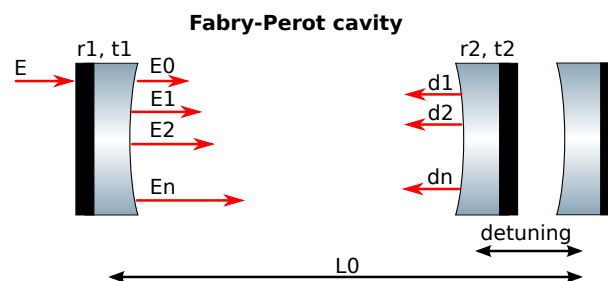


Figure 48: A Fabry-Perot cavity of length L_0 and coefficients r_1, t_1 and r_2, t_2 for the input and end mirrors respectively. The input mirror is stationary while the end mirror is affected by harmonic motion. The incoming field E at each round-trip i adds up a phase shift due to the displacement d_i

The field $E = A_0 e^{i\omega t}$ enters the cavity through the input mirror of coefficient $t_1 = t$ and r_1 and the field inside the cavity at the input mirror can be seen as following

$$E_{tot} = E_0 + E_1 + E_2 + E_3 + \dots + E_n + \dots \quad (\text{A.1})$$

We consider in our model the following definitions, with d_n being the displacement of the mirror,

$$L_1 = 2(L_0 + d_1) \quad (\text{A.2})$$

$$L_2 = 2(2L_0 + d_1 + d_2)$$

$$L_3 = 2(3L_0 + d_1 + d_2 + d_3)$$

...

with

$$d_n = d(t - [(2n - 1)\tau + \alpha_n]) \quad \text{and} \quad (\text{A.3})$$

$$\alpha_n = 2 \sum_{l=1}^{n-1} \frac{d_l}{c} - \frac{d_n}{c} \quad (\text{A.4})$$

where $\tau = L_0/c$. With the round trip length $L = 2L_0$ we obtain

$$\begin{aligned} E_{tot} &= tE(1 + r_1 r_2 e^{-ikL_1} + (r_1 r_2)^2 e^{-ikL_2} \\ &+ (r_1 r_2)^3 e^{-ikL_3} \dots) \\ &= tE(1 + r_1 r_2 e^{-ikL} e^{-2ikd_1} + (r_1 r_2)^2 e^{-2ikL} e^{-2ik(d_1+d_2)} \\ &+ (r_1 r_2)^3 e^{-3ikL} e^{-2ik(d_1+d_2+d_3)} \dots) \end{aligned}$$

If we define $X = r_1 r_2 e^{-ikL}$ we have

$$\begin{aligned} E_{tot} &= tE(1 + X e^{-2ikd_1} + X^2 e^{-2ik(d_1+d_2)} \\ &+ X^3 e^{-2ik(d_1+d_2+d_3)} \dots) \end{aligned}$$

Since by definition the optical spring K_{OS} is the linear term in the expansion $F = F_0 + K_{OS}d + O(d^2)$, we now expand the exponential in d_n . We group d_n terms:

$$\begin{aligned}
E_{tot} &= tE(1 + X(1 - 2ikd_1) + X^2(1 - 2ik(d_1 + d_2)) \\
&+ X^3(1 - 2ik(d_1 + d_2 + d_3)) + \dots) \\
&= tE(1 + X + X^2 + X^3 + \dots \\
&- 2ikd_1(X + X^2 + X^3 \dots) \\
&- 2ikd_2(X^2 + X^3 + X^4 \dots) \\
&- 2ikd_3(X^3 + X^4 + X^5 \dots) + \dots) \\
&= \frac{tE}{1 - X}(1 - 2ikd_1X - 2ikd_2X^2 - 2ikd_3X^3 + \dots)
\end{aligned}$$

Since any correction from α_n (equation A.4) is quadratic in $d(t)$, we can again neglect it by definition, and find for the harmonic mirror motion (i.e. in the Fourier domain)

$$\begin{aligned}
d_n &= x_0 e^{i\Omega(t - (2n-1)\tau)} = x_0 e^{i\Omega t} e^{-i\Omega(2n-1)\tau} \\
&= x_0 e^{i\Omega t} \frac{Y^{2n} Y}{Y} = Y^{2n-2} d_1
\end{aligned} \tag{A.5}$$

where $Y = e^{-i\Omega\tau}$. Thus we can write

$$\begin{aligned}
E_{tot} &= \frac{tE}{1 - X}(1 - 2ikd_1X - 2ikd_1Y^2X^2 \\
&- 2ikd_1Y^4X^3 - 2ikd_1Y^6X^4 \dots)
\end{aligned} \tag{A.6}$$

$$\begin{aligned}
&= \frac{tE}{1 - X} \\
&\times [1 - 2ikd_1X(1 + Y^2X + Y^4X^2 + Y^6X^3 \dots)] \\
&= \frac{tE}{1 - X} \left[1 - \frac{2ikd_1X}{1 - Y^2X} \right]
\end{aligned} \tag{A.7}$$

where d_1 is a complex number. Since we have to take its real part $Re(d_k) = \frac{d_k + \bar{d}_k}{2}$, we consider the field inside the cavity with \bar{d}_k conjugate of d_k :

$$\frac{tE}{1 - X} \left[1 - \frac{2ik\bar{d}_1X}{1 - \bar{Y}^2X} \right] \tag{A.8}$$

and we obtain as total field E

$$E_{tot} = tE \left[\frac{1}{1-X} - \frac{2ikX}{2(1-X)} \left(\frac{d_1}{1-Y^2X} + \frac{\bar{d}_1}{1-\bar{Y}^2X} \right) \right]$$

and its complex conjugate

$$\bar{E}_{tot} = t\bar{E} \left[\frac{1}{1-\bar{X}} + \frac{2ik\bar{X}}{2(1-\bar{X})} \left(\frac{\bar{d}_1}{1-\bar{Y}^2\bar{X}} + \frac{d_1}{1-Y^2\bar{X}} \right) \right]$$

Using the following expression

$$d_1 = x_0 e^{i\Omega(t-\tau)} = x_0 e^{i\Omega t} e^{-i\Omega\tau} = xY \quad (\text{A.9})$$

we can now obtain the intra-cavity power expression by multiplying E_{tot} by its conjugate and considering only the linear terms of x

$$\begin{aligned} P = E_{tot} \cdot \bar{E}_{tot} = P_0 t^2 & \left[\frac{1}{(1-X)(1-\bar{X})} \right. \\ & - \frac{ikXxY}{(1-\bar{X})(1-X)(1-Y^2X)} - \frac{ikX\bar{x}\bar{Y}}{(1-\bar{X})(1-X)(1-\bar{Y}^2X)} \\ & \left. + \frac{ik\bar{X}\bar{x}\bar{Y}}{(1-\bar{X})(1-X)(1-\bar{Y}^2\bar{X})} + \frac{ik\bar{X}xY}{(1-\bar{X})(1-X)(1-Y^2\bar{X})} \right] \end{aligned} \quad (\text{A.10})$$

where we have also neglected the first constant term. We now group the terms in x and \bar{x} :

$$\begin{aligned}
P &= -P_0 t^2 \left[\frac{ikY}{(1-\bar{X})(1-X)} \left(\frac{X}{1-Y^2 X} - \frac{\bar{X}}{1-Y^2 \bar{X}} \right) x \right. \\
&\quad \left. + \frac{ik\bar{Y}}{(1-\bar{X})(1-X)} \left(\frac{X}{1-\bar{Y}^2 X} - \frac{\bar{X}}{1-\bar{Y}^2 \bar{X}} \right) \bar{x} \right] = \\
&= -P_0 t^2 \left[\frac{ikY}{(1-\bar{X})(1-X)} \right. \\
&\quad \left. \times \left(\frac{X}{1-Y^2 X} - \frac{\bar{X}}{1-Y^2 \bar{X}} \right) x + cc \right] \tag{A.11}
\end{aligned}$$

Once we have calculated the power we can obtain the radiation pressure force on the end mirror by $F_{rad} = \frac{2r_2^2}{c} P$. Furthermore we can also notice the similarity of the expression with the elastic force. Thus we recall that in frequency domain and complex notation K is defined by $F = -Kx$, the real form is thus

$$F' = Re[F] = -\frac{1}{2}(Kx + \bar{K}\bar{x}) = -\frac{1}{2}(Kx + cc)$$

Taking into account that we are calculating the radiation pressure on the end mirror, we need to consider an extra delay factor Y for the calculation of the power which appears in the expression of K . The complex spring is then given by

$$K = \frac{2r_2^2}{c} P_0 t^2 \frac{2ikY^2}{(1-\bar{X})(1-X)} \left(\frac{X}{1-Y^2 X} - \frac{\bar{X}}{1-Y^2 \bar{X}} \right)$$

which can be rewritten in the form of equations 2.6 and 2.7.

Detuning

Given the frequency detuning is $\delta = \omega_0 - \omega_{res}$ and $\Omega = \omega - \omega_0$, where ω_0 is the carrier (sub-carrier) frequency and ω_{res} is the resonant frequency, we get the following expressions:

Resonance

$$\begin{aligned}\lambda_{res} &= L/n, & k_{res} &= \frac{2\pi n}{L}, \\ \omega_{res} &= k_{res} \cdot c = \frac{2\pi n}{L} \cdot c\end{aligned}\tag{A.12}$$

Carrier

$$\begin{aligned}\lambda_0 &= \lambda, & k_0 &= \frac{2\pi}{\lambda} = k, \\ \omega_0 &= k_0 \cdot c = \frac{2\pi c}{\lambda} = \omega_{res} + \delta\end{aligned}\tag{A.13}$$

Sideband

$$\omega = \Omega + \omega_0 = \Omega + \delta + \omega_{res}\tag{A.14}$$

Thus we find

$$\begin{aligned}
e^{-ikL} &\equiv e^{-ik_0L} = e^{-i\omega_0 \frac{L}{c}} \\
&= e^{-i(\omega_{res} + \delta) \frac{L}{c}} = e^{-i\omega_{res} \frac{L}{c}} e^{-i\delta \frac{L}{c}}
\end{aligned} \tag{A.15}$$

Recalling that $\tau = \frac{L_0}{c} = \frac{L}{2c}$ we can write

$$e^{-ikL} = e^{-i\delta 2\tau} \tag{A.16}$$

If we now replace X and Y we obtain the exact expression for K :

$$\begin{aligned}
K_{OS} = & -P_0 t^2 r_2^2 \frac{4ik e^{-2i\Omega\tau}}{c(1-r_1 r_2 e^{i2\delta\tau})(1-r_1 r_2 e^{-i2\delta\tau})} \times \\
& \left(\frac{r_1 r_2 e^{-i\delta\tau}}{1-r_1 r_2 e^{-2i\Omega\tau} e^{-i2\delta\tau}} - \frac{r_1 r_2 e^{i2\delta\tau}}{1-r_1 r_2 e^{-2i\Omega\tau} e^{i2\delta\tau}} \right)
\end{aligned} \tag{A.17}$$

To compare to existing literature we now expand the exponentials to linear order in Ω and δ , $e^{-i\delta 2\tau} \approx 1 - i\delta 2\tau$ and $e^{-i2\Omega\tau} \approx 1 - i2\Omega\tau$:

$$\begin{aligned}
K = & -P_0 t^2 r_2^2 \times \\
& \frac{4ik(1-2i\Omega\tau)r_1 r_2}{c(1-r_1 r_2 + r_1 r_2 i2\delta\tau)(1-r_1 r_2 - r_1 r_2 i2\delta\tau)} \times \\
& \left[\frac{1-i2\delta\tau}{1-r_1 r_2(1-2i\Omega\tau-i2\delta\tau)} - \frac{1+i2\delta\tau}{1-r_1 r_2(1-2i\Omega\tau+i2\delta\tau)} \right]
\end{aligned} \tag{A.18}$$

Considering the *Finesse* $\approx \pi \frac{r_1 r_2}{1-r_1 r_2} = \pi FSR/\gamma$, the cavity bandwidth γ , and the free spectral range $FSR = 1/2\tau$, we obtain:

$$\begin{aligned}
K_{OS} \approx & -P_0 t^2 r_2^2 \frac{4ik(1-2i\Omega\tau)r_1 r_2}{c(1+i\frac{\delta}{\gamma})(1-i\frac{\delta}{\gamma})(1-r_1 r_2)^3} \\
& \times \left[\frac{1-i2\delta}{1+\frac{\Omega}{\gamma}i+\frac{\delta}{\gamma}i} - \frac{1+i2\delta}{1+\frac{\Omega}{\gamma}i-\frac{\delta}{\gamma}i} \right]
\end{aligned} \tag{A.19}$$

Finally, since they correspond to a simple time delay, we neglect the $i\Omega\tau$, $i\delta\tau$ terms in the numerator and obtain

$$K_{OS} \approx P_0 t^2 r_2^2 \frac{8kr_1 r_2}{c(1-r_1 r_2)^3} \frac{\frac{\delta}{\gamma}}{(1+\frac{\delta^2}{\gamma^2})} \left[\frac{1}{1+\frac{\delta^2}{\gamma^2}-\frac{\Omega^2}{\gamma^2}+i2\frac{\Omega}{\gamma}} \right] \tag{A.20}$$

Overcoupled cavity

In the particular case of perfectly over-coupled cavity ($r_2 = 1$) $Finesse/\pi = 2/T_1$ and $(1 - r_1 r_2)^2 = T_1^2/2$ and the optical spring constant becomes:

$$K_{OS} \approx 128 P_0 \frac{\pi}{c \lambda T_1^2} \frac{\frac{\delta}{\gamma}}{(1 + \frac{\delta^2}{\gamma^2})} \left[\frac{1}{1 + \frac{\delta^2}{\gamma^2} - \frac{\Omega^2}{\gamma^2} + i 2 \frac{\Omega}{\gamma}} \right] \quad (\text{A.21})$$

Matched cavity

In this case of a matched cavity ($r_1 = r_2$) $Finesse/\pi = 1/T_1$ and $(1 - r_1 r_2)^2 = T_1^2$ and the optical spring constant remains the same as in Eq. A.21 except for the the factor 128 which has to be replaced with 16.

A.2 Torsion pendulum mechanical plant

Here we transform the basis of coordinates $\{x_G, \Theta\}$ formed by the position of the center of gravity x_G of the mirror and its rotation angle Θ with respect to the vertical axis passing from x_G into a basis $\{x_A, x_B\}$ formed by the length of the cavities relative to beam A and beam B respectively. Thus the longitudinal and angular control of the mirror can be treated as the longitudinal control of the two above mentioned cavities. The basis can be expressed as

$$\begin{pmatrix} x_A \\ x_B \end{pmatrix} = \begin{pmatrix} 1 & r_A \\ 1 & r_B \end{pmatrix} \begin{pmatrix} x_G \\ \Theta \end{pmatrix} = \mathcal{B} \begin{pmatrix} x_G \\ \Theta \end{pmatrix} \quad (\text{A.22})$$

with r_A and r_B being the lever arms of the two beams with respect to x_G .

The equation of motion for the mirror is

$$-\omega^2 \begin{pmatrix} m & \\ & I \end{pmatrix} \begin{pmatrix} x_G \\ \Theta \end{pmatrix} = \begin{pmatrix} F_{tot} \\ T_{tot} \end{pmatrix} \quad (\text{A.23})$$

with I being the moment of inertia of the mirror of mass m . We now express the total force and the total torque exerted on the mirror as function of the individual forces F_A and F_B :

$$\begin{pmatrix} F_{tot} \\ T_{tot} \end{pmatrix} = \begin{pmatrix} 1 & 1 \\ r_A & r_B \end{pmatrix} \begin{pmatrix} F_A \\ F_B \end{pmatrix} = \mathcal{B}^T \begin{pmatrix} F_A \\ F_B \end{pmatrix} \quad (\text{A.24})$$

Using equations A.24 and A.22 in equation A.23 we obtain the equation of motion in the x_A, x_B basis:

$$-\omega^2 \left[\mathcal{B}^{T-1} \begin{pmatrix} m & \\ & I \end{pmatrix} \mathcal{B}^{-1} \right] \begin{pmatrix} x_A \\ x_B \end{pmatrix} = \begin{pmatrix} F_A \\ F_B \end{pmatrix} \quad (\text{A.25})$$

A.3 Stability in two dimensions

The control loop stability in multiple dimensions can be evaluated by considering the one-dimensional open-loop transfer function of every control filter (i.e. optical spring) while all other loops stays closed. Here we calculate these open-loop transfer functions for the two-dimesnional case.

Referring to figure 6, we inject a signal $F_{xa} = F_{\text{ext}}$ into port A. The output at port A is $F_{ya} = F_A$. We close the loop from output B to input B by feeding back the force F_B . We obtain the following expression:

$$HM \begin{pmatrix} 0 \\ F_B \end{pmatrix} + HM \begin{pmatrix} F_{xa} \\ 0 \end{pmatrix} = \begin{pmatrix} F_{ya} \\ F_B \end{pmatrix} \quad (\text{A.26})$$

If we introduce the 2×2 matrix S :

$$S_A = \begin{pmatrix} 0 & 0 \\ 0 & 1 \end{pmatrix} \quad (\text{A.27})$$

we can write

$$HMS_A \begin{pmatrix} F_{ya} \\ F_B \end{pmatrix} + HM \begin{pmatrix} F_{xa} \\ 0 \end{pmatrix} = \begin{pmatrix} F_{ya} \\ F_B \end{pmatrix} \quad (\text{A.28})$$

Using the vector $e_A^T = (1, 0)$ we are able to extract the following open loop transfer function related to cavity A:

$$OL_A = \frac{F_{ya}}{F_{xa}} = e_A^T (\mathbb{I} - HMS_A)^{-1} HM e_A \quad (\text{A.29})$$

The same open loop transfer function can be obtained considering an external signal injected into the loop of the beam B while the loop of beam A remains closed.

$$OL_B = \frac{F_{yb}}{F_{xb}} = e_B^T (\mathbb{I} - HMS_B)^{-1} HM e_B \quad (\text{A.30})$$

with $e_B^T = (0, 1)$ and

$$S_B = \begin{pmatrix} 1 & 0 \\ 0 & 0 \end{pmatrix} \quad (\text{A.31})$$

Appendix B

More Derivations

B.1 Mode Matching

As will be discussed in section 6.3, we went through a revision in our overall layout. This changed the beam size and waist location in reference to the cavity. We did not want to open the chamber again for alignment and mode matching. It was useful to know the power coupling into the cavity with the wrong mode matching to give us an idea of how much transmitted light we should expect when the cavity is properly aligned since mode matching is a difficult process of moving the lenses along the beam path and realigning the beam.

We want to know how much power couples into the cavity from a perfectly gaussian beam of the wrong size and location. We start with the equations for the Hermite-Gaussian beam decomposition as discussed in Siegman [10].

$$\begin{aligned}
 c_{nm} &= \int_{-\infty}^{\infty} \int_{-\infty}^{\infty} E(x, y, z) u_n^*(x, z) u_m^*(y, z) dx dy \\
 &= \int_{-\infty}^{\infty} \int_{-\infty}^{\infty} E(x, y, z) u_0^*(x, z) u_0^*(y, z) dx dy \\
 &= \int_{-\infty}^{\infty} \int_{-\infty}^{\infty} u_0(x, z - z_0) u_0(y, z - z_0) u_0^*(x, z) u_0^*(y, z) dx dy \quad (\text{B.1})
 \end{aligned}$$

We now assign the labels b for the beam and c for the cavity,

$$\begin{aligned}
c_{00} &= \int_{-\infty}^{\infty} \int_{-\infty}^{\infty} u_{b0}(x, z - z_0) u_{b0}(y, z - z_0) u_{c0}^*(x, z) u_{c0}^*(y, z) dx dy \\
&= \int_{-\infty}^{\infty} \int_{-\infty}^{\infty} \left(\frac{2}{\pi w_0^2} \right) \left(\frac{q_{b0}}{q_b(z)} \right) \left(\frac{q_{c0}^*}{q_c^*(z)} \right) \exp \left[-ik (x^2 + y^2) \left(\frac{1}{2q_b(z)} + \frac{1}{2q_c^*(z)} \right) \right] dx dy
\end{aligned} \tag{B.2}$$

Since $q(z) = q_0 + z - z_0$, and q_0 is purely imaginary,

$$\begin{aligned}
c_{00} &= \int_{-\infty}^{\infty} \int_{-\infty}^{\infty} \left(\frac{2}{\pi w_{b0} w_{c0}} \right) \left(\frac{-q_{b0} q_{c0}}{(q_{b0} + z - z_0)(-q_{c0} + z)} \right) \\
&\quad \exp \left[\frac{-ik (x^2 + y^2)}{2} \left(\frac{(q_{b0} + z - z_0) - (-q_{c0} + z)}{(q_{b0} + z - z_0)(-q_{c0} + z)} \right) \right] dx dy
\end{aligned} \tag{B.3}$$

We start by changing to cylindrical coordinates,

$$\begin{aligned}
c_{00} &= \int_0^{2\pi} \int_0^{\infty} \left(\frac{2}{\pi w_{b0} w_{c0}} \right) \left(\frac{-q_{b0} q_{c0}}{(q_{b0} + z - z_0)(-q_{c0} + z)} \right) \\
&\quad \exp \left[\frac{-ik (r^2)}{2} \left(\frac{(q_{b0} + z - z_0) - (-q_{c0} + z)}{(q_{b0} + z - z_0)(-q_{c0} + z)} \right) \right] r dr d\theta
\end{aligned} \tag{B.4}$$

A careful analysis of the exponent will reveal that the real part must be less than 0. We can therefore solve the Gaussian integral, setting $s = \frac{-ik(r^2)}{2} \left(\frac{(q_{b0} + z - z_0) - (-q_{c0} + z)}{(q_{b0} + z - z_0)(-q_{c0} + z)} \right)$,

$$\begin{aligned}
c_{00} &= \int_0^{2\pi} \int_0^{\infty} \left(\frac{2}{\pi w_{b0} w_{c0}} \right) \left(\frac{-q_{b0} q_{c0}}{(q_{b0} + z - z_0)(-q_{c0} + z)} \right) \exp [s] r dr d\theta \\
&= \int_0^{\infty} \left(\frac{4}{w_{b0} w_{c0}} \right) \left(\frac{-q_{b0} q_{c0}}{(q_{b0} + z - z_0)(-q_{c0} + z)} \right) \exp [s] r dr
\end{aligned} \tag{B.5}$$

Now we transform the differential and the limits of integration, remembering that the real part of s is less than 0, $ds = -ik \left(\frac{(q_{b0} + z - z_0) - (-q_{c0} + z)}{(q_{b0} + z - z_0)(-q_{c0} + z)} \right) r dr$,

$$\begin{aligned}
c_{00} &= \left(\frac{4i}{k w_{b0} w_{c0}} \right) \left(\frac{-q_{b0} q_{c0}}{(q_{b0} + z - z_0) - (-q_{c0} + z)} \right) \int_{-\infty}^0 e^s ds \\
&= \left(\frac{4i}{k w_{b0} w_{c0}} \right) \left(\frac{-q_{b0} q_{c0}}{(q_{b0} + z - z_0) - (-q_{c0} + z)} \right) \\
&= \left(\frac{4i}{k w_{b0} w_{c0}} \right) \left(\frac{-q_{b0} q_{c0}}{(q_{b0} + q_{c0} - z_0)} \right)
\end{aligned} \tag{B.6}$$

Now, we rewrite the coefficient in terms of waist sizes and distance between waists, using,

$$q_0 = \frac{i\pi w_0^2}{\lambda}$$

$$k = 2\pi/\lambda$$

$$c_{00} = \frac{2w_{b0}w_{c0}}{w_{b0}^2 + w_{c0}^2 + iz_0\lambda/\pi}$$

$$= \frac{2w_{b0}/w_{c0}}{1 + (w_{b0}/w_{c0})^2 + iz_0/z_R} \quad (\text{B.7})$$

Power coupling into cavity is then (assuming no loss and $r_1 = r_2$),

$$P_{\text{trans}} = P_{\text{incident}} \frac{4w_{b0}^2/w_{c0}^2}{1 + 2(w_{b0}/w_{c0})^2 + (w_{b0}/w_{c0})^4 + (z_0/z_R)^2}$$

$$P_{\text{trans}} = P_{\text{incident}} \frac{4}{2 + (w_{c0}/w_{b0})^2 + (w_{b0}/w_{c0})^2 + (z_0/z_R)^2} \quad (\text{B.8})$$

$$P_{\text{trans}} = P_{\text{incident}} \frac{4}{(w_{c0}/w_{b0} + w_{b0}/w_{c0})^2 + (z_0/z_R)^2} \quad (\text{B.9})$$

In equation B.9 we can see readily the symmetry between w_{b0} and w_{c0} , and the symmetry of z_0 about 0, as expected.

Appendix C

Digital System

C.1 System Overview

In order to provide control of our small optic suspensions, we had the option of building either a digital or analog feedback system. Although either option would work for the experiment the digital system provides additional benefits:

1. Easy modification of feedback loops
2. Builds Familiarity to LIGO digital systems
3. Can be used as a platform for testing new LIGO tools
4. A platform for rapid implementation of future control loops

The digital system employed at Syracuse closely resembles the LIGO digital system. It is composed of the following major components:

1. Real-time Front-end for digital feedback and control
2. ADC and DAC for interfacing digital system with the experiment
3. Data Acquisition
4. Workstation for controlling the experiment, running tests, and analyzing data
5. Boot server for serving the diskless front-end machine

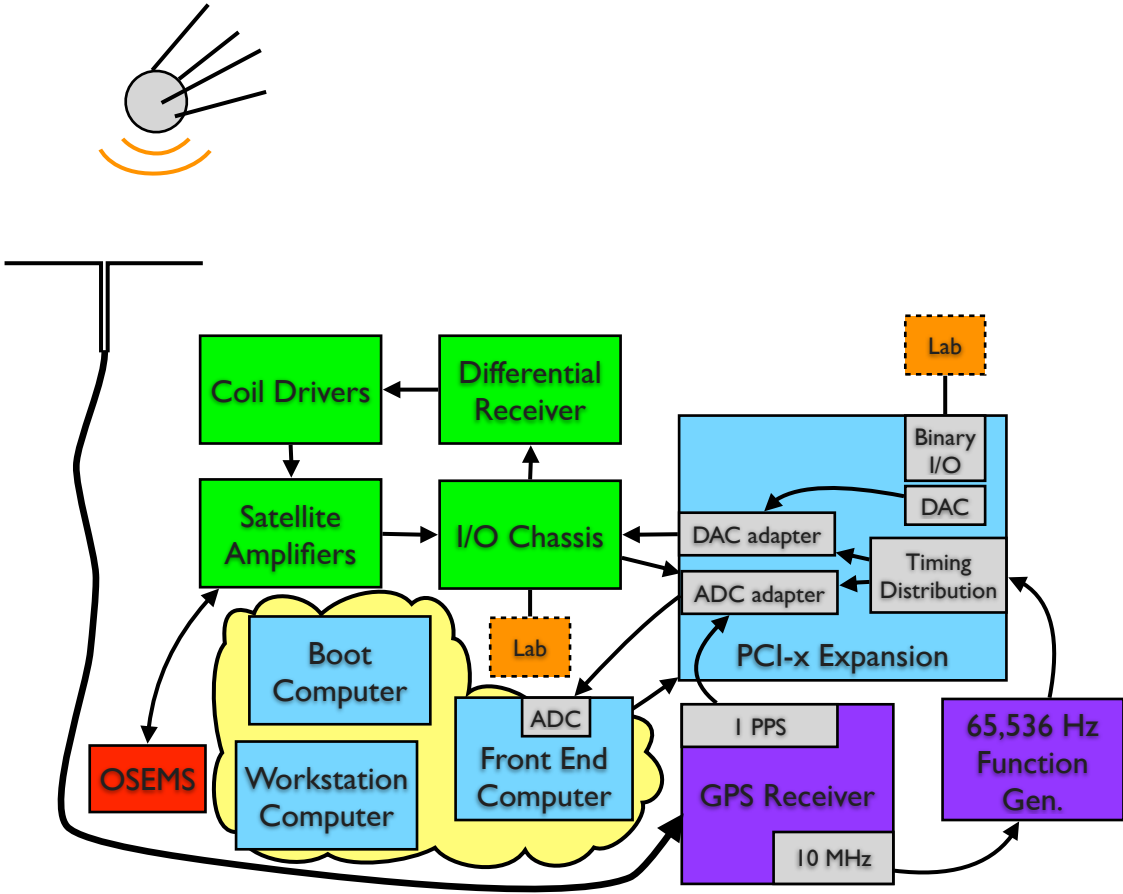


Figure 49: Front End System Overview

From	To	Connection
Front-End Computer	ADC card	PCIe bus
Front-End Computer	Expansion Chassis	PCIe to PCIx adapter
Expansion Chassis	DAC card	PCIx bus
ADC card	ADC adapter card	SCSI cable
DAC card	DAC adapter card	SCSI cable
Expansion Chassis	Binary I/O cards	PCIx bus
Timing Distribution Card	ADC card	coaxial SMB
Timing Distribution Card	DAC card	coaxial SMB
Function Generator	Timing Distribution Card	BNC
GPS Receiver	Function Generator	10 MHz sync BNC
GPS Receiver	ADC adapter card	1PPS BNC

Table 8: This interface matrix depicts the physical interconnectivity of digital system hardware components.

C.1.1 LIGO Real-Time System Theory of Operation

The LIGO Real-Time System provides for discrete, synchronous control of LIGO systems. The sampling frequency can be one of several powers of 2 in Hz. Time is synchronized to GPS time with a sophisticated timing distribution system. The digital processes are run in fixed time steps in order to run feedback signals through them which are analogous to continuous time feedback systems. One can then design a feedback system composed of poles and zeros completely inside the computer. The limitation being that of a bandwidth below the Nyquist frequency for the sampling rate used.

Timing signals are received by the digital system through the ADC/DAC cards. Each model is an individual process which has a limited time to process its data before the next time step begins. Interprocess communication happens at the beginning/end of each time step.

C.1.2 ADC/DAC Hardware Description

C.1.3 Timing

Time steps must be spaced precisely enough to avoid jitter (a phase noise associated with a variable time step). In practice it is impossible to avoid, but we can minimize jitter by referencing a crystal oscillator. Crystal oscillators are notoriously precise by using the natural mechanical oscillations of crystals which have very low mechanical loss.

The timing signal for the front end system is directly generated by a Stanford Research DS345 function generator. It produces a 65,536 Hz signal that clocks the ADC and DAC cards. Over a long period of time the time stamp in the front end can drift relative to the computers that are synced to network time. Some software, particularly Diagnostic Test Tools and probably others, gets confused when the current time in front end does not match network time. This requires a reboot of the front end system to reacquire the correct time.

We installed a GPS receiver (Trimble Thunderbolt E) that will prevent these long term drifts. It produces a 1PPS (Pulse Per Second) signal and a 10 MHz signal. The 1PPS connects to the ADC card through the ADC adapter card which is located in the blue expansion chassis. The 10 MHz signal connects to the external timebase input of the DS345. So, the 65,536 clock is now locked to the GPS time and as such will not drift over long periods of time.

Additionally, the Thunderbolt has an ovenized crystal oscillator that should help with phase noise.

In order to get the GPS antenna signal we needed about 250' of low-loss 1/2" diameter foam core cable (should be easy to spot as it's quite thick). The cable runs out the optics lab, across the hallway overhead and into a cable tray to go down the hallway. The cable runs out of the cable tray by the machine shop, over the hallway, into the machine shop, up to the ceiling, and then along the top of a black drain pipe to the south-east corner of the building. The cable then goes through some grating on the wall and up the shaft to the ground level of the SE corner where the antenna is mounted. (see Fig.50)

The 1PPS signal from the Trimble Thunderbolt GPS receiver is a fixed pulse width of 10 micro-seconds. Since the clock is running at 65,536 Hz, the 1PPS is missed by



Figure 50: The GPS antenna is located

the ADC.

I have fixed this by extending the pulse to about 15 microseconds using a 555 timer chip in monostable mode. The input has to be an inverse pulse so I inverted the pulse in GPS control software. This option is available in the Timing Receiver Configuration window.

See attached NE555P spec sheet (p.9) for the schematic that I used. Only difference is R_L is between output and ground instead of V_{CC} .

I scavenged a 5V power supply from an old 10baseT ethernet hub. I took the ferrites and electrolytic capacitor that were on the supply input in the hub itself and added them to this board for noise suppression.

R_A is a small potentiometer. If you need to adjust the pulse width, just open the case and turn the pot. Clockwise increases the width.

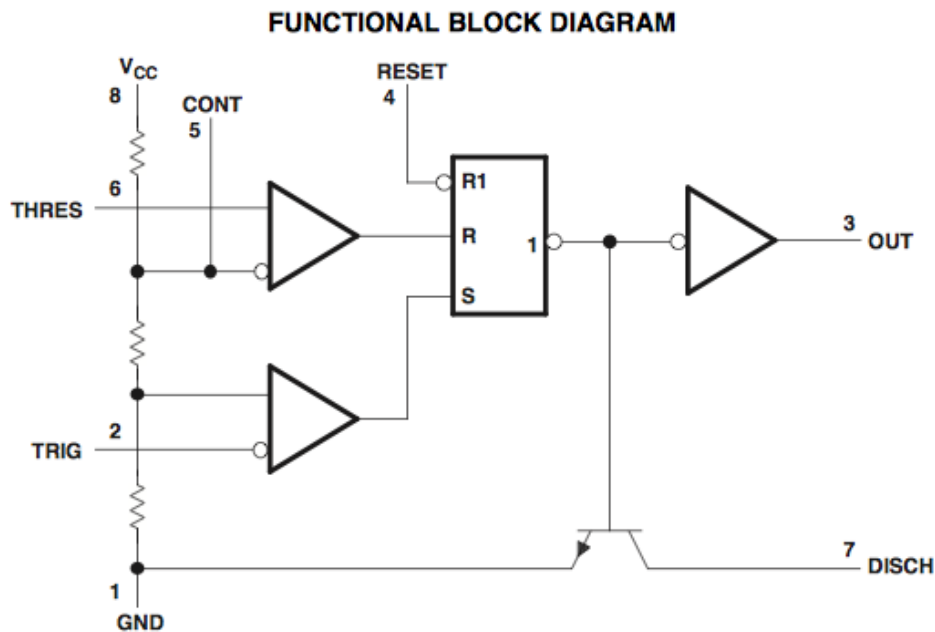


Figure 51: This block diagram depicts the function of the 555 timer. The trigger and threshold inputs are compared against $1/3V_{CC}$ and $2/3V_{CC}$ to set or reset the flip-flop respectively

The first thing to check in the GPS software is the status. It should say "over-determined clock". Other key items in the control software to pay attention to are

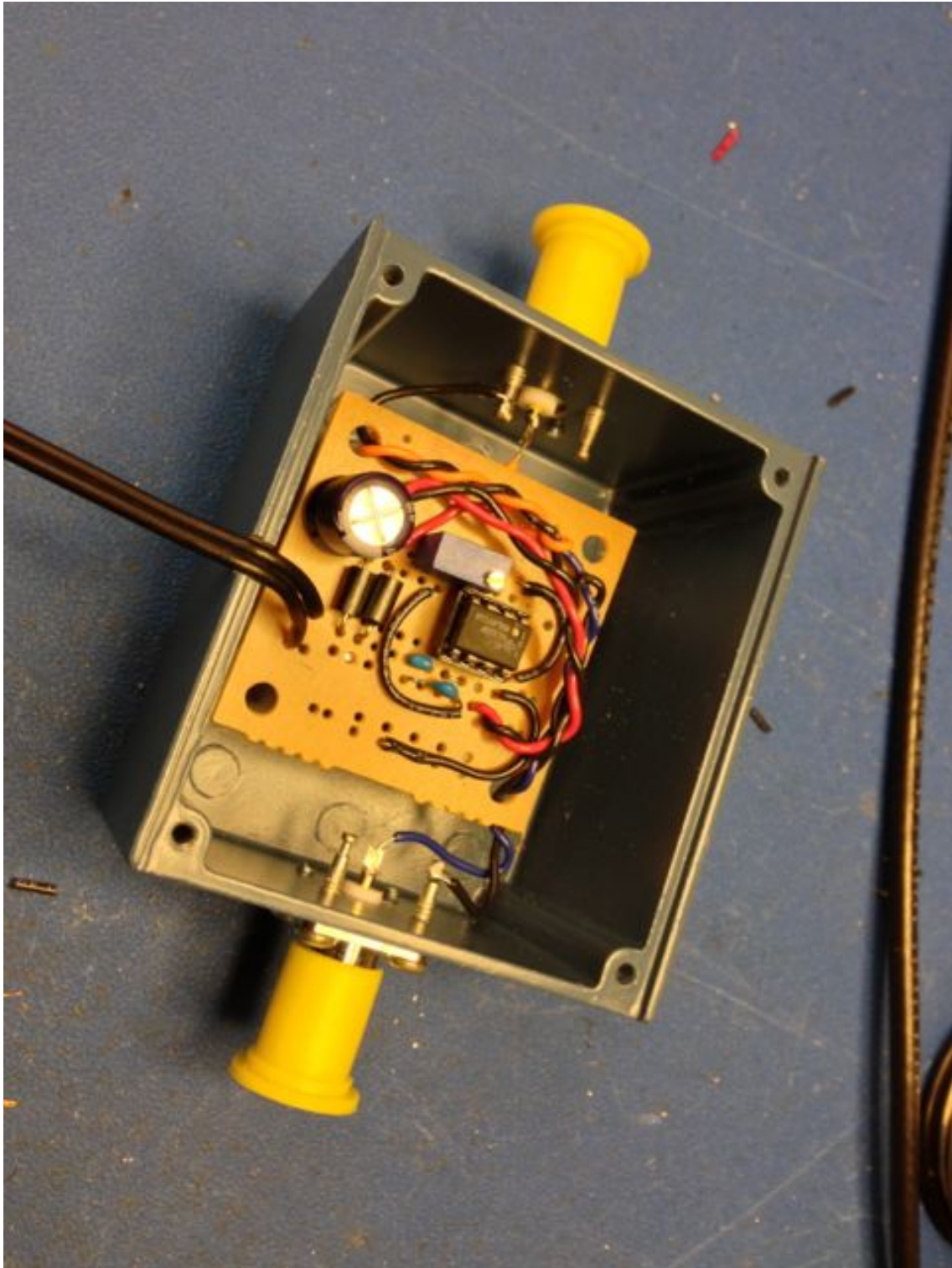


Figure 52: GPS Pulse Extender

basically the number of green lights (in this case 5) and the holdover time in the upper-right window labeled "Timing Receiver Status and Control". If things are working correctly the number of green satellites will typically be 4-5 with the antenna at it's current location. We should also not see any holdover time. When the receiver is not using any satellites it enters a "holdover" state where the oscillator is no longer disciplining. The GPS keeps track of how long it's been in holdover. Going into holdover could indicate a problem in the connection to the GPS antenna.

C.2 Front-End Code Installation

We have acquired a clone of the front end disk used at Livingston. The disk was backed up locally (sugar-dev3:/lab/frontend/sata-disk-backups/mnt2 as of 2013/02/18). The disk was adapted for use at Syracuse. The disk failed on 6 Feb 2013. This page documents the second build of the front end at syracuse...

C.2.1 Using LLO Cloned Disk

The cloned disk is saved in /lab/frontend/sata-disk-backups/mnt2 and a tar file of the contents was made on . We use the tar file from LLO to build a new machine. The new machine can either be used to serve a diskless front-end machine or used as a standalone front-end machine.

Diskless Node Install

1. Acquire machine with same architecture as front-end (presumably x86_64).
2. Login using gentoo minimal-CD or Live-DVD.
3. Repartition first disk (/dev/sda) to one partition and create ext3 filesystem.

4. Make mount point for sda1 and mount.

```
mkdir /mnt/fe
mount /dev/sda1 /mnt/fe
```

5. Make mount point for /lab and mount directory.

```
mkdir /mnt/lab
mount -t nfs 10.20.1.15:/sugwg/projects/lab /mnt/lab
```

6. copy tar file:

```
rsync -a /mnt/lab/frontend/sata-disk-backups/mnt2/fe.tar.gz /mnt
    /fe/
```

7. untar file:

```
cd /mnt
tar -xvf fe/fe.tar.gz
```

8. chroot into new filesystem and setup for use on network...

```
mount -t proc proc /mnt/fe/proc
mount --rbind /sys /mnt/fe/sys
mount --rbind /dev /mnt/fe/dev
chroot /mnt/fe /bin/bash
source /etc/profile
```

Local Disk Install

C.2.2 Minimal tar deploy

Create a tar file without the portage, front-end target, and cvs/svn directories...

Creating tar file for Syracuse front-end machine

This is the procedure used to create an archive of a front-end system modified for use at Syracuse. Here, I am using 10.20.1.44 (s1boot0) as the machine to boot from (the tftp server) and 10.20.1.45 (s1labfe1) is the diskless front-end machine. This can easily be modified for installation directly onto the hard drive.

1. Copy the fe tar file to `${FE_LOCATION}` and untar.

```
cd ${FE_LOCATION}
cp /lab/frontend/sata-disk-backups/mnt2/fe.tar.gz .
tar -xvpf fe.tar.gz
```

2. `${FE_LOCATION}/fe` is now the root directory for the front-end system

```
export FE_ROOT=${FE_LOCATION}/fe
```

- At LLO the controls user has UID:GID = 1001:1001. Change this to 512:512 for Syracuse. (You must execute this as root)

```
find ${FE_LOCATION} -xdev -user 1001 -print0 | xargs -0 chown
    512:512
```

- Change the lines for controls in the files `${FE_ROOT}/etc/passwd` and `${FE_LOCATION}/fe/etc/group`

- Edit `${FE_ROOT}/etc/ntp.conf`: Change "server" and "restrict" lines and comment out "broadcast" line

```
server 10.20.1.25
restrict 10.20.1.0 mask 255.255.255.0 nomodify nopeer notrap
```

- Comment out entries in `${FE_ROOT}/etc/conf.d/net` and add this line:

```
config_eth4=( "10.20.1.45 netmask 255.255.0.0 broadcast
    10.20.255.255" )
```

- Change ip address found in 3 files in `${FE_ROOT}/etc/xinetd.d/` from `10.144.0.0/24` to `10.20.1.0/24`

- Comment out 3 lines in `{FE_ROOT}/etc/resolve.conf`

- remove `${FE_ROOT}/opt/rtcds`

```
rm -rf ${FE_ROOT}/opt/rtcds
```

- Comment out all lines in `fstab` except for "shm" and add lines for root and lab.

```
10.20.1.44:/tftpboot/sllabfe1 / nfs sync,hard,intr,rw,nolock,rsize=8192,wsiz=8192 0 0
10.20.1.15:/sugwg/projects/lab /lab nfs sync,hard,intr,rw,nolock,rsize=8192,wsiz=8192 0 0
```

- Change `EPICS_CA_ADDR_LIST` in `${FE_ROOT}/opt/cdscfg` directory

```
find /ligo/feback/fe/opt/cdscfg/ -type f -print0 | xargs -0 sed
    --in-place=.old s/10.144.0/10.20.255/g
```

- Comment out `source /opt/cdscfg/rtsetup.sh` from `${FE_ROOT}/home/controls/.bashrc` and add the following lines in it's place:

```

export IF0=X2
export ifo=x2
export SITE=TST
export site=tst
export RCG_LIB_PATH=/lab/frontend/controls/git/cds_user_apps/cds
    /b1/models
export RTCDSROOT=/opt/rtcds/${site}/${ifo}
export NDSSERVER=10.20.1.45:8088
export EPICS_CA_ADDR_LIST="10.20.255.255"
export EPICS_CA_AUTO_ADDR_LIST="NO"
export LD_LIBRARY_PATH=${LD_LIBRARY_PATH}:/lib:/usr/lib:/usr/
    local/lib:/opt/rtapps/fftw-3.2.2/lib
source /opt/rtapps/epics/etc/epics-user-env.sh
source /opt/rtapps/ldas-tools-1.18.2/etc/ldas-tools-user-env.sh
source /opt/rtapps/libframe-8.11/linux-x86_64/etc/libframe-user-
    env.sh
source /opt/rtapps/libmetaio-8.2/linux-x86_64/etc/libmetaio-user
    -env.sh
source /opt/rtapps/gds/etc/gds-user-env.sh
export PATH=${PATH}:/opt/rtapps/dv:/opt/rtcds/${site}/${ifo}/
    scripts

```

Creating a bootable disk for front-end

This is how to build a disk that can be installed directly into a front-end machine.

NOTE The machine that you build this disk from must have the same type of disk controller as the front-end machine you intend to install this in.

1. Locate a spare disk and install in a machine connected to the internal network that you have root access to.
2. Mount /lab on this machine.
3. Use fdisk or parted to partition the spare disk.

Number	Start	End	Size	Type	File system	Flags
1	512B	32.0MB	32.0MB	primary	ext2	
2	32.5MB	542MB	510MB	primary	linux-swap(v1)	
3	542MB	1000GB	1000GB	primary	ext4	

4. Mount `/dev/sd*` (blank spare disk) at `/mnt/fe`

C.2.3 From Gentoo Source

Installation from source seems to be ideal, however the real-time code is working quite stably with a specific gentoo kernel. This kernel is no longer supported in gentoo so the OS has stagnated into the past a bit. One can, however, compile and run all but the real-time code itself in a current Gentoo environment without too much difficulty. This could be a benefit if one wanted to build an environment that resembles the front end system.

The kernel has a special patch to allow the OS to dedicate CPU cores to front-end models. The earliest supported kernel in the Gentoo source is newer than the most recent kernel patch for rtds. The patch is about 240 lines of code, but it would take some time to figure out how to apply it to the current version of the kernel and verify it's functionality.

front-end install procedure

1. Download the Gentoo amd64 minimal install iso image and burn it to a CD.
2. Boot the machine you wish to use as a front-end using the Gentoo CD.
3. Connect to the internet.
 - (a) Refer to local IT experts on how to connect using your network.
 - (b) At Syracuse we have a http proxy server running on the local network.
 - (c) If using a proxy type,

```
export http_proxy="http://proxy.server.com:port"
```

4. Using `links` download the stage3 tarball for amd64.

```
links http://www.gentoo.org/main/en/mirrors.xml
```

5. Untar the stage3 and install system:

```

tar xvjpf stage3-*.tar.bz2
vi /mnt/gentoo/etc/portage/make.conf
echo MAKEOPTS="-j5" >> /mnt/gentoo/etc/portage/make.conf
mirrorselect -i -o >> /mnt/gentoo/etc/portage/make.conf
cp -L /etc/resolv.conf /mnt/gentoo/etc/
mount -t proc proc /mnt/gentoo/proc
mount --rbind /sys /mnt/gentoo/sys
mount --rbind /dev /mnt/gentoo/dev
chroot /mnt/gentoo /bin/bash
source /etc/profile
export PS1="(chroot) $PS1"
emerge-webrsync

```

6. edit /etc/portage/make.conf to add USE flags,

```

USE="bindist mmx sse sse2 ssea qt4 qt3support png"
# echo "US/Eastern" > /etc/timezone
# emerge --config sys-libs/timezone-data
# nano -w /etc/locale.gen
# locale-gen
# eselect locale list
# eselect locale set <value>
# env-update && source /etc/profile
# emerge gentoo-sources

```

7. Configure kernel and compile

- This is to get a good baseline kernel for building the special front-end kernel.
- Configure the kernel with no modules to keep things simple. The front end models will be compiled as modules to the kernel.

8. Install bootloader

9. Reboot machine

10. Bypass startup sequence in \etc\inittab.

11. Checkout SVN repo advLigoRTS

- This can go anywhere. A central location is advised. We will create a link to this location next.

12. Create link in standard location which points to the rcg code

- Choose one of the following locations.

```
/opt/rtcds/rtscore/release
/opt/rtcds/${site}/${ifo}/core/release
/opt/rtcds/${site}/${ifo}/core/trunk
```

13. Checkout SVN repo userapps and link to one of the following standard locations.

```
/opt/rtcds/userapps/release
/opt/rtcds/${site}/${ifo}/userapps/release
/opt/rtcds/${site}/${ifo}/userapps/trunk
```

14. Checkout SVN repo cdscfg and copy contents of trunk to `\opt\cdscfg`

15. Initialize site settings for cdscfg. The options here are hardcoded in various places so unless you are at llo, lho, cit, mit, geo, or sta use the site location, tst. The corresponding ifo setting must be between x0 and x5. In this example I have chosen tst and x2.

```
# touch /opt/cdscfg/site/tst
# touch /opt/cdscfg/ifo/x2
```

16. Edit cdscfg scripts for location.

- In `/opt/cdscfg/tst/x2/rtrc.sh` edit the following lines.

```
LIGONDSIP=10.20.1.45
NDSSERVER=10.20.1.45:8088
EPICS_CA_ADDR_LIST="10.20.1.45"
```

17. Install applications in `/opt/rtapps/`.

```

# cd /opt/rtapps
# mkdir tarballs
# cd tarballs
# wget http://www.ldas-sw.ligo.caltech.edu/packages/framecpp
  -1.18.2.tar.gz
# wget http://www.ldas-sw.ligo.caltech.edu/packages/ldas-tools
  -1.18.2.tar.gz
# wget http://www.ligo.caltech.edu/~jzweizig/gds-release/gds
  -2.15.0.tar.gz
# wget http://www.fft.w.org/fftw-3.2.2.tar.gz
# wget http://www.aps.anl.gov/epics/download/base/baseR3
  .14.12.2.tar.gz

```

18. Install EPICS base in `/opt/rtapps/epics/base`.

19. Install EPICS seq module in `/opt/rtapps/epics/modules/sncseq`

C.3 Front-End Operation

C.3.1 Using a Model

Provided the models are already installed and running, using the model basically consists of 3 things; system control, filter modification, and data analysis. Each of these have a set of tools available that one should be aware of. Table 9 shows the tools available and highlights their use.

I will now step through the tools in more detail

medm

This is the primary tool for interacting directly with the running model. It runs a set of user-defined screens which have readouts and controls for various pre-defined points in the model. Some of these screens are generated automatically when the models are installed. For more details see the front-end users guide.

Many of the screens are generated after installing the model. They contain all the switches, knobs, meters, etc. needed for controlling some aspect of an experiment. One can redirect feedback using matrices, turn on and off filter modules, adjust gains

Tool	Use
medm	control
diaggui	data analysis
dataviewer	data analysis
foton	digital filter generation
awggui	arbitrary waveform generation and excitation

Table 9: This table describes the tools available and their purpose.

while monitoring things like DC photodiode levels and position sensor outputs for suspensions.

Additionally one can create a link inside one screen that pulls up another. We use this feature to build up what we call a "sitemap" which basically is the highest level screen for the site and generally has links to access the highest level screens for each model.

C.3.2 Running a Model

If a model has been installed already that you want to use, it may already be running. You can check what is running by logging into the front-end machine and running the `system_check` command.

To interact with the running model from the workstation in the lab, start up medm. Open a terminal and type,

```
# sitemap &
```

This will start medm in execute mode and open a screen representing the top level for the lab.

A well designed medm screen should be fairly intuitive. However MEDM screens are, in general, not representative of the underlying frontend code. You will also need to open the model file which is written in MATLAB Simulink for reference in order to understand how the system works.

C.3.3 Changing a Filter

Eventually you will need to change filters in the model. This is done through the application, Foton. To open a GUI window for Foton the command is simply `foton`. You will need to navigate to the `chans` directory to access the filter files. The easiest way to do this is by using the previously configured alias, `chans` before starting Foton. The following set of commands will open a Foton GUI in the appropriate location.

```
# chans
# foton &
```

C.3.4 Changing a Model

The models are written using the MATLAB SimuLink GUI. The GUI allows you to easily connect various block together with wires. The blocks represent some sort of signal processing while the wires represent the flow of signal itself. The GUI generates a text file that describes the system which is then parsed by Perl scripts in the RCG code during front-end compilation. The Perl scripts generate C code which is then compiled by the RCG into a kernel module which takes over a single CPU core.

For the user, changing a model consists of editing the SimuLink file using the GUI and then recompiling the front-end code. The compilation procedures are,

1. Log into the frontend machine

```
# s1fe
```

2. Change to the cdscode directory using alias

```
# cdscode
```

3. Compile and install model

```
# make x2model
# make install-x2model
```

C.3.5 Data Storage

Data is stored in frame files located on the boot machine hard drive at `/frames`. The files are generated by the data acquisitions (DAQ) daemon (`daqd`). Channels are

configured to record from the SimuLink GUI. There is a limited amount of lookback time due to space limitations on the harddrive. This is handled automatically by a deleting old frame file to make room for new ones. The number of frame files that can exist depend on the space available and the size of the files which grows with the number of channels recorded and their recording rates. This is accomplished using a cron job which is a process that is run periodically. This cron job checks the amount of free disk space and deletes enough old frame files to get the disk usage down below some threshold percentage.

C.3.6 Analysis Tools

There are a few tools one can use to access the data in from either frame files or online. With Diagnostic Test Tools (DTT) one can look at raw and filtered time series data, or process an amplitude spectral density (ASD). One can also run various tests which involve actuating at an excitation point.

In DTT, the most commonly used test is the swept sine test for generating a transfer function.

Bibliography

- [1] Thomas Corbitt, Yanbei Chen, Edith Innerhofer, Helge Müller-Ebhardt, David Ottaway, Henning Rehbein, Daniel Sigg, Stanley Whitcomb, Christopher Wipf, and Nergis Mavalvala. An all-optical trap for a gram-scale mirror. *Phys. Rev. Lett.*, 98:150802, Apr 2007.
- [2] Antonio Perreca, James Lough, David Kelley, and Stefan W. Ballmer. Multidimensional optical trapping of a mirror. *Phys. Rev. D*, 89:122002, Jun 2014.
- [3] L. Barsotti and M. Evans. Modeling of alignment sensing and control for advanced ligo. Technical Report LIGO-T0900511-v4.
- [4] J. A. Sidles and D. Sigg. Optical torques in suspended Fabry Perot interferometers. *Physics Letters A*, 354:167–172, May 2006.
- [5] P. R. Saulson. Thermal noise in mechanical experiments. *Phys. Rev. D*, 42:2437–2445, October 1990.
- [6] A. L. Greensite. *Elements of modern control theory*. Spartan Books, 1970.
- [7] G. F. Franklin and A Powell, J. D. Emami-Naeini. *Elements of modern control theory*. Addison-Wesley Publishing Company, 1994.
- [8] V. B. Braginsky and S. P. Vyatchanin. Low quantum noise tranquilizer for Fabry-Perot interferometer. *Physics Letters A*, 293:228–234, February 2002.
- [9] S. W. Ballmer and D. J. Ottaway. New class of optical beams for large baseline interferometric gravitational wave detectors. *Phys. Rev. D*, 88(6):062004, September 2013.
- [10] A. E. Siegman. *Lasers*. University Science Books, 1986.

- [11] Eric D. Black. An introduction to Pound-Drever-Hall laser frequency stabilization. *American Journal of Physics*, 69(1):79–87, 2001.
- [12] Alexandr Ageev, Belkis Cabrera Palmer, Antonio De Felice, Steven D Penn, and Peter R Saulson. Very high quality factor measured in annealed fused silica. *Classical and Quantum Gravity*, 21(16):3887, 2004.
- [13] J Winterflood, T Barber, and D G Blair. Using euler buckling springs for vibration isolation. *Classical and Quantum Gravity*, 19(7):1639, 2002.
- [14] Peter R. Saulson. *Fundamentals of Interferometric Gravitational Wave Detectors*. World Scientific, Singapore, 1994.
- [15] Herbert B. Callen and Richard F. Greene. On a theorem of irreversible thermodynamics. *Phys. Rev.*, 86:702–710, Jun 1952.
- [16] Yu. Levin. Internal thermal noise in the ligo test masses: A direct approach. *Phys. Rev. D*, 57:659–663, Jan 1998.
- [17] Stefan W. Ballmer. *LIGO interferometer operating at design sensitivity with applications to gravitational radiometry*. PhD thesis, Massachusetts Institute of Technology, June 2006.

Vita

Name of Author

James D. Lough

Place and Date of Birth

Blacksburg, Virginia

August 30, 1973

Colleges and Universities

Virginia Tech

Degrees Awarded

B.S. Physics, 2001

Publications

1. Perreca Antonio, Lough James, Kelley David, and Ballmer Stefan W, *Multidimensional optical trapping of a mirror*, Phys Rev D **89** 122002 (Jun 2014),
<http://link.aps.org/doi/10.1103/PhysRevD.89.122002>
2. White GR, Lough J, Duncan D, Davis JP, and Narducci FA, *Quantum optic techniques for diagnostics of a gradient magnetometer atom interferometer*, Journal of Modern Optics **56** 2013–2021 (2009),
<http://dx.doi.org/10.1080/09500340903243455>